INVESTIGATION OF CREASES IN ULTRA-THIN MEMBRANES

D. M. S. P. Dassanayake

188037G

Degree of Master of Science

Department of Civil Engineering

University of Moratuwa
Sri Lanka

September 2019

INVESTIGATION OF CREASES IN ULTRA-THIN MEMBRANES

D. M. S. P. Dassanayake

188037G

Thesis submitted in partial fulfilment of the requirements for the degree of Master of Science in Civil Engineering

Department of Civil Engineering

University of Moratuwa
Sri Lanka

September 2019

Declaration

I declare that this is my own work and this thesis does not incorporate without acknowledgement any material previously submitted for a Degree or Diploma in any other University or institute of higher learning and to the best of my knowledge and belief it does not contain any material previously published or written by another person except where the acknowledgement is made in the text.

Also, I hereby grant to University of Moratuwa the non-exclusive right to reproduce and distribute my thesis, in whole or in part in print, electronic or other medium. I retain the right to use this content in whole or part in future works (such as articles or books).

..... Date :

D. M. S. P. Dassanayake

The above candidate has carried out research for the Master′s thesis under my supervision.

..... Date :

Dr. H.M.Y.C. Mallikarachchi

Abstract

The use of thin membranes is widespread in a variety of applications in a range of industries owing to the lightweight nature and small packaged volume attainable by them. When facilitating the storage of large areas of membranes by folding−specifically in aerospace applications, the resulting creases alter the physical state and material properties of the overall membrane structure. Even though numerical modelling is preferred as a viable tool in replicating space environments on earth in the form of reduced gravity and air drag, the idealisations utilised in these analyses require validation via small-scale experiments. The significance of this process is highlighted due to past endeavours which failed to idealise the crease mechanics accurately, leading to inaccurate predictions and eventual failure in complete missions. Moreover, the use of virtual testing in this regard is limited by the unavailability of accurate experimental data.

In this research, an attempt has been made to characterise the crease mechanics of multiple creased thin Kapton 100 HN poyimide membranes using an experimental study. A combination of specimens consisting of two and three creases have been analysed in this regard, and moment−angle responses were plotted using results of physical experiments. The results indicated different crease stiffnesses for each crease in a parallel-creased specimen, with the highest stiffness observed for a crease nearest to the pinned support. However, all the stiffness values obtained herein were observed to be of a lower order than the simulation and physical experimental results obtained by previous researchers for membranes with a single crease, which could be attributed to the precise measurements taken during the experimental study and the incorporation of the effect of self-weight of the membrane into its moment−rotation response, which was neglected in earlier studies. The time dependence of the opening behaviour

was also studied, and it was identified that the membrane achieves a constant opening angle in a shorter time duration on being loaded.

An improved experimental setup was designed and developed, on identifying the limitations and inaccuracies observed in the experimental setup devised by previous researchers. This ensured controlled displacement being offered to the membrane for capturing its deployment behaviour over a wider regime of loading, along with precise force measurement. The setup included additional measures to facilitate its usage for specimens of a wider range of dimensions, and to ensure proper alignment of the membrane, thereby enhancing the accuracy of the results obtained via the physical experiments which would then be utilised for idealisation schemes of deployment simulations in virtual environment.

Crease stiffness determined for single-creased membranes utilising the improved setup was implemented in Abaqus/Explicit finite element package for the purpose of predicting the deployment behaviour of membrane structures with multiple creases accordingly. The crease-line was represented with connector elements specifying the rotational elasticity, and was observed to have negligible effect on the deployment which contradicts the experimental observations. Hence, further investigations are required for assessing the accuracy of this claim.

A quasi-static simulation was carried out for a simple creased unit based on traditional "Waterbomb" base for predicting the deployment behaviour consisting of intersecting creases. The simulation developed in Abaqus/Explicit environment was able to capture the deployment response observed in the physical experiments, in terms of maximum deployment ratio and shape on incorporating the effect of gravity to the simulation.

Keywords : *ultra-thin membranes, crease mechanics, rotational stiffness, multiple parallel creases, finite element simulations*

Dedication

To my parents, whose unyielding love, support and encouragement has enriched my soul and inspired me to pursue and complete this research.

Acknowledgement

First and foremost, I would like to express my sincere gratitude to my supervisor, Dr. Chinthaka Mallikarachchi, for providing me with technical guidance, valuable insights, advices and encouragement throughout the past year. Without his support, this would have not been possible. Secondly, I would like to thank Prof. Priyan Dias and Prof. Rangika Halwatura for their conducive comments and suggestions during progress reviews, which contributed greatly towards the research directives taken thus far.

Thirdly, I would like to extend my special thanks to Mr. K.H.J. Mangala, of the Department of Mechanical Engineering, University of Moratuwa for the immense support offered in the form of technical guidance and workmanship for the development of the improved experimental setup for controlled deployment of thin folded membranes. My sincere appreciation goes to Seyon Mierunalan, Varakini Sanmugadas, Hasitha Wijesuriya, Vishnu Punithavel, Roanga De Silva, Chameera Randil, Isuru Nanayakkara, Sujeeka Nadarajah and Hasini Weerasinghe for being great research colleagues and for their support and helpful conversations throughout my research work.

Further, I would like to recognise the technical staff of the Mechanics of Materials and Structural Testing Laboratories of the Department of Civil Engineering, University of Moratuwa for supporting me throughout the laboratory experiments. Moreover, for providing me with the necessary knowledge and expertise required to carry out this research, my heartfelt gratitude is extended to the academic staff of the Department of Civil Engineering, University of Moratuwa and also to the authors of the literature referred, which paved the way for this research.

Finally, I would like to thank the Ministry of Science, Technology and Research under Indo−Sri Lanka Joint Research Project, National Research Council, Sri Lanka and Senate Research Committee of the University of Moratuwa for the financial assistance provided, without which this would not have been a possible achievement.

Contents

Declaration i

Abstract ii

Dedication iv

Acknowledgement v

Contents vii

List of Figures x

List of Tables xiii

Nomenclature xiv

1 Introduction 1

1.1 Deployable Thin Membrane Structures 1

1.2 State of the Art 2

1.3 Alternatives to Physical Testing 5

1.4 Scope and Aim 8

1.5 Chapter Organisation 9

2 Literature Review 11

2.1 Creased Membrane Structures 11

2.1.1 Crease patterns 11

2.1.2 Applications 13

2.2 The Phenomenon of a Crease 15

2.2.1 Rigid Origami versus Non-Rigid Origami 15

2.2.2 Hinge Response at the Crease 16

2.3 Studies on Creased Membrane Structures 19
2.3.1 Analytical Studies 19
2.3.2 Experimental Studies 22
2.3.3 Numerical Studies 25

3 Multiple Parallel-creased Membranes 29
3.1 Moment−Rotation Response of Parallel Creases 29
3.1.1 Experimental setup 30
3.1.2 Moment and angle measurements 34
3.1.3 Self-weight of the membrane 34
3.1.4 Time dependence of opening angle 37
3.2 Results and Discussion 40
3.2.1 Limitations in the existing experimental setup 45

4 Improved Experimental Setup 46
4.1 Controlled displacement 46
4.2 Force measurement 48
4.2.1 Measuring scale 48
4.2.2 Extension of the thread 49
4.3 Boundary conditions 49
4.4 Horizontal and vertical alignment 50
4.5 Results and Discussion 51

5 Implementation in Finite Element Package 54
5.1 Modelling the crease-line and membrane panels 54
5.2 Finite element model of multiple creased thin membranes 55
5.2.1 Finite element model of membrane with two creases 56
5.2.2 Abaqus/Explicit Solver 59
5.3 Results and Discussion 60
5.3.1 Sensitivity of the simulation for membrane with two creases 60
5.3.2 Comparison with experimental results 63

6 Quasi-static Deployment Simulation of a Creased Unit 64
6.1 Crease pattern 64
6.2 Details of the experimental study 65
6.3 Finite element model of the creased unit 66
6.4 Results and Discussion 67
6.4.1 Sensitivity of the simulation for the creased unit 67

6.4.2 Comparison with physical experiments 69

7 Conclusions and Future Work **71**

7.1 Conclusions 71

7.2 Recommendations for Future Work 72

References **73**

Appendix A: Moment−Angle Data **81**

1. Single Crease Stiffness (Initial Experimental Setup) 81
2. Single Crease Stiffness (Improved Experimental Setup) 84
3. Stiffness of Membrane with Two Creases (Initial Experimental Setup) 86
4. Stiffness of Membrane with Two Creases (Initial Experimental Setup - Different Orientations) 90
5. Stiffness of Membrane with Three Creases (Initial Experimental Setup) 94

Appendix B: Keywords of Abaqus Input Files **97**

1. Predicting Deployment Behaviour of Membrane with Two Parallel Creases 97
2. Quasi-static Deployment Simulation of a Simple Creased Unit 99

List of Figures

1.1 (a) Artist′s concept of LightSail-2 above Earth (b) An image taken during its sail deployment sequence 2
1.2 IKAROS Solar Sail Deployment Process 3
1.3 LightSail-2 spacecraft sitting on its low friction deployment table following a successful solar sail deployment test at Cal Poly San Luis Obispo on January 28, 2016 4

2.1 Miura-Ori Tessellation 12
2.2 Two waterbomb bases and their tessellations 13
2.3 Applications of creased membrane structures 14
2.4 The geometry of a single straight crease described by its length L and three unit vectors $(\vec{u}, \vec{v}, \vec{w})$ 15
2.5 Geometric state of membrane 16
2.6 Schematic of the experimental setup used to calculate the moment−angle relationship in a crease 18
2.7 Relaxation process and the mechanical response of a single creased Mylar sheet to an external strain 23
2.8 (a) Moment–angle relationship for a Mylar sheet of 350 μm thickness (b) Stiffness k for different thicknesses 24
2.9 Sketch of the pinching experiment used for measuring dimensionless crease stiffness 24
2.10 Linear response between the resistive moment and opening angle . 25
2.11 Schematic diagram of the steps of simulation for creasing and subsequent uniaxial tensile test of thin Kapton membrane 26
2.12 Deformed shape of 25 μm Kapton membrane 27

3.1 Multiple parallel-creased membrane 29
3.2 Parallel-creased membrane specimens 31

3.3 Creasing procedure 32
3.4 Self-opening action of creases 32
3.5 Boundary conditions 33
3.6 Loaded specimens 34
3.7 Free-body diagram of creases 35
3.8 Free-body diagram for resistive moment derivation 36
3.9 Achieving static equilibrium - load cases 37
3.10 Static configuration - unloaded case 38
3.11 Static configuration - loaded case 39
3.12 Moment−rotation relationship for a single crease 41
3.13 Moment−rotation relationship for two creases 42
3.14 Orientations of the specimen 42
3.15 Moment−rotation relationship for two creases - different orientations 43
3.16 Moment−rotation relationship for three creases 44

4.1 Improved experimental setup 46
4.2 Controlling displacement 47
4.3 Calibration of measuring scale 48
4.4 Boundary conditions 50
4.5 Additional components 51
4.6 Improved experiments 52
4.7 Improved moment−rotation relationship for a single crease 53

5.1 Local axes and vector definitions for (a) crease region (b) a connector element 55
5.2 Mesh refinement at the crease 57
5.3 Node-based connectors placed perpendicular to the crease-line . . 58
5.4 Comparison of kinetic energy profile with the internal energy profile of the finite element simulation for membrane with two creases 61
5.5 Energy variation of the finite element simulation for membrane with two creases 62
5.6 Snapshots taken during deployment simulation at different ratios of deployment compared with the shape of membrane observed during the experiment 63

6.1 Crease pattern 64
6.2 Simple creased unit (experimental study) 65

6.3 Deployment of simple creased unit (experimental study) 66
6.4 Finite element geometry of simple creased unit 67
6.5 Comparison of kinetic energy profile with the internal energy profile of the finite element simulation for creased unit 68
6.6 Energy variation of the finite element simulation for creased unit . 68
6.7 Energy variation of the finite element simulation for creased unit . 69
6.8 Snapshots taken during deployment simulation at different ratios of deployment compared with the final shape of structure observed during experiments 70

List of Tables

3.1 Experimental data for a membrane specimen with two creases . . 40
3.2 Summary of crease stiffnesses obtained via regression analysis . . 44

4.1 Single crease stiffness 53

5.1 Material properties of Kapton used in the finite element simulation of multiple creased membrane 57

Nomenclature

List of Abbreviations

ARGOS Active Response Gravity Offload System

DLR German Aerospace Centre (Deutsches Zentrum für Luft- und Raumfahrt)

ESA European Space Agency

IKAROS Interplanetary Kite-craft Accelerated by Radiation of the Sun

JAXA Japanese Aerospace Exploration Agency

LEO Low Earth Orbit

NASA National Aeronautics and Space Administration

PDT Pacific Daylight Time

UTC Coordinated Universal Time

List of Symbols

$\hat{V_i^j}$ Vector in the i^{th} direction for node j

ν Poisson's ratio

ω_{max} Highest Eigenvalue of the model

ϕ Neutral angle

ρ Material density

θ Current crease opening angle

ξ Fraction of critical damping in the fundamental frequency mode

c_d	Dilatational wave speed
c_v	Viscous damping coefficient
D_f	Fully deployed dimension of creased structure
E	Modulus of elasticity
E_i	Internal energy of the system (elastic, inelastic and artificial strain energy)
E_{ke}	Kinetic energy
E_{total}	Total energy of the system
E_{vd}	Energy absorbed by viscous dissipation
E_{wk}	Work done by external forces
F	Tensile load
k	Crease-line stiffness
k_o	Crease-line stiffness during crease actuation (and panel bending)
k_r	Crease-line stiffness during self-opening
l	Length of a membrane panel
L^*	Non-dimensional length
l_h	Horizontal distance from the crease-line to the loaded tip
l_{min}	Minimum length of the finite element
M	Resistive moment at the crease-line
M_c	Kinematic moment in the connector
t	Thickness
w	Width of the membrane coupon

Chapter 1

Introduction

1.1 Deployable Thin Membrane Structures

Larger areas and compact enclosures offered by thin membranes along with the ease of transportation facilitated by deployable structures have earned "deployable thin membrane structures" a rise in popularity over the recent years. The introduction of folds or "creases" solved the fundamental problem of enclosing membranes having large spans in compact stowage spaces of transportation vehicles, to be later unfurled to their full dimensions for their designated purposes.

The Japanese folding technique−Origami metamorphosed in mid-1980′s from merely an art form to a systematic geometric arrangement of folds and panels accordingly. This in turn led to the possibility of new meta materials, where the concept of "Origami Engineering" allowed packaging and deployment of folded sheets in a predetermined and robust path [1].

Interestingly, the auxetic behaviour and multi-stability resulting from the introduction of creases has led to plane inextensible sheets displaying a unique mechanical property: reconfigurability [2] i.e. the ability to undergo large configurational deformations, leading to applications in a wide range of fields from deployable space structures [3] and assembly of complex architectures [4] to functional meta materials [4, 5].

Out of the above fields, the high area-mass ratio, small packaged volume and flexible nature of thin membranes are being increasingly utilised by the aerospace industry owing to their significant sizing requirements in the range of hundreds of metres and the low areal density and weight requirements for launch and during flight. Solar sails, deployable sunshields, reflectors and

inflatable telescopes are some innovative gossamer structures employing large areas of membranes for collecting a higher quantity of flux, while receiving a higher spatial resolution of signals transmitted from space due to the higher aperture offered.

An artist′s concept of LightSail-2−a demonstration of controlled solar sailing above Earth, and an image taken during its sail deployment sequence on July 23, 2019 at 11:48 PDT (18:48 UTC) are shown in Figure 1.1.

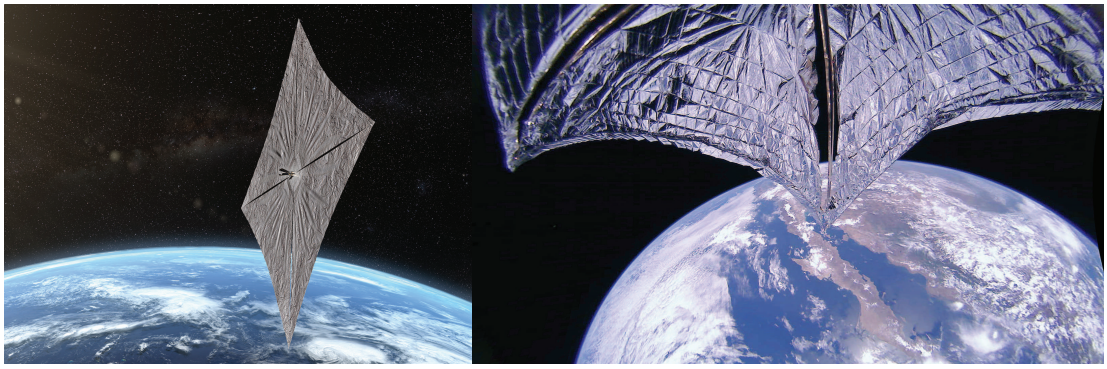

Figure 1.1: (a) Artist′s concept of LightSail-2 above Earth (b) An image taken during its sail deployment sequence
(Courtesy: The Planetary Society)

Deployable membrane structures call for unique and often contradictory requirements inducing very compelling structural challenges, of which, ensuring controlled, autonomous and ascertained tear-free deployment and structural performance following deployment are of crucial importance.

1.2 State of the Art

In the past 20 years, several initiatives have been taken in studying the deployment mechanics of space structures for various missions associated with power generation, communication and space craft propulsion. However, quantifying the independent behaviour of the thin membranes incorporated in the structure has only been done at a limited capacity, as was the case in the NASA sponsored test of a 20 m square solar sail in 2001 [6]. The overall deployed behaviour of the sail craft, consisting of four booms in addition to the sail was the main focus in this study.

On the other hand, physical testing procedures are subjected to additional constraints; gravity and air drag, the accuracy of results being dependent on how meticulously a representative space environment is achieved during testing. For example, the high rates of deployment of approximately 25 mm/s employed during experiments carried out on a 5 m $\times$ 5 m square sail of 7.5 μm thick aluminized Kapton by DLR and ESA, led to the measured deployment forces being affected by gravity and air drag [7]. The usage of the slowest possible rate of deployment was recommended by Seefeldt et al [8] in order to reduce inertial loads during deployment during their analysis of the Gossamer-1 mission of DLR. Also, an increase in deployment forces and changes to the deployment angles of the membrane were indicated on increasing direct gravity load [8, 9]. Moreover, the spinning-deployable spacecraft mission IKAROS developed by JAXA illustrated by Figure 1.2 encountered inertial effects owing to the dynamic nature of the experiment, rendering the dynamic predictions of these large sails to be imperative.

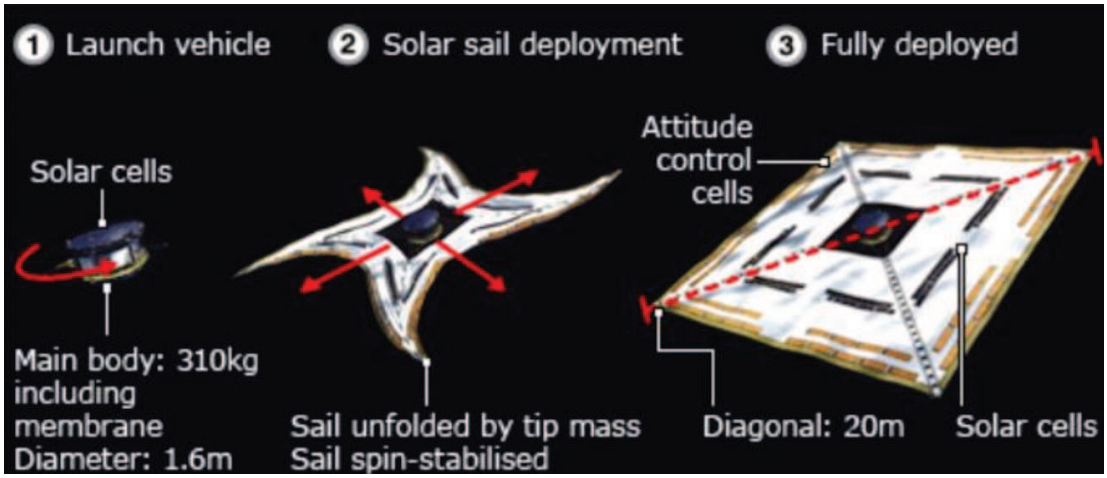

Figure 1.2: IKAROS Solar Sail Deployment Process
(Courtesy: JAXA)

Highlighting the importance of aforementioned dynamic predictions, the dynamic behaviour of spinning solar sails during deployment was analysed considering their out-of-plane and in-plane motions [10]. The influences of initial conditions, structural and control parameters on the stabilisation of deployment process was investigated on, but the focus was the overall structure which consisted of continuous cables as well.

Figure 1.3: LightSail-2 spacecraft sitting on its low friction deployment table following a successful solar sail deployment test at Cal Poly San Luis Obispo on January 28, 2016

(Courtesy: The Planetary Society)

NASA has investigated utilising solar sails for the purpose of validating the de-orbiting functionality of 3–element CubeSats in the presence of atmospheric drag. The four-quadrant 20 m solar sail NanoSail-D of NASA was one of the first attempts at the above, followed by NanoSail-D2 in 2010 where a 10 m^2 square sail of 7.5 μm thick ultra-thin reflective polymer material CP1 was used, successfully accomplishing the goal of deploying a sail in LEO [11–14]. Another objective of NanoSail-D mission was to demonstrate the capability of deploying the sail without re-contacting the spacecraft [15].

Low friction tables have been used for the purpose of counteracting the effects of air drag during initial ground deployment tests of NanoSail-D mission as well as the LightSail mission of the Planetary Society, as shown in Figure 1.3. LightSail-1 employed a 4.5 μm thick Mylar square sail of 32 m^2 area to demonstrate controlled solar sailing in LEOs, with LightSail-2 developed as a fully-functional spacecraft demonstrating true solar sailing. The latter shows

promising development on overcoming air drag, with its successful deployment and the addition of a momentum wheel facilitating higher altitudes, thus preventing the air drag present in Earth′s atmosphere from dominating any propulsion from the sun [15–18].

In terms of eliminating the effects of gravity in simulating a space environment, gravity offload systems such as ARGOS [19] are limited to stiff structures with motorised deployment, otherwise resulting in greater differences in deployment behaviour [20]. Membranes utilised for deployable structures of interest typically possess low stiffness due to their thicknesses in the range of a few micrometres, which leads to inevitable sagging of the membrane at full deployment.

The extremely large size of the sails, the time taken for sail deployment; which is usually 2-3 days [16] and the cost constraints of the endeavour limit the possibility of utilising drop towers and zero-gravity flights for the purpose of decoupling the effects of gravity during physical testing of these thin structures. Even so, the effect of air drag is still problematic during the testing stage for controlled deployment, and this calls for alternative methods of testing quite apart from the physical testing scenario.

1.3 Alternatives to Physical Testing

Exhaustive exploration of the deployment behaviour of thin membrane structures via physical testing is quite challenging, since the process of replicating the features of space environment, viz; reduced gravity and vaccuum tends to be tedious and costly.

Several approaches have been taken accordingly, in order to replace experimental testing with a more viable analysis tool, capable of accommodating several design cycles for the purpose of design optimisation of membrane structures [20].

Seefeldt [9] developed a mathematical model for establishing the stowing and deployment geometry of Gossamer-1 sail of DLR, where the coiled configuration of the sail was idealised as a spiral and a helix. The model represented the progression of the deployment forces observed in the physical

tests satisfactorily. Closed form equations were derived by Gattas et al. [21] and Zhou et al. [22] to describe the complete folding process of patterns consisting of a repeated assemblage of unit cells such as the "Miura-Ori" and its derivatives. However, these studies based on geometric considerations in its entirety, are considered applicable only in cases where the membrane panels are infinitely rigid in bending, which is far from a realistic approximation of their behaviour.

Papa and Pellegrino [23] developed a simple analytical model for a creased membrane, by relating the geometric properties of two perpendicular creased beams to the physical dimensions of the thin membrane. The relative displacements of the membrane during deployment were captured with adequate accuracy. An analytical dynamics model of a sail was derived by Funase et al. [24] considering the first mode of oscillation of the sail membrane. The membrane, isotropic in nature was idealised as mass points connected by springs and dampers, and validated with vibration experiments. Wang et al. [25] idealised an Origami-based circular cylindrical shell as rigid plates linked by elastic hinges, in order to study its kinematics and elastic properties. However, this study was limited to the analysis of the mechanical response of structures based on two specific variations of periodic Miura-Ori unit. Filipov et al. [4] introduced a model consisting of bars and hinges to simulate the in-plane stiffness of Origami panels, with the orientation of bars allowing for the bending of the panels along the diagonals, and rotational hinges facilitating the out-of-plane bending of the panels and the moment-rotation behaviour of prescribed creases. Nevertheless, the contact behaviour between the membranes and discontinuities in the process of deployment; such as sudden changes in geometry that are characteristic of membrane structures have not been incorporated into all these techniques [20].

In addition to analytical models, numerical models have also been employed to study the folding and deployment behaviour of membrane structures. Rapid advancement of high performance computers and the availability of robust algorithms in commercial finite element packages for capturing contact behaviour and the discontinuities involved, has led to enhanced feasibility of numerical analysis in comparison with pure analytical approaches [20, 26]. Funase et al. [24] utilised a precise multi-particle numerical model for the analysis of a spinning solar sail, which substituted the elements of

the membrane to particles connected by springs. It was highlighted, however, that the validity of the applicability of this technique is highly dependent on the approximations used during the idealisation and requires comparison with compatible experiments. Satou and Furuya [27] developed a finite element model to identify the elasto-plastic deformation properties of space membranes during crease formation and consequent deployment. The significance of conducting fold experiments to justify the results obtained from the numerical analysis was pointed out in this study as well.

As indicated above, even though testing in virtual environments seem to be an attractive alternative over physical testing, the importance of accurate idealisation schemes should be understood. When it comes to creased membrane structures, the relative values of bending stiffness of the sheet and torsional stiffness of the crease determines the type of deformation undergone by the sheet on being folded, in terms of panel bending or crease opening [28]. The presence of creases results in a negative Poisson's ratio effect in the structure, which ultimately leads to a singular response of highly compacted thin membranes to stretching and bending [29]. However, membrane structures have been often idealised to be consisting of infinitely rigid faces in bending connected by a series of flexible creases. The initial failure of IKAROS solar sail demonstrator is a credible example to support the claim that utilising accurate means of idealising the plastic deformations on folded sheets is imperative for preventing the time and cost implications associated with poor predictions on deployment behaviour [30].

Accordingly, researchers have attempted at quantitative incorporation of material test data and initial imperfections of the structure to numerical models, in order to accurately predict the deformation profile and unfolding process of creased membranes [31, 32]. As it stands, the stand-alone implementation of virtual testing has been constrained due to the absence of reliable experimental data on crease-line mechanics and the challenges encountered during measurement of crease properties with the required level of precision.

1.4 Scope and Aim

This research is aimed at characterising multiple creases in highly compacted thin membrane structures. For this purpose, the crease-line mechanics of single and multiple parallel creases in thin membranes are studied in terms of an experimental study and by developing constitutive relationships. Crease properties, are then incorporated into the virtual simulation techniques proposed by Dharmadasa and Mierunalan [20, 32] for the purpose of studying their deployment behaviour, which in turn is compared with the behaviour obtained via the experimental study.

Accordingly, the experimental study conducted in this regard is utilised to serve two main purposes, viz; characterising the crease-line properties, and validating the applicability of the simulation technique within the multiple crease regime. It is understood that virtual testing overcomes the measurement difficulties and the inevitable inaccuracies accompanying physical experiments. The goal of this study is to aid the implementation of such efficient analysis techniques through reliable physical test data on the mechanical response of crease-lines during its deployment sequence.

On account of the capabilities of Kapton Polyimide membranes in preserving its distinctive physical, electrical and mechanical properties over a wide range of temperatures (-269° C to 400° C) [33], it is a material preferred for use in applications carried out in the space environment, and hence, in this study.

First, experiments were carried out on single and multiple parallel-creased thin Kapton membranes in order to obtain their moment−angle responses utilising a setup developed by Dharmadasa [32] during his analysis of single folded thin membranes. The responses obtained herein were compared with the experimental results obtained by Dharmadasa et al. [26]. On identifying and overcoming the limitations in the previous experimental setup, an improved setup was developed, which facilitated providing controlled displacement to thin membranes with multiple parallel creases and measuring deployment forces with a satisfactory level of accuracy. The redesigned setup was utilised to carry out further experiments, from which, data was extracted on the moment−angle response and deployment behaviour.

The developed crease-line behaviour model was implemented in geometrically nonlinear contact analyses using commercial finite element package Abaqus/Explicit [34], for simulating the deployment of multiple parallel-creased thin Kapton membranes using the simulation technique presented in [20, 32]. A quasi-static deployment simulation of a creased unit consisting of intersecting creases was carried out using Abaqus/Explicit package to study the changes to the deployment behaviour owing to the presence of an intesection, typical of all folding patterns used for compacting solar sails for stowage.

1.5 Chapter Organisation

This thesis consists of 7 chapters. After the current introductory chapter on the field of research, Chapter 2 gives an overview of literature on creased membrane structures, its applications and the past endeavours in simulating their folding and deployment behaviour in the form of numerical and analytical models and experimental investigations. In this chapter, emphasis is given to the necessity of integrating crease properties in the analysis.

Chapter 3 focuses on characterising the crease-line properties of multiple parallel-creased membranes using an experimental study. This chapter also includes a formulation for the resistive moment at the crease incorporating the effect of self-weight of thin membranes and illustrates an investigation into the time dependence of the moment−angle response of multiple parallel-creased membranes. The limitations and measurement difficulties involved with the existing experimental setup are also identified.

Chapter 4 narrates the features of an improved experimental setup developed to facilitate controlled displacement and precise deployment force measurement of thin creased membranes. It also concentrates on the characterisation of crease-line mechanics of multiple parallel-creased membranes utilising the improved setup, and elaborates on the findings by comparison with the earlier data.

Chapter 5 describes how the multiple parallel crease behaviour properties determined in Chapter 4 are incorporated into finite element simulations in a virtual environment. The deployment sequence of parallel-creased thin Kapton

membranes with one and two creases are simulated using commercial finite element package Abaqus/Explicit, and validated against physical experiments while considering the sensitivity of the simulation to numerical instabilities.

Chapter 6 presents a quasi-static simulation technique to study the deployment behaviour of a simple creased unit, consisting of an intersection of creases. The sensitivity of the simulation results based on various parameters is investigated, and the results are validated against physical experiments.

Chapter 7 concludes the thesis with suggestions for future research.

Chapter 2

Literature Review

This chapter provides an overview of literature on creased membranes, their applications and the past endeavours in simulating their folding and deployment behaviour via numerical/analytical models and experimental investigations. The chapter begins with an introduction to creased membrane structures, typical crease patterns prevalent for use in these structures and their applications. Next, elaborate details on the phenomenon of a crease are presented, reviewing the idealisation schemes available for creases and considering the hinge response at the fold. The final section provides an overview of the existing techniques for characterising the behaviour of crease-lines in thin membrane structures.

2.1 Creased Membrane Structures

A permanent plastic deformation which is localised to a ridge in a membrane, can be referred to as a "crease". Occurring in the nature in the form of butterfly wings as well as in man-made appliances such as the fabric of umbrellas, systematic creasing has been recognised to enhance the performance of otherwise weaker membranes.

2.1.1 Crease patterns

Falling in line with "Origami", the art of folding which offers thin membranes with the ability to convert morphologically and systematically between two-dimensional (2D) thin sheets and three-dimensional (3D) spatial structures [25], specific creasing patterns have been derived targeting possible applications in a variety of industries.

Miura [35] developed one such packaging scheme, better known as "Miura-Ori", where the membrane surface functioned as a mechanical linkage of

thin flat plates connected by frictionless hinges having a single degree of kinematic freedom, i.e. in-plane folding and unfolding. The pattern was developed considering the conditions to be satisfied for a space structure, such as continuous isomeric condition and deployment via a simple, monotonic movement. The subsequent unusual mechanical properties that arise almost exclusively from the geometry of its constituent creases are as shown in Figure 2.1.

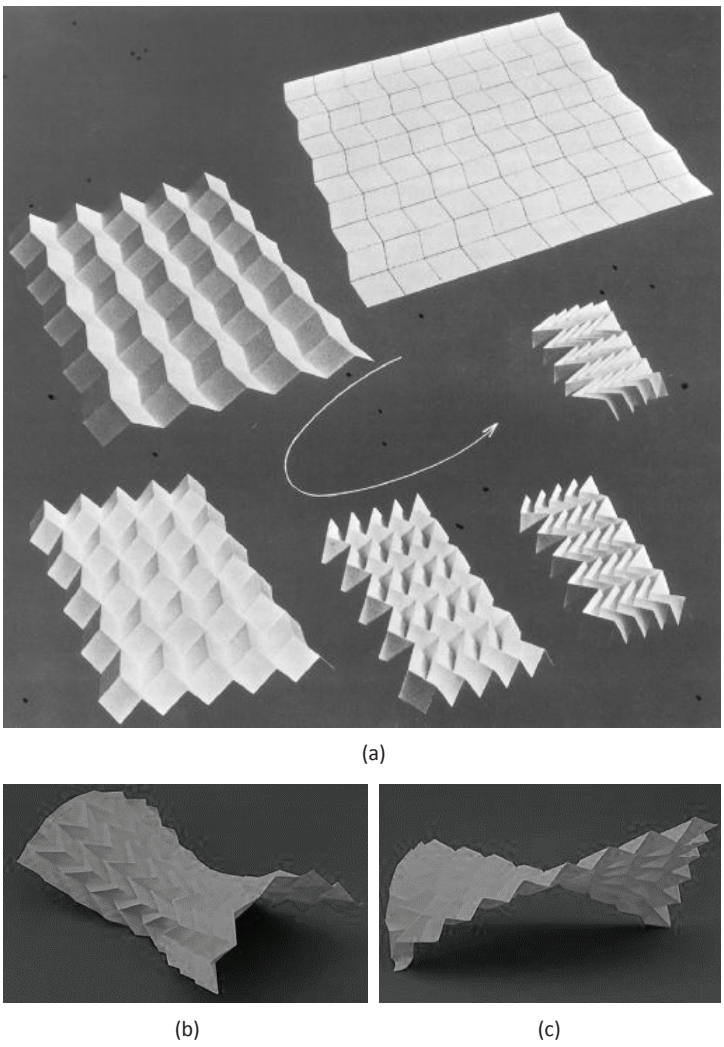

Figure 2.1: Miura-Ori Tessellation [35, 36]
(a) Crease pattern and bi-axial shortening of membrane (b) Saddle-shaped response to bending (c) Negative Gaussian curvature response to twisting

Traditional "Waterbomb" base has two varieties consisting of eight creases and six creases, as illustrated in Figure 2.2 (a) and (d) respectively. Resch crease pattern (see Figure 2.2 (b) and (c)) developed by Ron Resch is one of the

eight-crease base′s tessellations, where four such bases tilt around a smaller square. The interesting property offered by this pattern is its ability to undergo large deformations and change its global Gaussian curvature, without stretching the actual membrane [37]. The tessellations of the six-crease base are more widely used, in the form of a conversion from a flat-foldable surface to a deformable tube referred to as the "Magic Origami ball", as shown in Figure 2.2 (e) and (f).

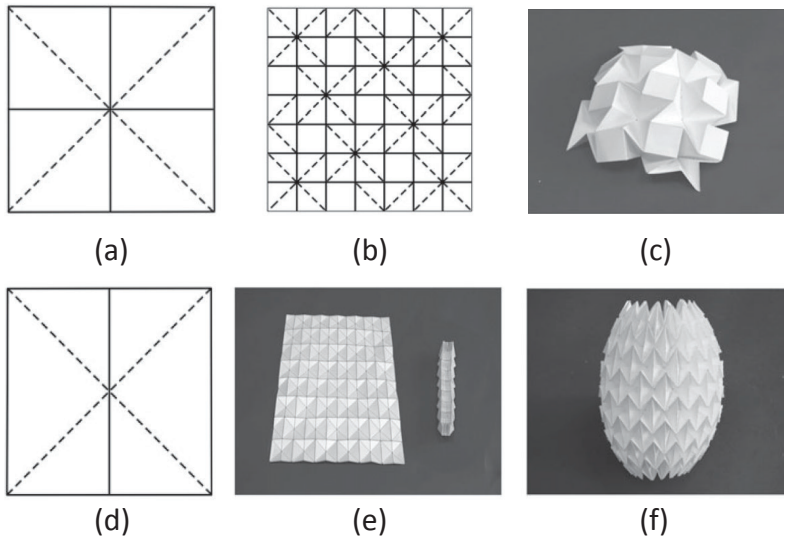

Figure 2.2: Two Waterbomb bases and their tessellations [38] (a) The eight-crease Waterbomb base (b) Resch pattern [39] (c) Partially folded Resch pattern model (d) The six-crease Waterbomb base (e) Unfolded and folded states of its tessellation (f) Magic Origami ball

2.1.2 Applications

Since its overlap with mathematics and engineering, the feasibility of utilising creased membrane structures in the scale of microscopic nano-bots to solar panels on a satellite has been extensively explored.While the significance of employing such structures for applications in space is as explained earlier under Section 1.1, their merit has been recognised by other industries as well.

For example, structures capable of remote, autonomous assembly, along with temperature-sensitive material can be used as "search-and-rescue" bots (see Figure 2.3 (a)) and also to automate steps in manufacturing processes. On the other hand, creating a 3D polyhedron from a flat sheet using creases has been

identified to be one of the best means of modelling the inflation of automobile airbags in a few milliseconds while being sufficiently firm to stop a rapidly-accelerating body, while still providing cushioning [40].

These structures show prospects in the medical field as well. Using the concept of the Waterbomb base described in Section 2.1.1, a heart stent made of plastic materials was developed (see Figure 2.3 (c)) which is capable of being contracted for fitting through a catheter, and subsequently inflated to open up arteries on reaching required positions [38]. Retinal implants are another development that is taking place, which could be built flat for a low cost and elastically compliant to adapt to a variety of retina sizes, as illustrated in Figure 2.3 (b). Creasing techniques would allow the presence of a dense array of electrodes near the retina for transmitting electrical signals from a camera mounted near the eyeball, facilitating regain in vision [41].

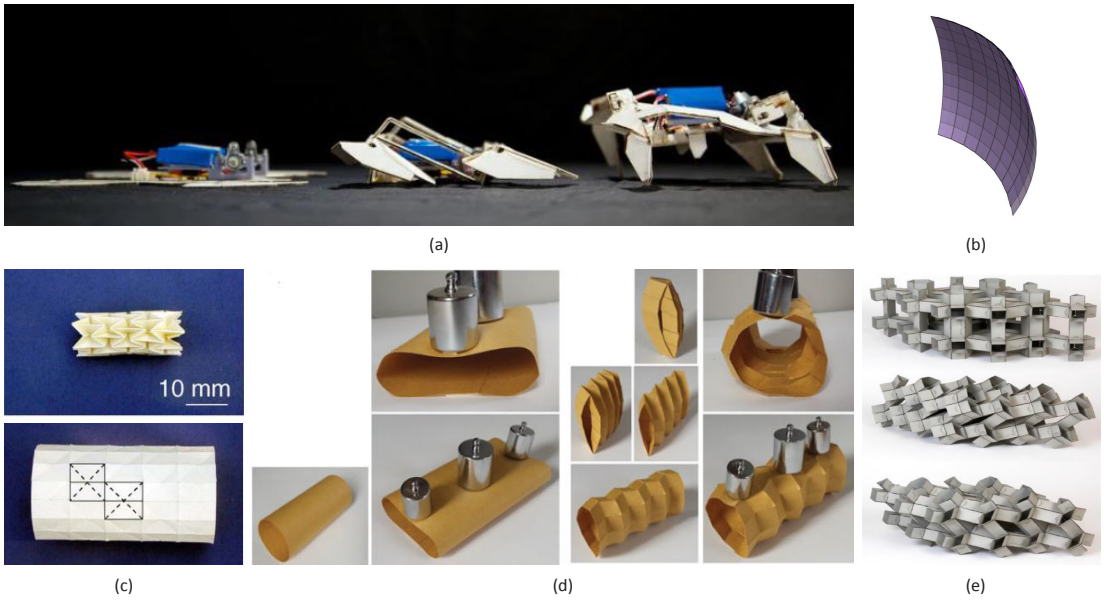

Figure 2.3: Applications of creased membrane structures (a) A robot assembling itself [42] (b) Early design of a retinal implant substrate [41] (c) A card model of the Origami stent graft in its fully folded and deployed configurations [38] (d) Out-of-plane stiffness of Origami zipper tubes (right) in comparison with tubes with zero creases (left) [43] (e) A cardboard prototype of a reconfigurable meta material (top) with its two degrees of freedom (middle and bottom) [36]

Moreover, a new category of Origami tubes with polygonal, translational symmetric cross sections were introduced by Filipov et al [44] where the interlocking of Miura-Ori strips resulted in high out-of plane stiffness of the

tunable structure indicating potential applications ranging from pipes and microrobotics to deployable architecture in buildings (see Figure 2.3 (d)). Reconfigurable meta materials such as the one shown in Figure 2.3 (e) is another result of the enhanced strength and stiffness provided by the incorporation of creases into base membranes.

2.2 The Phenomenon of a Crease

The concept of a fold is commonplace in numerous structures in nature and engineering. A very narrow fold could be considered as a "crease", which could be approximated to have an infinitesimal width in order to obtain a relatively simple geometry [45]. The structure itself is usually seen as an assemblage of rigid faces, coupled around creases exhibiting a behaviour analogous to a hinge [28] with torsional elastic properties, while the overall mechanical response and shape achieved by a creased sheet is found to be programmable by local control of each crease [46], as shown in Figure 2.4.

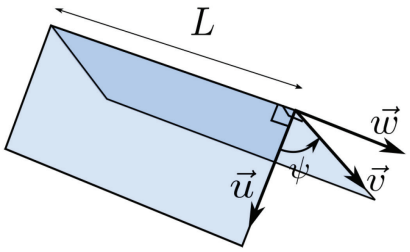

Figure 2.4: The geometry of a single straight crease described by its length L and three unit vectors $(\vec{u}, \vec{v}, \vec{w})$ [46]

2.2.1 Rigid Origami versus Non-Rigid Origami

Rigid Origami is a facet of Origami folding principles categorised in-line with the distinction on face bending and crease actuation. The structure is idealised to be consisting of infinitely rigid faces in bending connected by a series of flexible creases, rendering the latter to be the governing criteria for the shape of the structure at rest.

Although the idealisation schemes in Rigid Origami has given way to achieving a finer interpretation on geometric and kinematic constraints associated with a folded structure while focusing on control of elastic energy as

a means of prescribing the shape-shifts, the actual nature of material utilised in physical applications of Origami exhibit additional soft modes of bending beyond the scope of rigid folding [47]."Non-Rigid Origami" has acquired significance as a result, the effects imposed by the geometric and material nonlinearity associated with flexible thin sheets being crucial in simulating the mechanical response of novel deployable and shape-changing structures.

2.2.2 Hinge Response at the Crease

As explained in Section 2.2.1, despite the approximations, real creases are found to have a finite width, resulting in continuous structural properties. i.e. in actual folded structures, the relative values of bending stiffness of the sheet and torsional stiffness of the crease determines the type of deformation undergone by the sheet on being folded, owing to the two phenomena; face bending and crease actuation competing with each other [28].

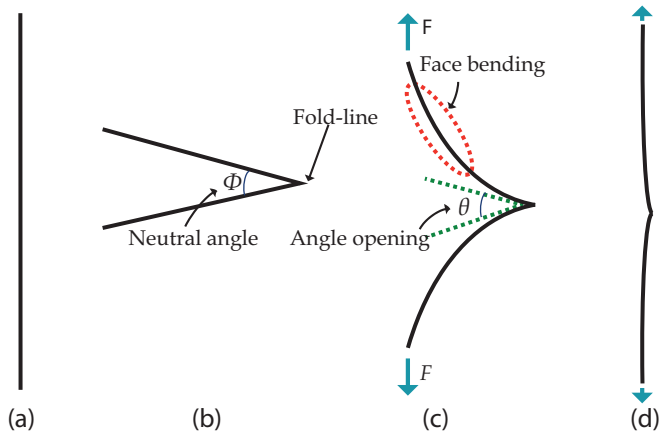

Figure 2.5: Geometric state of membrane [20]
(a) Initial stress-free state (b) New stress-free state after folding (c) Unfolding due to external load (d) Fully unfolded state

Moreover, the underlying mechanics of crease-lines are identified to be twofold; the initial state of equilibrium achieved by the creased membrane by a self-opening action on removal of the creasing load, and the moment−angle response on being subjected to an external load consequently [20].

Stress-Free State on folding

The first response, termed as the "Neutral Angle"− the stress-free state attained by the creased membrane (see Figure 2.5 (a) and (b)) was observed by Papa

and Pellegrino in a simple Miura unit [23]. On removal of the creasing load, it would partially deploy until it reaches an equilibrium configuration. In this study, a square membrane was allowed to expand from its folded state to this state of initial equilibrium, under zero deployment forces. Both physical tests [32, 48] and numerical simulations [49] have been conducted on quantifying and predicting this behaviour, while exploring the effects of creasing pressure, thickness of membrane and material properties.

Moment-Rotation Response

The second response, as illustrated in Figure 2.5 (c) is identified to be a combination of the two characteristics presented earlier in Section 2.2.1; Face Bending and Crease Actuation [50]. The former is dependent on the flexural rigidity of the panels and boundary conditions of the structure, while the latter is dependent on the material properties and method used for crease preparation.

The response of a 25 μm thick aluminized Kapton membrane under diagonal loads applied at the corners was investigated following its naturally expanded state [23]. In-plane stretching of the flat regions of the membrane folded as per Miura pattern of creasing were identified as the primary load-carrying mechanism, together with out-of plane bending of narrow crease regions. It was also observed that the membrane undergoes linear elastic behaviour, for stress magnitudes typical of prevalent solar sail designs.

A simple experimental setup has been utilised by Pradier et al [48] and Dharmadasa [26] for the purpose of characterising the mechanical properties at the crease, as shown in Figure 2.6.

Pradier et al [48] studied the behaviour of creases on 120 g/m^2 printer paper at a macroscopic scale, with the boundary conditions of the specimen being a known load prescribed by increasing weights and a low stiffness hinge. Dharmadasa [26] performed the experiments on 40 mm $\times$ 20 mm Kapton strips of thicknesses 25 μm, 50 μm and 75 μm. The specimens were creased by first carefully bending at the center and then pressing using a roller with a uniform pressure intensity. On allowing the creased specimen to achieve its initial stress-free state, it was attached to a supporting frame using an adhesive tape whose stiffness could be considered negligible compared to the stiffness of

the crease-line, rendering its function as a perfect hinge. The bottom center edge of the specimen was then progressively loaded with light-weight calibrated beads via a hook attached to a nylon string, and photographs of the deformed configuration were taken at each loading step.

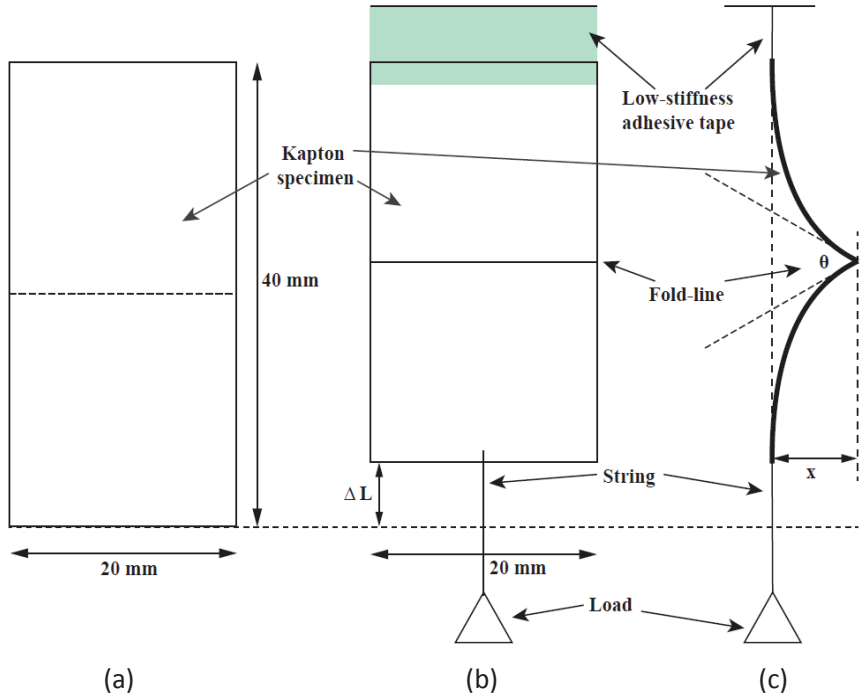

Figure 2.6: Schematic of the experimental setup used to calculate the moment−angle relationship in a crease [26] (a) Specimen before folding (b) Front view (c) Side view after attaching to the frame

The significance of the latter study was the fact that the deformed shape of the specimen (see Figure 2.6 (c)) was a result of both bending of faces on either side of the crease and angle opening, whereas the former study neglected the face bending component by limiting the length of the specimen to the "Origami length scale" (L^*) [51].

By measuring the opening angle θ, defined as the angle between the two tangent lines at the crease, and the horizontal distance between crease and the loaded edge x, the moment exerted by the load at the crease was calculated as per Equation 2.1 [26].

$$M_{applied} = Px \tag{2.1}$$

The applied moment per unit width plotted against the opening angle θ resulted in linear fits parallel to each other for all specimens of same thickness. Specimens of all thicknesses indicated this behaviour leading to the relationship presented in Equation 2.2, where the crease-line response was characterised with the aid of crease stiffness k, independent of neutral angle ϕ.

$$M_{applied} = kw(\theta - \phi) \tag{2.2}$$

where the applied M is measured in Nmm, width of specimen w in mm and all angles are in degrees.

However, the requirement of further physical experiments to confirm the universal applicability of this relationship was highlighted in this study.

2.3 Studies on Creased Membrane Structures

Several approaches have been taken in establishing a generic framework for the folding and deployment behaviour of thin membranes, by the use of both Rigid and Non-Rigid Origami idealisations.

2.3.1 Analytical Studies

An affine map was developed by Belcastro and Hull [52] for describing the folding of a single vertex origami, which was extended by Tachi [53] for simulating arbitrary folding patterns on complex origami sheets. A rotating vector model based on Quaternion and Dual quaternion formulation was proposed by Wu and You [54] for effective capturing of rigid and flat foldabilities of thin sheets, offering prospects in analysing trajectories of multiple vertex patterns on folding. These endeavours were limited to the regime of Rigid Origami.

A model for the prediction of crease topology of transversely creased tape under a tensile load was developed by MacNeal and Robbins [55], based on the elasto-plastic beam theory. The model was capable of predicting the effective elastic modulus and length shortening of creased tapes, and was extended by Murphy et al [56] to a model consisting of a network of creased beams and for randomly creased coated membranes. The limitation of these studies was the assumption that the hinge at the crease behaves elastically at first attaining

perfect plasticity beyond a specific loading, and the effects of the creasing method and resulting residual stresses not being accounted for in the derivation of crease topology [20].

Brunck et al. [46] has attempted expressing the elastic deformation and geometric constraints of crease networks in terms of a vector deformation field. This overcame the shortcomings of the standard approach which does not offer a universal energy minimisation procedure for predicting the three-dimensional shape taken by the structure due to the absence of explicit constraints in terms of opening angles. The study displayed prospects of using vectors supported by crease networks, for characterising elastic deformation and residual stresses and predicting the mechanical response of creased membranes by taking geometric frustration (fundamental incompatibility between the folded geometry and the ensuing mechanical stresses) into account. However, the findings are again limited to Rigid Origami structures, where only the deformation of creases was considered.

Lechenault and Adda-Bedia [51] and Dias et al [57] obtained an expression for the minimum elastic energy of a thin-folded sheet at neutral state using the optimisation technique of Lagrange multiplier, the energy being a function of both panel bending and the crease actuation. However, while the focus of the former study was on the "bistability" of structures with infinitely rigid creases with the snap of vertices locking the kinematics into a deployed state functioning as a mechanical switch, the latter study explored into the "bifurcation" of curvature of closed narrow folds, with the shape and in-plane stretching of the membrane leading to a buckling response.

The realm of curved-line creases has been investigated by Duncan and Duncan [58] in terms of the analytical relationship between pairs of generators linked via two distinct developable surfaces, the shape of original curved path and the variation of the opening angle along it. Theorems were proposed using the Mohr circle of twist and curvature for identifying the kinematic constraint existing between pairs of surfaces for two generator layouts: crease-line remaining a plane curve during deformation and uniform dihedral angle/neutral angle along the curve. Seffen [59] verified these generator layouts using Gauss mapping, replacing the curved crease by a piecewise linear path connecting the vertices of intersecting pairs of hinge lines. The geometric relationships between

the constructed spherical images for folding of successive vertices revealed the operating conditions of the two cases, aiding the synthesis of creasing patterns without complex computations.

Since creased membrane structures are characteristically subject to drastic geometric nonlinearity, most conventional methods are unable to follow the equilibrium path of deformed shape beyond limit points. Dias and Audoly [60] derived a Kirchhoff Rod model for the equilibrium shapes of a thin, annular strip cut out in an elastic sheet, starting from the theory of elastic plates. The derived nonlinear effective constitutive law considered the underlying geometrical constraints where the opening angle of the crease appears as an internal degree of freedom. The significance of this study was the fact that it captured non-rigid deformations of the cross-sections, including finite variations of the neutral angle at the crease.

Pradier et al [48] characterised the fold-deployment behaviour of paper creases, by modelling the crease as a macroscopic local hinge idealised as a nonlinear torsional spring. The model was validated with experiments for straight creases and indicated usefulness in characterising other thin material such as polymer films. However, the model was developed for a monotonic unloading path for a limited range of angles, whereas actual paper creases are used on a wider range of opening angles from 0° (completely closed) to 160° approximately. Liu and Paulino [47] developed a fully nonlinear, displacement-based implicit formulation based on bar and hinge models for performing static/quasi-static analyses of Non-Rigid Origami structures, focusing on global deformations and multi-stable behaviour of some creasing patterns. Mierunalan [20] explored the possibility of quantifying crease mechanics using an analytical model based on the high deflection beam (Elastica) theory, where one half of the thin membrane at a crease was treated as a 1-dimensional beam fixed to a rotational spring at a variable angle $\theta/2$ at each loading stage, taking advantage of the symmetry about the crease-line. However, the accuracy of the results were limited by the inherent assumptions in the Elastica theory and the fact that the derivation does not take the geometric limitations of the specimens into account.

The influence of the crease geometry on the large-displacement flexural behaviour of a 0.2 mm thick creased copper beryllium strip was studied by

Walker and Seffen [45]. In this study, a crease on a tape spring was modelled as a shallow cylindrical segment connected to initially flat side panels. The coupled flexural behaviour of the panels and the crease was considered, and the equilibrium cross-sectional shape for a particular strip curvature was obtained by minimising the strip strain energy per unit length. Even though a crease is often idealised as a singular torsional spring with a linear stiffness, a finite-width crease has portrayed a nonlinear opening behaviour in this study. A linear stiffness of $2D/\beta r$, where D, β and r represent the flexural rigidity, angle subtended across the crease and the initial crease radius respectively has been introduced however, by a reasonable approximation for a singular torsional spring.

As explained above, extensive analytical studies have been carried out on crease-line behaviour by various approximations. However, quantifying nonlinear responses portrayed by creased thin membranes via analytical methods is still in development.

2.3.2 Experimental Studies

Experimental investigations are imperative in quantifying crease-line mechanics, owing to the highly nonlinear nature of material properties and the dependency of crease behaviour on the geometric constraints of the membranes.

A series of experiments were conducted by Gough et al [61] for analysing the nonlinear stress−strain response of creased Kapton membranes. The crease stiffness was observed to be considerably higher than that of the base material, with each crease added to the membrane system leading to an additional compliance, thereby lowering the stiffness of the total system. It was observed that at higher strain levels, the tangent modulus begins to approach that of the pristine base material, where the mechanical effects of creases can be negated. However, it was also highlighted that the operating strain levels of space structures such as solar sails are well below 1%, the range within which creased membranes offer a nonlinear behaviour. Hence, incorporating crease properties to the analysis of deployment of these structures becomes an inevitable requirement.

These findings were confirmed during the uniaxial tests carried out by

Hossain et al [62], where a higher order nonlinearity was identified at the location of the transverse crease, with a linear material response far from the crease. Nevertheless, both these studies were carried out at relatively high stress ranges due to gauging difficulties.

Thiria and Adda-Bedia and Lechenault et al [51,63] investigated the relaxation process and the mechanical response of a single creased Mylar sheet to an external strain. Relaxation in this case was described by an initial quick opening followed by a progressive slow relaxation of the crease, through an Arrhenius activation process (see Figure 2.7). The presence of a resistive moment was identified which remained zero at the neutral angle state, and increased on further opening of the crease beyond the neutral angle. The stiffness of the crease was obtained by the gradient of the linear plot of applied moment versus opening angle, and compared for different thicknesses of the membrane as illustrated in Figure 2.8. Yasuda et al [64] investigated the relationship between the resistive moment and crease angle for a unit paper cell, on being subjected to a compression load. The onset of plastic deformation of the crease with increased membrane stiffness was observed on being compressed up to 80% of neutral angle.

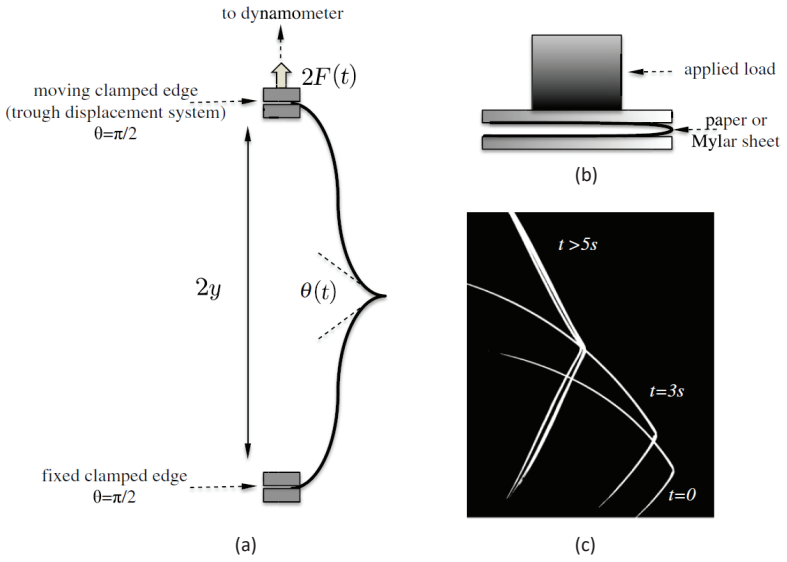

Figure 2.7: Relaxation process and the mechanical response of a single creased Mylar sheet to an external strain [63] (a) Schematic of the controlled experiment; creased sheet clamped on both sides and maintained at a fixed strain $2y$ (b) Illustration of the method of crease preparation (c) Superimposed images of the initial stage of the sheet during the unfolding and relaxation process [63]

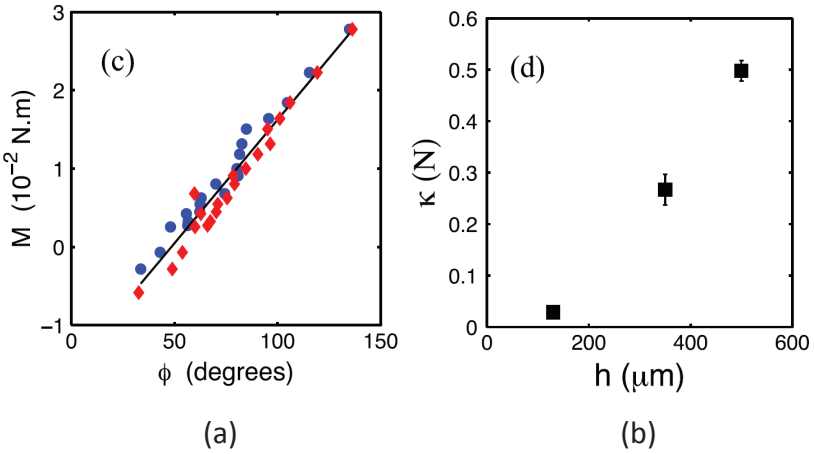

Figure 2.8: (a) Moment–angle relationship for a Mylar sheet of 350 μm thickness (b) Stiffness k for different thicknesses, the error bars being 95% confidence intervals [51]

The crease stiffness of a 0.2 mm thick bistrip of 400 mm × 100 mm dimensions was examined by Dias and Audoly [60], where the endpoints of the membrane at neutral angle state were subjected to a pinching force. The dihedral angle θ_0 and the angle made by the two end points ϕ (see Figure 2.9) were measured for each loading stage f, from which a dimensionless crease stiffness K_r was determined, aided by a parametric analysis.

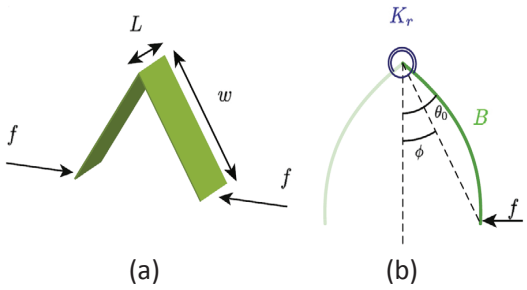

Figure 2.9: Sketch of the pinching experiment used for measuring dimensionless crease stiffness [60]

Dharmadasa [32] obtained a linear response between the resistive moment and opening angle of thin Kapton specimens, as described under Section 2.2.2 and illustrated on Figure 2.10 (a). On gradually increasing the external load, a kinked shape deformation was observed at the crease as indicated in Figure 2.10 (b), which prevents the crease from fully opening up to 180°. However, this analysis

did not take the self-weight of the membrane into account.

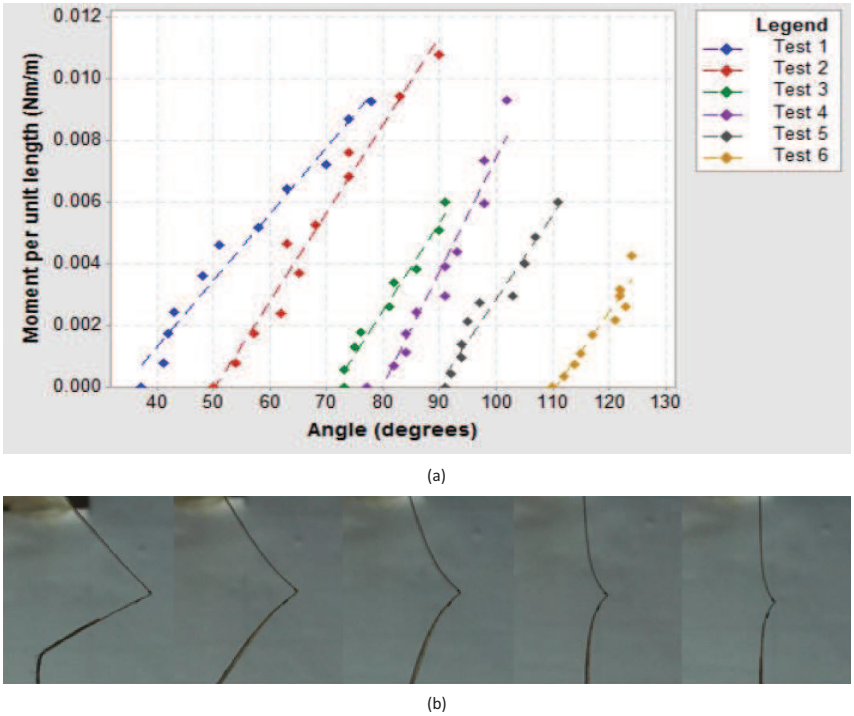

Figure 2.10: Linear response between the resistive moment and opening angle (a) Moment−angle relationship for Kapton 100 HN (25 μm) (b) Deformation profile of Kapton 200 HN (50 μm) [32]

In terms of crease patterns, spinning experiments were carried out by Furuya et al [65], for analysing the centrifugal deployment characteristics of rotationally skew fold for spinning solar sail membranes. However, the global focus of the study was on the specific spin rates and directions for complete deployment and not strictly on crease mechanics.

The need for physical testing of thin membranes has been recognised by previous researchers, as evident from the above studies. Further, experimental investigations serve as reliable inputs for accurate idealisation schemes to be used in analytical/numerical studies, as highlighted by Dias and Audoly [60].

2.3.3 Numerical Studies

The ground tests conducted for the deployment of a 10 m four-quadrant solar sail were simulated using the finite element analysis software packages NEiNastran and ABAQUS by Sleight et al [66]. The predictions of the analysis

were in reasonable agreement with the physical test data, and this study recognised the importance of incorporating accurate material properties, test conditions, and assumptions during numerical analyses.

Woo et al [67] carried out geometrically and materially nonlinear contact analyses to simulate the entire process of creasing and uniaxial tensile testing of 25 μm thick Kapton membranes, as illustrated in Figure 2.11. Initial crease angles were determined for a single crease, and the effective moduli obtained for the crease was found to be dependent on the crease gauge δ. In terms of the self opening action exhibited by creases, Mierunalan and Mallikarachchi [49] and Dassanayake et al [50] carried out creasing and subsequent opening simulations of thin Kapton membranes under a virtual environment with plane strain elements for membrane panels assuming that they are predominantly under bending stress state. The crease was observed locally to take the form of a kink, as shown in Figure 2.12, which was seen during experiments as well [32].

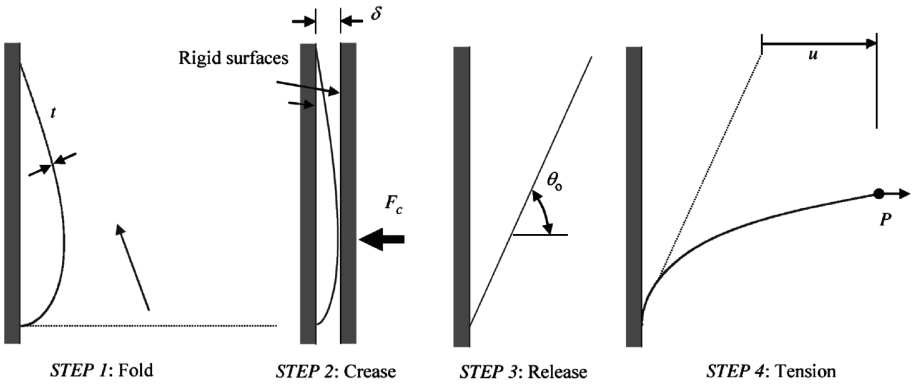

Figure 2.11: Schematic diagram of the steps of simulation for creasing and subsequent uniaxial tensile test of thin Kapton membrane [67]

Crease properties were included into the wrinkling analysis of a rectangular membrane with a single crease under shearing by Wang et al [68] with the aid of residual stresses from creasing, and an effective modulus of elasticity was derived based on the initial elastic modulus of the material. Similarly, Cai et al [31] conducted numerical simulations for the deployment of membrane structures based on Miura-Ori, by incorporating an effective modulus of elasticity for the crease region different to that of the rest of the membrane. It was also highlighted that the loading time plays an important role in the process, in terms of smoother deployment.

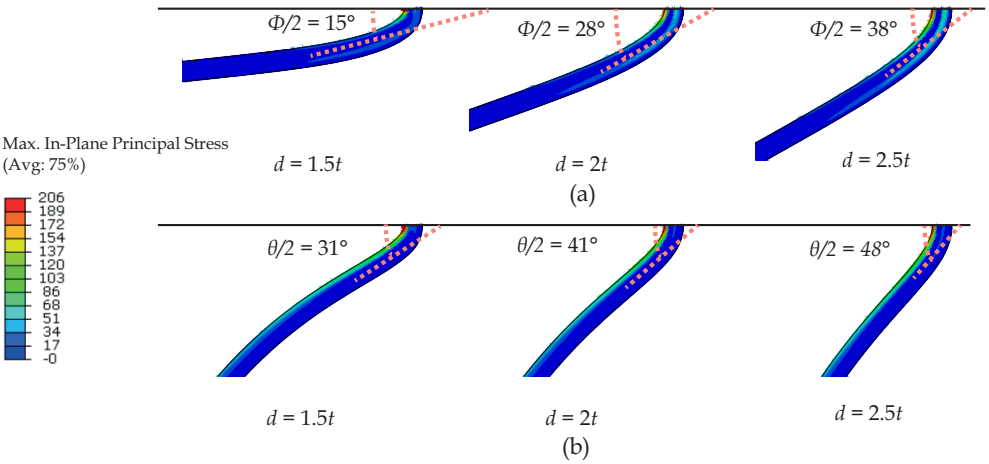

Figure 2.12: Deformed shape of 25 μm Kapton membrane [49, 50] (a) When creased to different creasing gauges (b) When subsequently subjected to 0.4 N tensile load

On observing that the deployment of creased thin membranes are essentially controlled by a much softer bending mode, crease opening was identified to be dependent on the flexibility of faces on either side of the crease as well, in addition to crease stiffness. On the other hand, modelling solar sails with membrane elements led to failure in capturing the panel bending phenomena during deployment. This has resulted in scientists utilising shell approach for idealising creased membranes panels, which is capable of accommodating the material properties and contact responses of the thin membranes on being folded. Papa and Pellegrino [23] and Dharmadasa [26] employed thin shells accordingly, to model the membrane. However, the former study assumed the crease region to have the same stiffness as the base membrane. In contrast, an attempt was made to model the creases with tie constraints and connector elements available in Abaqus Software in the latter study, where the connectors were defined with an experimentally determined rotational stiffness.

Owing to the influence that creases impose on membrane structures (such as solar sails) altering their material states and mechanical response, characterisation of crease mechanics is essential during design optimisation of such structures. Liyanage and Mallikarachchi [69] carried out virtual simulations to assess the possibility of utilising circumferential and spiral folding patterns for large solar sail missions, but considered the membrane to have zero-thickness with no plastic deformation at the creases. The deployment dynamics of a

simplified spinning solar sail system consisting of a central rigid hub, membranes and tethers, based on the concept of IKAROS was studied by Zhao et al [70]. The focus of the analysis was the second stage of deployment of the system, where the deployment of the membrane takes place following release by the guides. A combination of rectangular and triangular thin plate elements were used to model the membrane, with the rate of deployment of the membrane being dependent on tip masses i.e. heavier tip masses led to quicker attainment of equilibrium position. Mierunalan [20] studied the quasi-static deployment of behaviour of a solar sail using Abaqus/Explicit package, creased under the algorithm for inextensional wrapping pattern proposed by Guest and Pellegrino [71] and wrapped around an 8-sided polygonal hub. Although a crease stiffness was incorporated into the model which was determined from numerical simulations conducted on the elasto-plastic behaviour of 25 μm thick Kapton membrane, the deployment force indicated little difference from that obtained for zero stiffness at the crease. This was to be further analysed, since these findings were obtained under the assumptions that the neutral angle of all creases were zero, and that the effect of scoring as the method for creasing can be captured by reducing the stiffness along a crease-line.

Chapter 3

Multiple Parallel-creased Membranes

This chapter focuses on characterising crease-line mechanics of thin membranes with multiple parallel creases using an experimental study. Experiments conducted by Dharmadasa et al. [26] on thin Kapton membranes with a single straight crease are chosen as the background for this purpose, and the limitations in the existing experimental setup have been explored.

3.1 Moment–Rotation Response of Parallel Creases

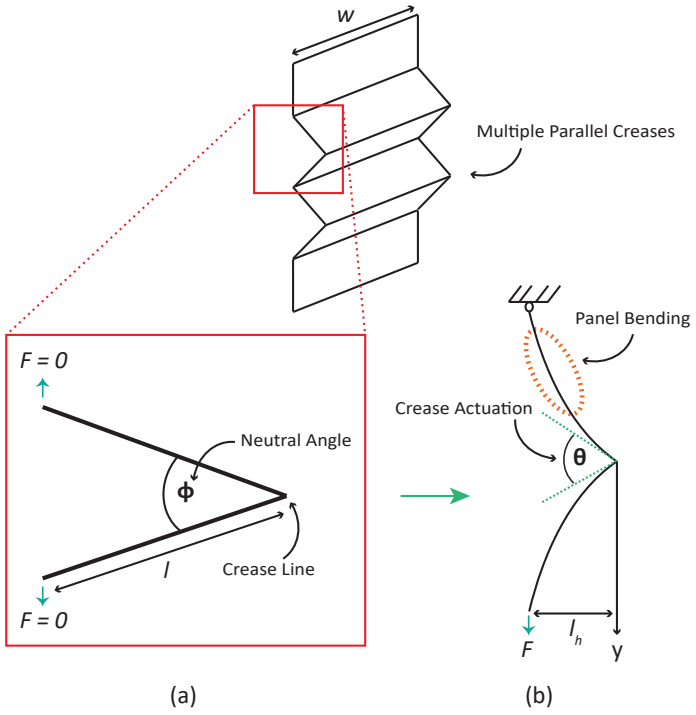

Figure 3.1: Multiple parallel-creased membrane
(a) Neutral angle at stress-free unloaded state (b) Crease actuation and panel bending on being subjected to an external load

This study is focusing on the effect imposed by multiple parallel creases on the deployment behaviour of thin membrane structures, as a result of their unique crease-line properties. As discussed in Section 2.2.2, the hinge behaviour at the crease consists of two components; the self-opening action and consequent crease actuation and panel bending on application of an external load. This hinge response observed for a single crease [20, 26, 50] is considered applicable for the simplest case of Origami−"accordionlike" multiple parallel creases as well, considering the repeatability of crease formation and the similarity in the degrees of freedom; the neutral angle ϕ and the length of the panel l [51] (see Figure 3.1(a) and (b)).

The dependency of the neutral angle ϕ (obtained at the initial stress-free state of a crease) on the type of material, membrane thickness [49], method of creasing, the level of "scoring"−grooves made along the crease-line to facilitate crease formation and applied creasing pressure [72] has been widely recognised. Since the subject of interest is the membrane response to an external load following the neutral angle state, this study will consider 25 μm Kapton 100HN membranes, creased by applying pressure via a known load over a specified time.

3.1.1 Experimental setup

Specimen sizing

Lechenault et al [51] observed that the crease stiffness is characterised by a torsional rigidity parameter κ, with dimension N. A length scale L^* was defined together with the bending rigidity B of panels accordingly, as shown in Equation 3.1.

$$L^* = B/\kappa \tag{3.1}$$

In-line with Equation 2.2, crease opening should be isolated from panel bending, in order to characterise the crease stiffness κ. However, to achieve this, the specimen size l must be limited to L^*, which is approximately 200 times the membrane thickness t [51]. With 25 μm thickness, the limit for panel size becomes 5 mm, which pose issues in handling the specimen and attaching loads and supports. Hence, similar to the experiments carried out by Dharmadasa et al [26] on single creases, each panel was sized to have a length of 20 mm. In deciding the width of the specimen, wider specimens have been identified to

experience non-uniform crease opening, while narrower specimens undergo large deformations due to reduced moment carrying capacity [32]. Therefore, it was decided to use 20 mm wide specimens resulting in square membrane panels, thus striking a balance and limiting panel bending.

Specimen preparation and creasing

The Kapton membrane was marked into 20 mm × 20 mm panels and cut using a sharp blade accordingly, the number of panels depending on the number of creases in between, as shown in Figure 3.2.

The method of creasing followed by Dharmadasa [32] (via roller passes) led to difficulty in quantifying the pressure applied on the fold for creasing. Hence, creasing of the membrane was carried out in two stages, similar to the method followed by Lechenault et al [51]. Initially, the membrane was bent symmetrically by placing the straight edges on top of each other as shown in Figure 3.3 (a), and then a roller weighing 174 g was kept on the bend freely for 3 minutes (without applying external pressure) to form a pre-crease at the desired location (see Figure 3.3 (b)). Then, pressure was applied on each crease by means of a load of 7.05 kg for a duration of 30 minutes to achieve plastic deformation at the crease, as illustrated in Figure 3.3 (c).

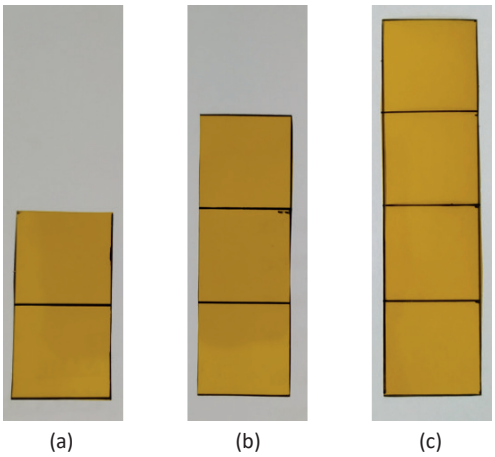

Figure 3.2: Parallel-creased membrane specimens
(a) Single crease (b) Two creases (c) Three creases

On application of the creasing pressure, the specimens were kept undisturbed for a duration of 1 hour for the self opening action of the crease to take place, as shown in Figure 3.4.

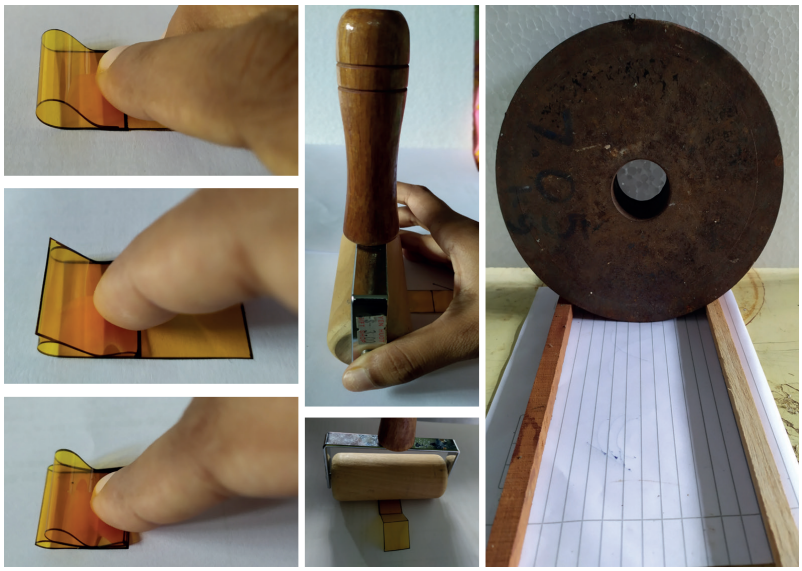

Figure 3.3: Creasing procedure
(a) Forming the bends (b) Forming the pre-crease (c) Applying pressure with a known load over a known time

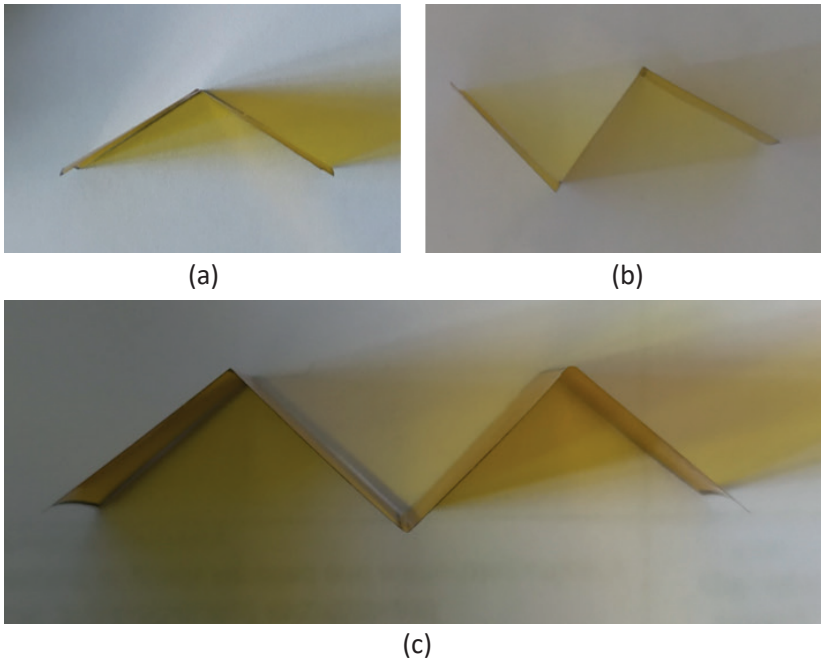

Figure 3.4: Self-opening action of creases
(a) Single crease (b) Two creases (c) Three creases

Boundary conditions

Following the experimental setup utilised by Pradier et al [48] and Dharmadasa [32], the membrane was attached to a timber frame using adhesive tape, having higher rigidity and relatively lower stiffness respectively in comparison with that of the Kapton membrane. Due to the low stiffness of the adhesive tape, the top support of the specimen was considered to behave as a perfect hinge.

A cotton thread was connected to the mid point of the bottom edge and held in place with a low stiffness adhesive tape of 20 mm $\times$ 3 mm dimensions. The adhesive tape running over the entire width of the specimen ensured uniform load distribution. The load steps utilised by Dharmadasa [32] were observed to lack in sensitivity, with even the smallest step (100 mg) leading to a larger opening of the crease. Hence, to capture the moment$-$angle relationship with better accuracy, it was decided to load the bottom edge of the specimen via a combination of plastic and Styrofoam beads weighing 32.2 mg and 3 mg respectively (see Figure 3.5).

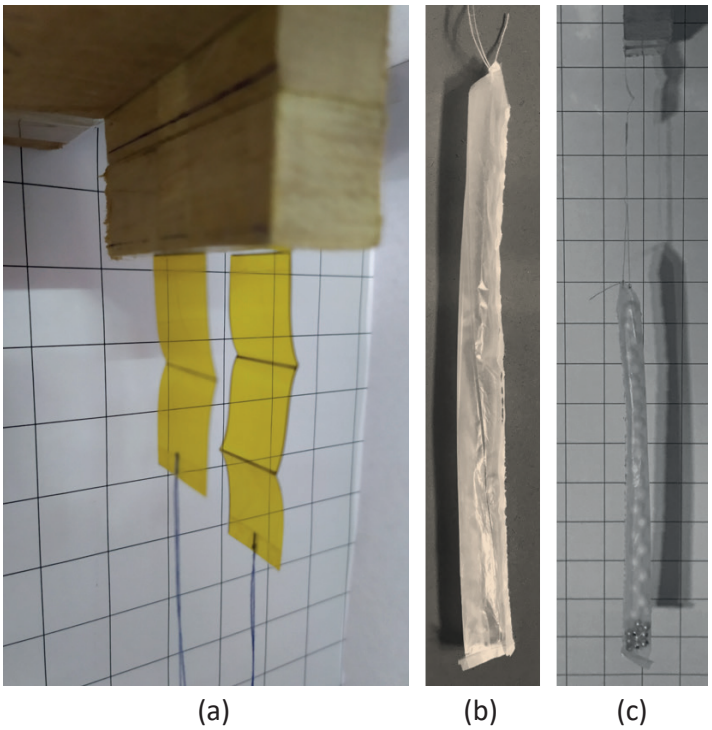

Figure 3.5: Boundary conditions
(a) Perfect hinge support and the loaded edge (b) Attachment to the string for placing the beads and ensuring application of a vertical load (c) Loaded single-creased specimen

3.1.2 Moment and angle measurements

Extreme care was taken during the experiment to ensure that air drag and vibrations are minimised, thereby allowing the membrane deployment to occur solely under the applied calibrated loading. On applying each step of loading, the membrane was allowed to achieve static equilibrium, and an image was taken using a digital single-lens reflex camera (18 megapixel) kept 1 m distance away and in-line with the specimen and sufficiently zoomed in for capturing the entire range of its deployment, as shown in Figure 3.6.

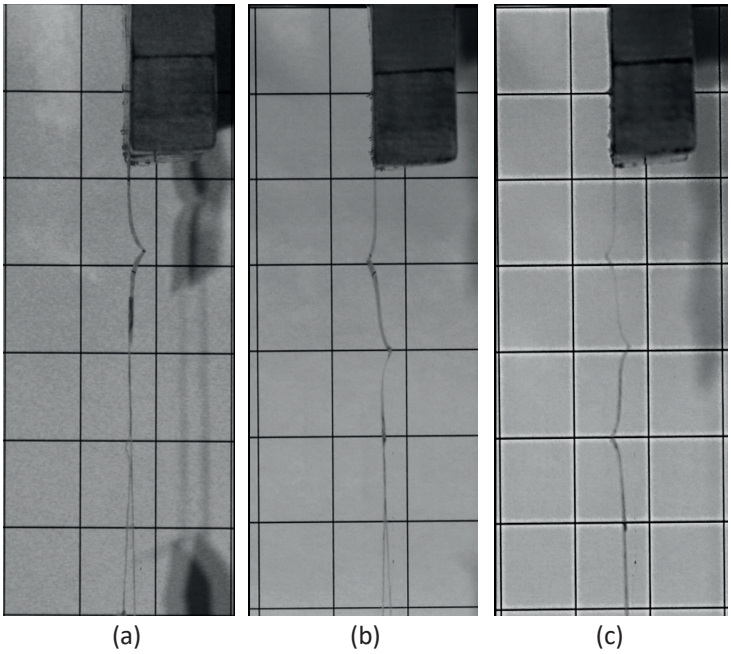

Figure 3.6: Loaded specimens
(a) Single crease (b) Two creases (c) Three creases

As indicated by Dharmadasa [32], image processing was carried out with the aid of the calibration grid fixed in the background of the specimen and WebPlotDigitize tool. Using the coordinates of the creases, loaded edge, support edge and points of maximum curvature in the membrane panels obtained accordingly, the opening angle θ and the horizontal distance between the crease and the loaded edge l_h were calculated.

3.1.3 Self-weight of the membrane

Previous studies on the moment−rotation response of Kapton membranes with a single crease neglected the effect of self weight during the analysis. However,

with a mass density of 1.42 $\mu g/mm^3$, the self-weight of a 20 mm $\times$ 20 mm $\times$ 0.025 mm membrane panel comes up to 14.2 μg. Accordingly, for single, double and triple creased specimens, the self-weight would be 28.4 μg, 42.6 μg and 56.8 μg respectively. It can be seen that these values are in fact prominent during the initial steps of loading, where each step is 32.2 μg. For example, the self-weight of a single creased membrane is approximately 88% of the initial step of loading. Hence, it is evident that the self-weight of the membrane should be incorporated to the analysis, in order to obtain a realistic approximation of the moment−rotation response of the membrane.

With this background, equations were derived for the moment exerted at the crease due to external loading F and self-weight mg of each of the panels (see Figure 3.7) as follows.

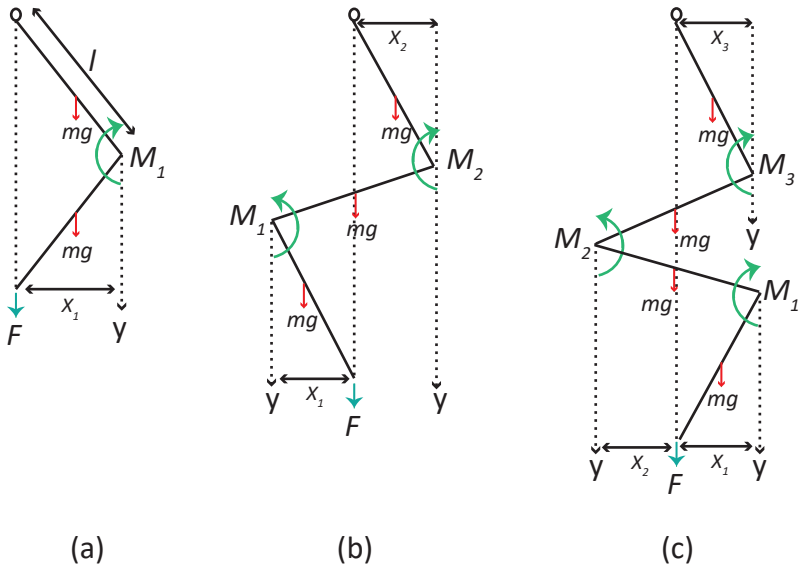

Figure 3.7: Free-body diagram of creases
(a) Single crease (b) Two creases (c) Three creases

Single crease

As shown in Figure 3.8 (a), the moment M_1 at a single crease can be derived as per the Equation 3.2.

$$M_1 = mg\frac{x_1}{2} + Fx_1 \tag{3.2}$$

Two creases

As shown in Figure 3.8 (b), the moment M_1 would be the same as derived in Equation 3.2, due to similar boundary conditions. The moment M_2 can be derived as per the Equation 3.3.

$$M_2 = -5mg\frac{x_2}{2} - Fx_2 \tag{3.3}$$

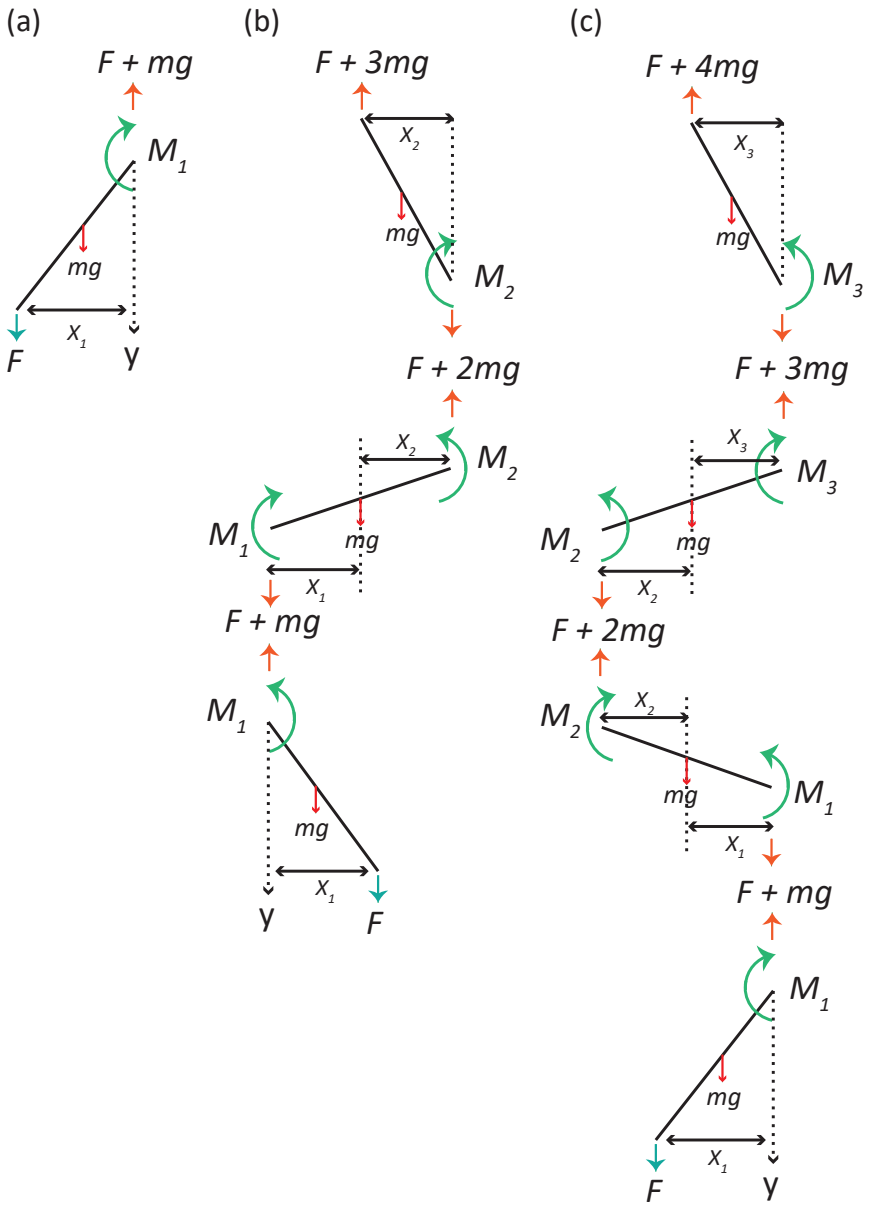

Figure 3.8: Free-body diagram for resistive moment derivation
(a) Single crease (b) Two creases (c) Three creases

Three creases

As shown in Figure 3.8 (c), the moments M_1 and M_2 would be the same as derived in Equations 3.2 and 3.3, due to similar boundary conditions. The moment M_3 can be derived as per the Equation 3.4.

$$M_3 = 7mg\frac{x_3}{2} + Fx_3 \tag{3.4}$$

Accordingly, on calculating x_1, x_2 and x_3 as explained earlier in Section 3.1.2, the resistive moment due to external forces can be computed. By equating this to the resistive moment from the crease defined in Equation 2.2, the moment−angle relationship of each crease could be obtained, in terms of crease stiffness k.

It should be noted that in this formulation, the resistive moment at the crease due to panel bending was accounted for, by direct use of x_1, x_2 and x_3, instead of using the relationship between panel length l and opening angle to arrive at their values ($l\cos(\theta/2)$) .

3.1.4 Time dependence of opening angle

In obtaining the θ and l_h measurements using image processing, it is essential to ensure that the membrane has reached a constant opening angle at each load step. This was investigated by a simple study, where the membrane opening was recorded over time, by subjecting it to two load cases; unloaded and loaded with 50% of the full deployment load, as shown in Figure 3.9 (a) and (b).

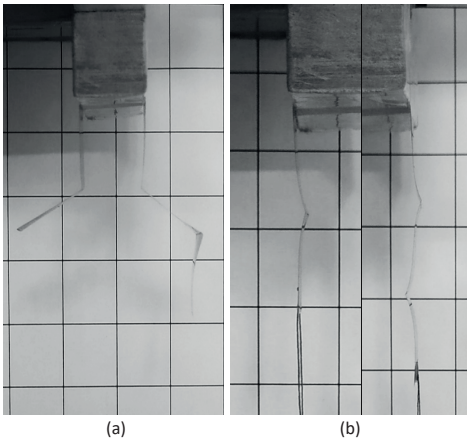

Figure 3.9: Achieving static equilibrium - load cases
(a) Unloaded (b) 50% of full deployment load

Unloaded case

On plotting the opening angles of the specimen versus time, it was observed that the opening angle attains a constant value only after a period of 50−200 hours (see Figure 3.10). This indicates the viscoelastic behaviour of the crease, which will not be taken into account during this study on parallel creases.

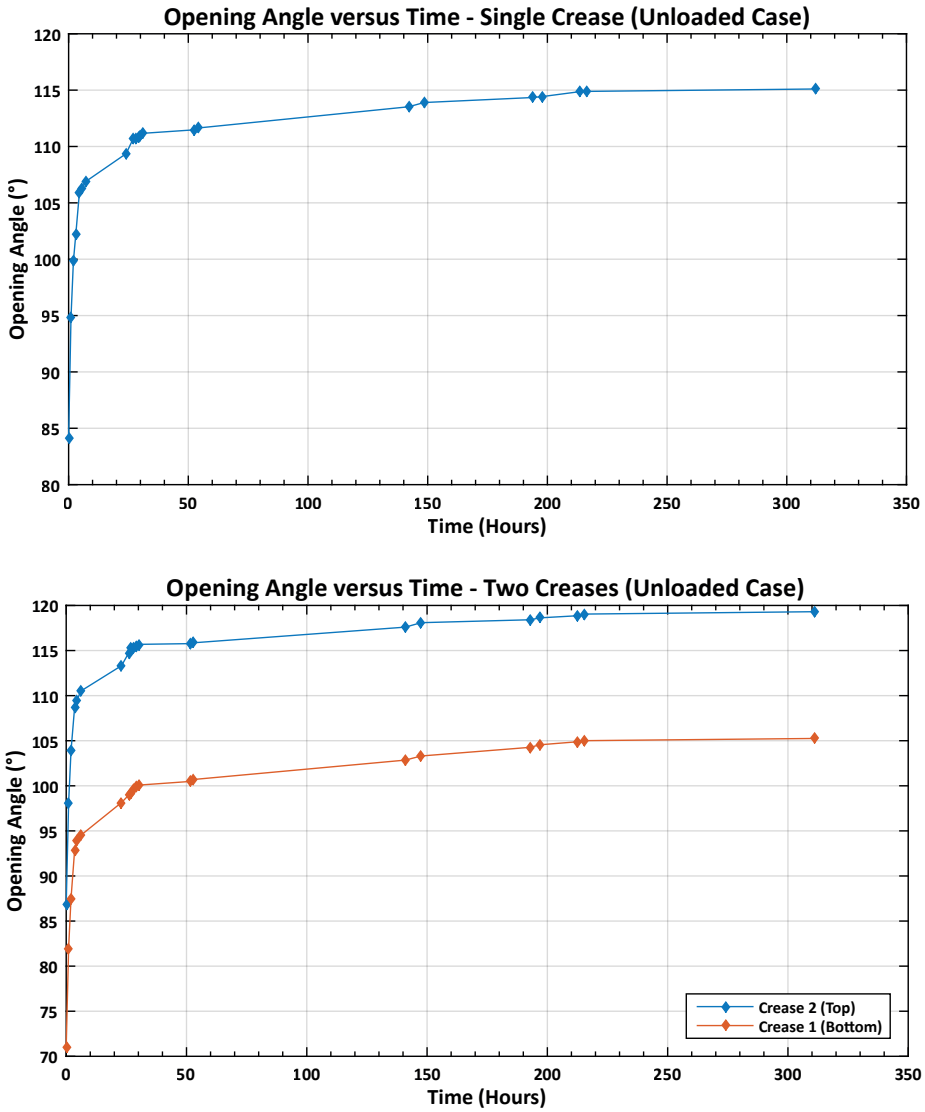

Figure 3.10: Static configuration - unloaded case
Single crease (top) and two creases (bottom)

Loaded case

On loading the specimens with 50% of its full deployment load, a considerable difference was observed in the time taken to achieve a constant opening angle (see Figure 3.11). This change in duration from several hours during the unloaded case to 30−90 minutes during loaded case indicates that loaded specimens attain a constant opening angle quicker than the unloaded case, and hence the measurements taken during the experiments for deployment would not necessarily be affected by viscoelastic effects of the membrane.

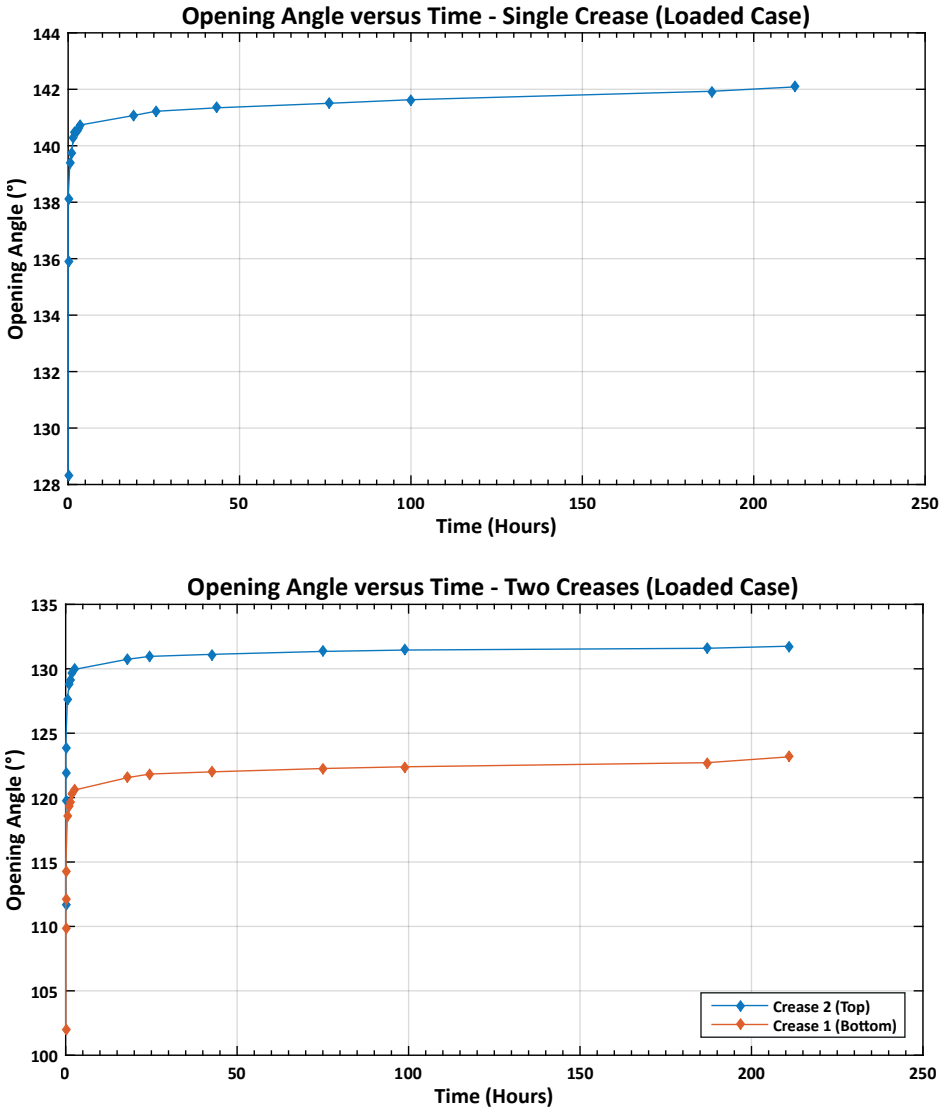

Figure 3.11: Static configuration - loaded case
Single crease (top) and two creases (bottom)

3.2 Results and Discussion

As illustrated in Figure 3.6, a kinked shape deformation was observed at the crease for all specimens, which limits the membrane from achieving full deployment. This was observed in the previous experiments carried out for single creases as well [26]. The moments calculated as per Equations 3.2, 3.3 and 3.4 were divided by the specimen width (20 mm) to obtain the moment per unit width, which was plotted against the $\theta - \phi$ component to assess their relationship. The typical opening angles θ_1 and θ_2, distances x_1 and x_2, along with calculated resistive moments M_1 and M_2 are presented in Table 3.1. Detailed experimental data utilised for the analysis are presented in Appendix A.

Table 3.1: Experimental data for a membrane specimen with two creases

$\boldsymbol{\theta_1}$ *(deg)*	$\boldsymbol{\theta_2}$ *(deg)*	$\boldsymbol{x_1}$ *(cm)*	$\boldsymbol{x_2}$ *(cm)*	$\boldsymbol{M_1}$ $\times 10^{-3}$ *(Nm/m)*	$\boldsymbol{M_2}$ $\times 10^{-3}$ *(Nm/m)*
62	67	1.08	0.87	0.67	0.66
67	75	1.03	0.81	0.80	0.75
77	77	0.96	0.75	0.90	0.81
80	79	0.91	0.69	0.99	0.85
82	82	0.86	0.66	1.08	0.92
84	85	0.83	0.61	1.18	0.95
88	90	0.78	0.60	1.22	1.02
89	91	0.76	0.56	1.31	1.04
93	92	0.74	0.51	1.39	1.02
93	94	0.71	0.50	1.45	1.09
93	94	0.68	0.48	1.50	1.13
94	94	0.66	0.48	1.55	1.20
95	95	0.65	0.47	1.63	1.24
96	96	0.62	0.41	1.67	1.17
96	97	0.61	0.41	1.72	1.21
97	97	0.58	0.39	1.75	1.23
98	98	0.58	0.38	1.83	1.26
99	99	0.57	0.37	1.88	1.28
99	100	0.56	0.35	1.92	1.28
101	101	0.53	0.35	1.93	1.29
103	103	0.50	0.33	1.93	1.30
104	104	0.49	0.33	1.95	1.32
106	104	0.49	0.31	2.02	1.33
106	104	0.49	0.30	2.06	1.28
107	105	0.48	0.29	2.04	1.25
108	106	0.47	0.28	2.06	1.23
109	107	0.47	0.27	2.08	1.25

Moment−angle plots were produced for 25 μm thick Kapton membrane specimens with one, two and three creases, as illustrated in Figures 3.12, 3.13, 3.15 and 3.16. All the plots indicate a reduction in moment beyond a certain opening angle, which suggested that the membrane has undergone axial tension at (and beyond) that point [20]. The set of data where the moment monotonically increased with the opening angle were fitted to linear regression models, from which a constant crease stiffness k was derived for each type of specimen. It has been identified by previous studies that this value is not dependent on the particular neutral angle, i.e. creasing pressure [32]. However, as shown in Figure 3.13, unloading curves for each crease indicated a stiffness slightly higher than that of the loading curve, implying a higher resistive moment from the crease for same angle opening.

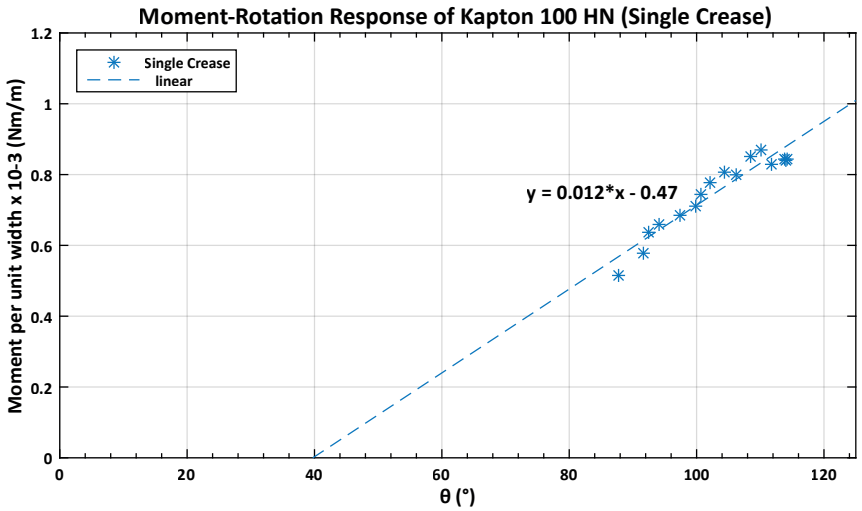

Figure 3.12: Moment−rotation relationship for a single crease

In order to assess the effect of the location of the crease (closer to the pinned boundary) and measurement inaccuracies on poor alignment of the camera with the specimen (shift of the membrane to the side), further experiments were conducted on specimens with two creases, by placing the specimen in four different orientations. Figure 3.14 illustrates the considered orientations of the specimen with numbered creases to facilitate identification, while the obtained moment−rotation plots are presented in Figure 3.15. On comparing the results obtained for each orientation, crease stiffness was found to be dependent on the location of the crease and independent of the shift of the membrane during deployment.

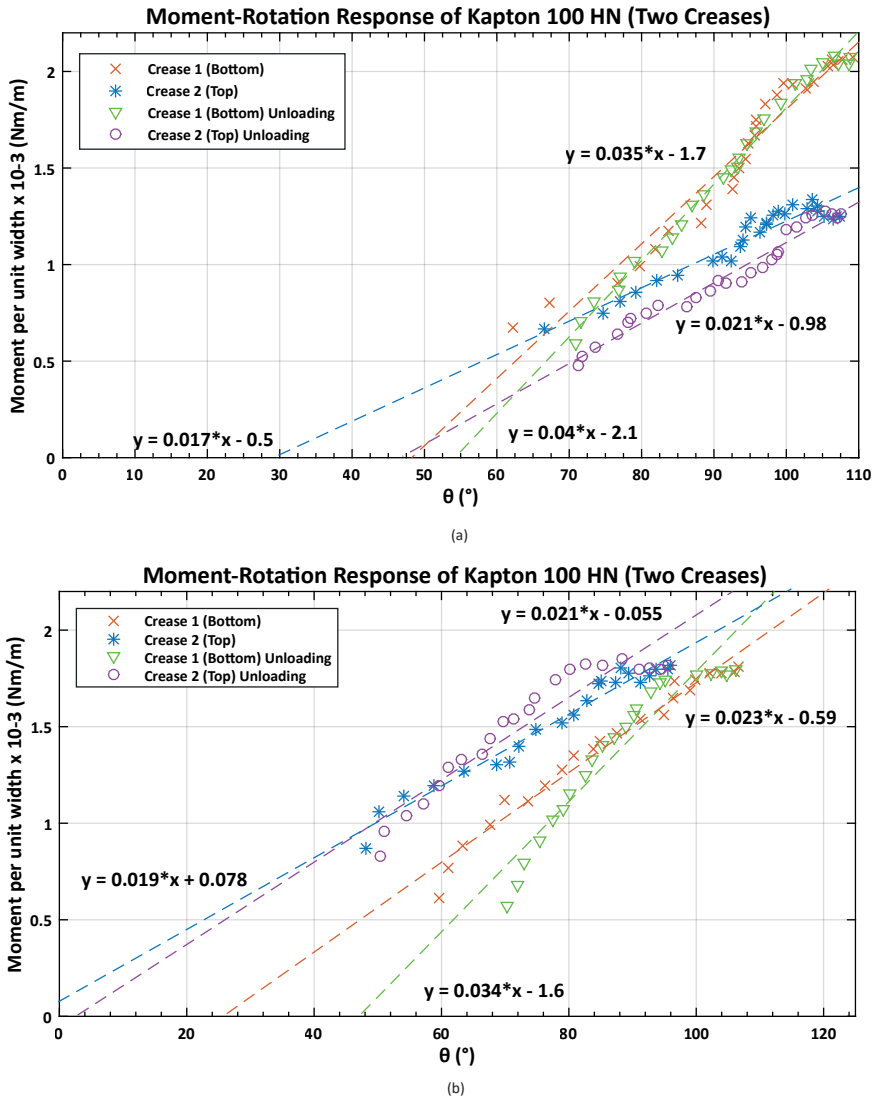

Figure 3.13: Moment−rotation relationship for two creases
(a) Specimen 1 (b) Specimen 2

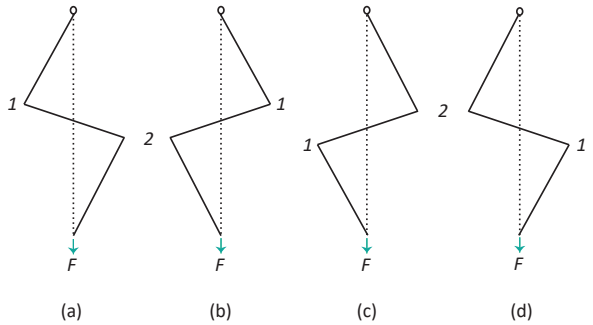

Figure 3.14: Orientations of the specimen
(a) Orientation 1 (b) Orientation 2 (c) Orientation 3 (d) Orientation 4

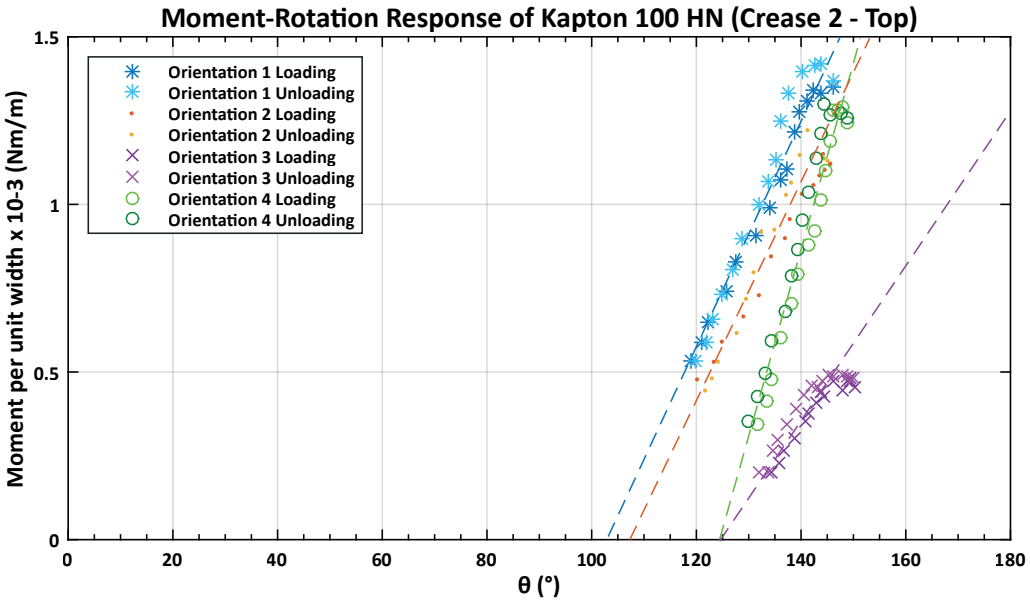

(a)

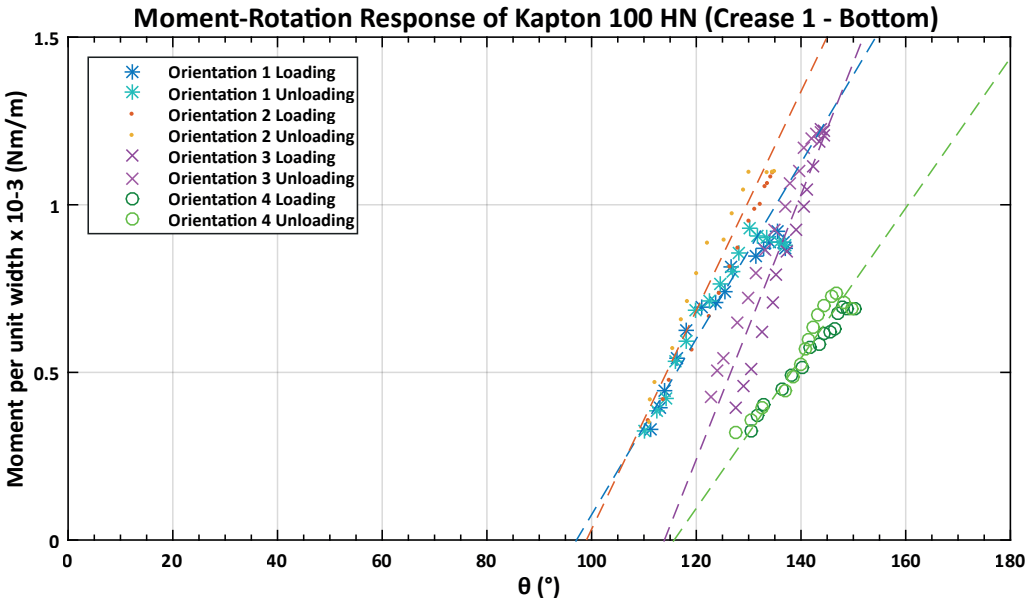

(b)

Figure 3.15: Moment−rotation relationship for two creases - different orientations (a) Top crease (b) Bottom crease

The experiments carried out on specimens with three creases indicated an interesting behaviour, where the crease nearest to the pinned boundary was found to depict a considerably different crease stiffness from the the other two creases (see Figure 3.16). This was observed for all four orientations of the specimen, which could be attributed to the non-uniform contribution of panel bending on either side of the crease to its resistive moment, which should be further investigated.

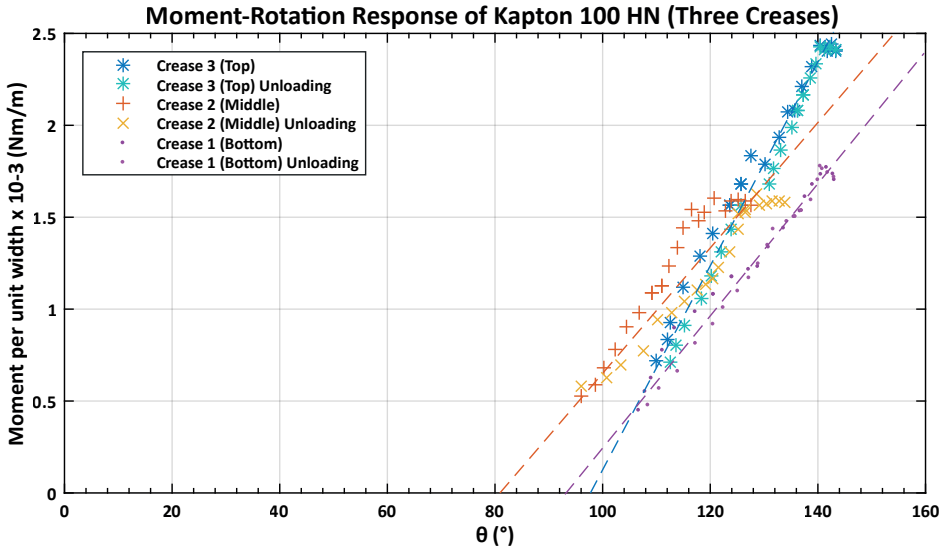

Figure 3.16: Moment−rotation relationship for three creases

Table 3.2 presents the stiffnesses obtained for the best linear fit of each set of crease data accordingly, along with their coefficients of determination (R^2), established through the regression analysis.

Table 3.2: Summary of crease stiffnesses obtained via regression analysis

Type of specimen		**Crease stiffness k** (N/deg)		R^2 (%)	**Sample Standard Deviation S (σ)**	
Single Crease		0.000012		91.2	0.0000012	
Two Creases	Top	0.000032	0.000031	93.7	0.0000061	0.0000071
	Bottom	0.000029		95.1	0.0000063	
Three Creases	Top	0.000041	0.000036	98.9	0.0000023	0.0000015
	Middle	0.000033		93.5	0.0000021	
	Bottom	0.000033		98.7	0.0000028	

The values are observed to be lower than the values obtained during the

simulations carried out by Mierunalan [20] and experiments carried out by Dharmadasa [32] for 25 μm thick Kapton membranes with a single crease, by an order of 10. However, the experiments carried out were more precise in comparison to the earlier investigations owing to the lower least count of loading steps enabling better capture of the moment−rotation response, and since it accounts for the significant effect of self-weight as explained earlier in Section 3.1. On the other hand, the finite element simulation technique does not account for specimen preparation and viscous behaviour of Kapton, and is yet to be validated with other materials. Nevertheless, the applicability of the obtained result for different thicknesses of the Kapton membrane should be further investigated.

3.2.1 Limitations in the existing experimental setup

The main limitations identified in the existing experimental setup utilised by Dharmadasa [32] were the insufficient sensitivity of load steps and the absence of a method for controlling deployment of the creased membrane. Even though the sensitivity of load steps were improved as explained under Section 3.1.1, the disturbances occurred during placement of the calibrated loads in the attachment to the string was still identified to affect the accuracy of measurements, by contributing to the shift of the membrane and exerting additional forces on the membrane beyond calibrated loading. On the other hand, the validity of assuming the pinned boundary condition required to be assessed, which is a key criterion in the resistive moment formulation. Subjecting creased specimens to external loading by controlling the displacement of the membrane was identified to be a plausible alternative in this regard, in the form of an improved setup capable of ensuring proper alignment and boundary conditions of the membrane, thereby minimising the measurement errors as well.

Chapter 4

Improved Experimental Setup

This chapter focuses on describing the features of the improved experimental setup shown in Figure 4.1, elaborating on the purpose of each of the components for facilitating controlled displacement and precise deployment force measurement.

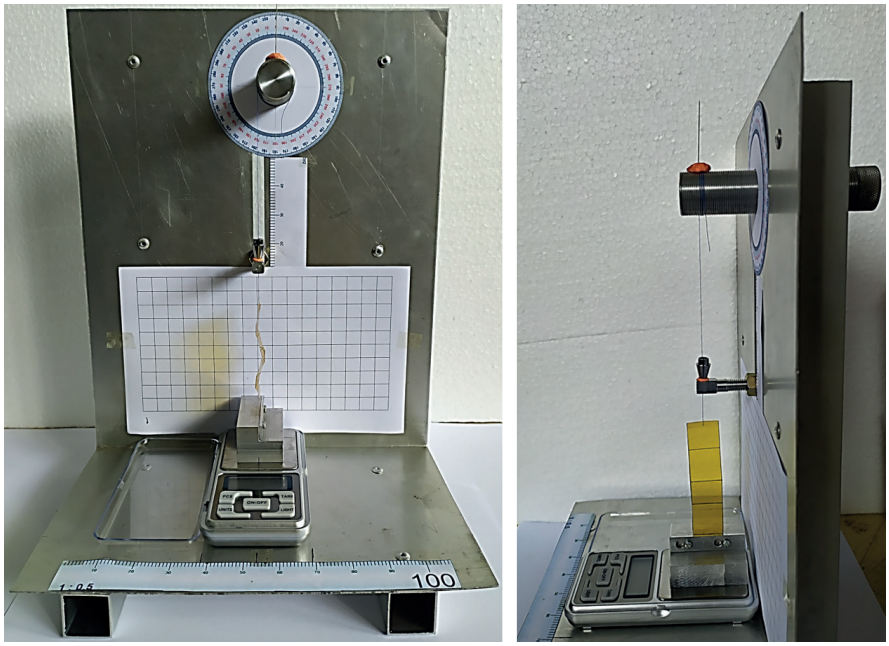

Figure 4.1: Improved experimental setup
(a) Front view (b) Side view

4.1 Controlled displacement

Displacement control was identified to be an accurate alternative in comparison to the force (via load steps) controlled deployment method followed in the

earlier setup.

This was ensured by attaching the free end of the creased membrane specimen to a string of negligible weight, which passed over a thread bar, capable of being rotated about its axis for changing the provided displacement as required (see Figure 4.2). The circular scale attached to the frame concentric with the thread bar, along with the indicator serves as a guide to control the displacement. The pitch of the thread was 1 mm, and the diameter of the thread bar was selected such that a complete turn results in 7.5 cm displacement−well above the full range of displacement provided to the specimens. This ensured that the back and forth motion of the string along the thread bar is limited, thereby maintaining a constant alignment during the full duration of the experiment.

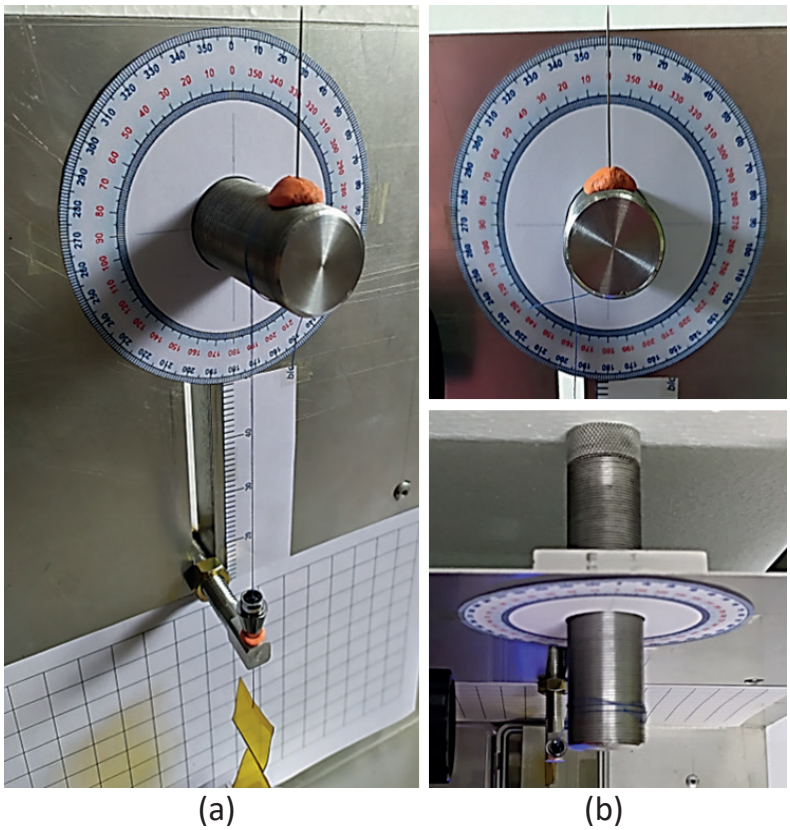

Figure 4.2: Controlling displacement
(a) Arrangement for displacement control (b) Circular scale and indicator (top), thread bar and knob for precise control (bottom)

4.2 Force measurement

4.2.1 Measuring scale

Previous experiments on creased membranes revealed that full deployment of the specimens of concern occurs at a load range of 0 to 1.5 g. Therefore, it was imperative to select a measuring scale with a minimum precision of 0.1 g. Available spring balances in the market were either uneconomical or lacked in precision. A compression controlled electronic measuring scale with 200 g full capacity and 0.01 g precision was selected accordingly.

The accuracy of the measuring scale needed to be assessed, since the opening response of creased membranes indicated a high load sensitivity. The scale was calibrated with SHIMADZU−ATX224 high accuracy analytical balance with 0.0001 g precision, and the measurements taken by the scale were found to be satisfactorily accurate for the full range of loading, as shown in Figure 4.3.

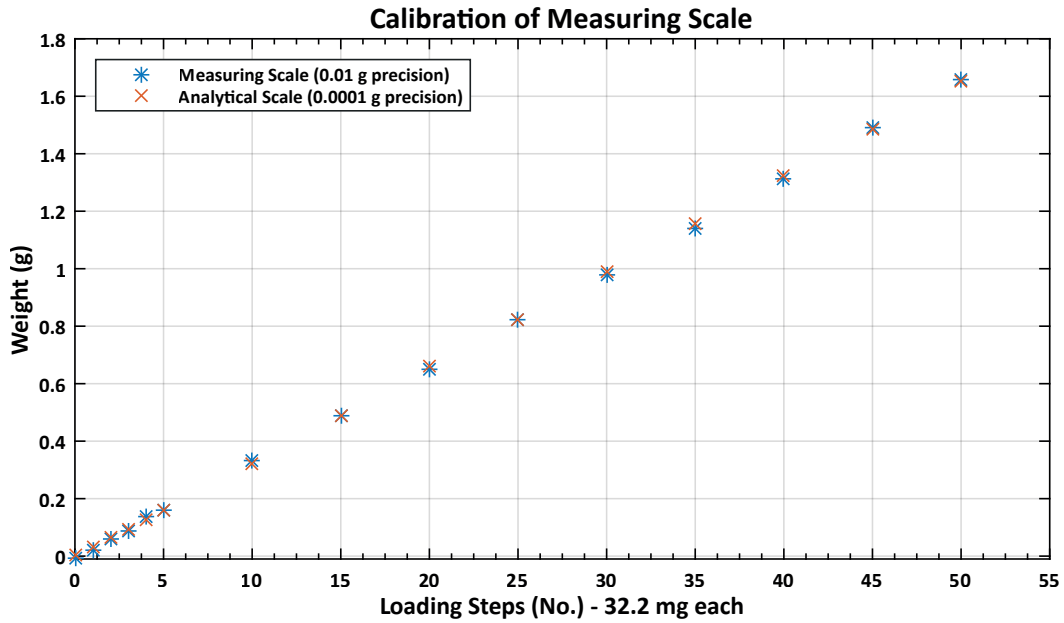

Figure 4.3: Calibration of measuring scale

Since the scale was designed for usage only under compression loading, it was required to preload the scale, following which the force measurements would be taken by means of the reduction in the preloaded reading due to applied displacement to the membrane.

4.2.2 Extension of the thread

Since the thread acts as the main component transferring the provided displacement to the membrane specimen, it was required to ensure that the extension of the thread is minimal during the overall deployment process. On carrying out a simple experiment, it was identified that the percentage elongation of the thread for full range of loading was approximately 0.015%, which was considered acceptable.

Additionally, the measuring scale indicates a continuous increase in reading (in contrast with the expected reduction in the reading due to the preload) on increasing displacement when stretching of the thread commences, which serves as an indicator on the maximum ratio of deployment D/D_f (where D and D_f refer to deployed length and initial length of specimen respectively) attainable by a creased membrane.

4.3 Boundary conditions

The boundary conditions were to remain as in the earlier setup; pinned support at one end, loaded on the other. As described under Section 4.1, loaded edge was attached to a thread for facilitating controlled displacement. However, it was noted that the selection of the size and type of the adhesive tape should be done with care, to avoid its effect on the perfect hinge condition at the support. Adhesive tapes of 20 mm $\times$ 3 mm dimensions and minimum thickness available in the market (approximately 20$-$30 μm) were chosen accordingly (see Figure 4.4 (a)), the width just sufficient to hold the specimen in place and to arrive at the loading configuration.

For the pinned edge of the specimen, an arrangement was made as shown in Figure 4.4 (b), where the specimen was held in place via two flat metal surfaces bolted together. The specimen was attached to one of the flat surfaces using an adhesive tape strip of similar sizing as described earlier, and then locked in position using the other flat plate on top, while taking care to ensure that a slight gap is present between the support and the specimen. The latter precaution was taken to prevent the formation of a plastic hinge at the support, which would render the pinned boundary assumption invalid.

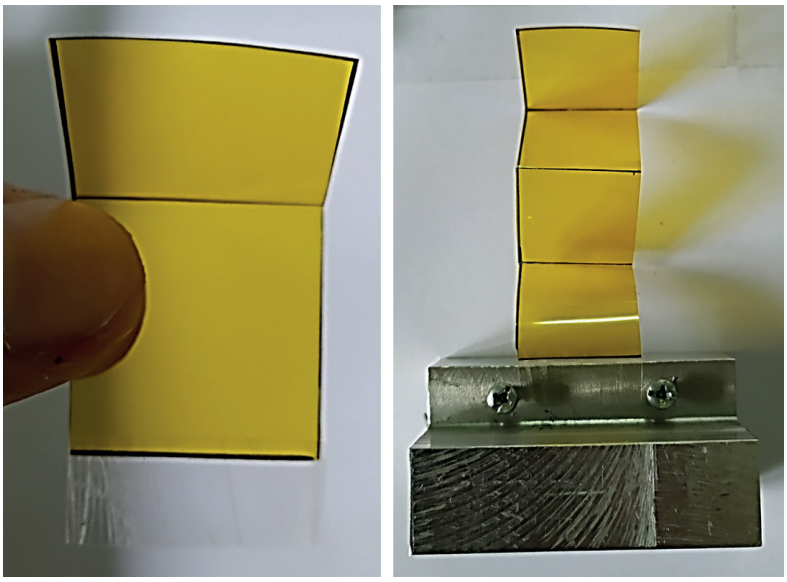

Figure 4.4: Boundary conditions
(a) Adhesive tape (b) Pinned boundary

The attachment which was utilised for the pinned support served as the preload for force measurements as well, as shown in Figure 4.1.

4.4 Horizontal and vertical alignment

Due to the extreme sensitivity of the nature of the experiment, maintaining accurate vertical and horizontal alignments was considered to be of utmost importance. Markings were made on the platform of the setup to indicate the position of placement of the measuring scale and the preload/pinned support attachment, vertically aligned with the thread bar and string at the top of the specimen. The component shown in Figure 4.5 (a) (with a 0.1 mm diameter slot) was used to ensure that the string remains vertical throughout the deployment process, so that the direction of loading remains constant.

Moreover, in order to facilitate conducting experiments for membranes of different lengths and widths, a second thread bar was placed in the setup, as illustrated in Figure 4.5 (a) and (b). This is capable of moving in both vertical and horizontal planes and being held at a desired location, guided by the attached vertical ruler.

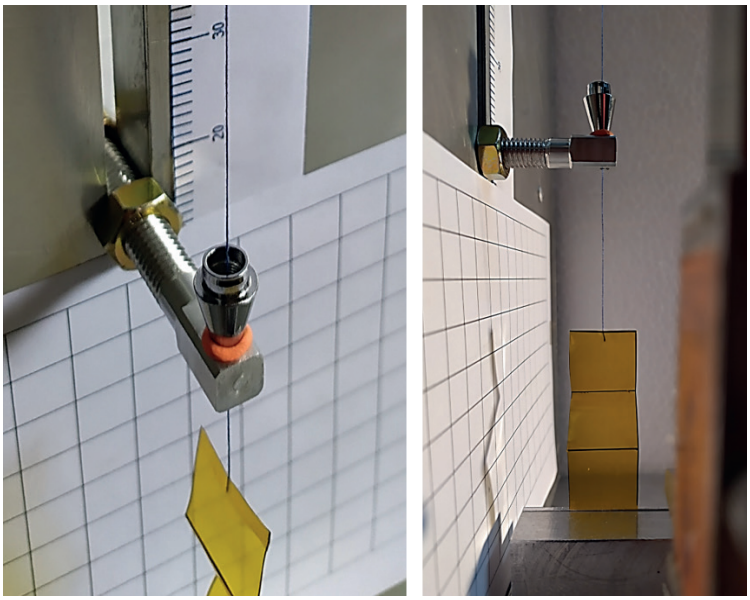

Figure 4.5: Additional components
(a) Component for maintaining verticality of string (b) Component for facilitating testing of different specimens

In addition to the aforementioned controls, the vertical alignment of the specimen, and horizontal and vertical alignments of the setup were ensured via spirit level prior to each experiment.

4.5 Results and Discussion

Experiments were carried out on 25 μm thick Kapton membranes with one, two and three creases using the improved experimental setup (see Figure 4.6), following the method of specimen preparation explained in Chapter 3 and ensuring proper alignment of the specimen via available controls.

While the displacement control feature in the setup was used for deploying the specimen free of external vibrations, the actual displacement of the specimen, opening angle θ and l_h were measured via image processing, as in the earlier experiments. The force measurements were taken directly from the scale, but the work carried out against the gravity was accounted for, by using modified equations during the calculations.

In order to assess the effect of the enhanced features of the setup on the

accuracy of the moment−rotation response obtained, the deployment of a single crease was given focus. Accordingly, the moment−angle plots obtained for a single crease are as illustrated in Figure 4.7.

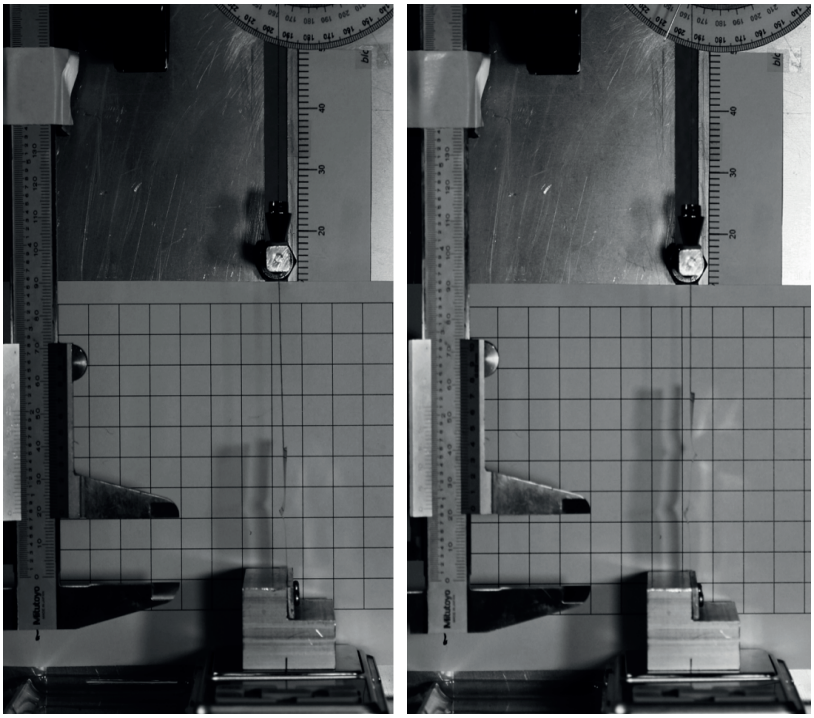

Figure 4.6: Improved experiments
(a) Single crease (b) Two creases

It can be seen that all the plots follow a linear relationship with an approximately equal gradient irrespective of the neutral angle in each case (which is dependent on the creasing procedure), which was observed in the earlier experiments as well. Table 4.1 presents the summary of the crease stiffnesses obtained for each specimen along with the results of the linear regression analysis.

By averaging the values of stiffness obtained, a single value was determined for the crease stiffness of a single crease, 0.0000214 N/deg. This value would be incorporated to virtual simulations for the purpose of predicting the deployment behaviour of membrane specimens with two and three creases.

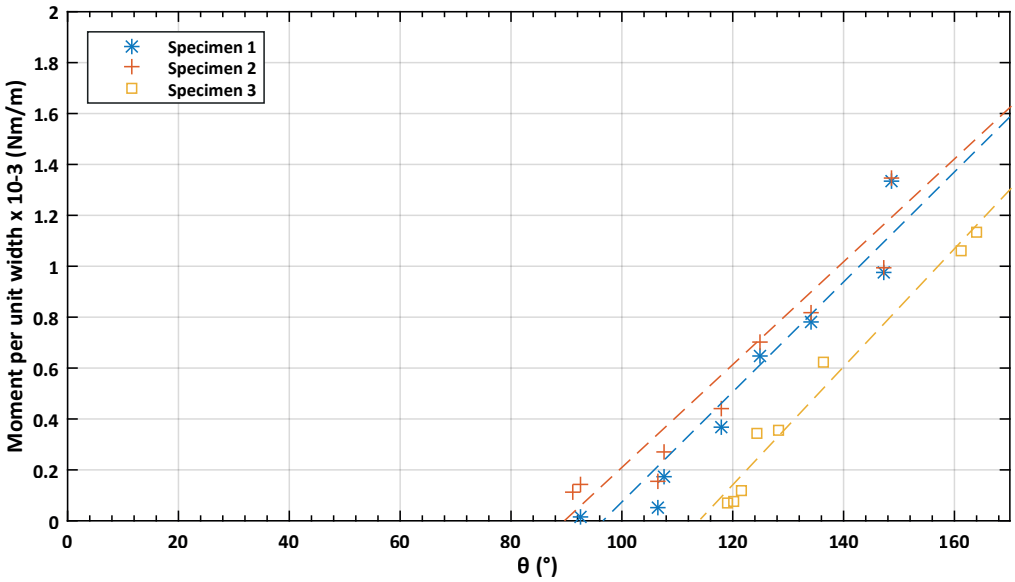

Figure 4.7: Improved moment−rotation relationship for a single crease

Table 4.1: Single crease stiffness

Specimen No.	**Crease stiffness** $\boldsymbol{k}$ (N/deg)	$\boldsymbol{R^2}$ (%)	**Sample Standard Deviation S** (σ)
1	0.000020	93.7	
2	0.000019	91.8	0.000001
3	0.000023	98.6	

Chapter 5

Implementation in Finite Element Package

This chapter discusses the implementation of crease-line properties (obtained via physical experiments and presented in Chapter 4) in numerical simulations for the purpose of predicting the deployment behaviour of parallel-creased membranes.

5.1 Modelling the crease-line and membrane panels

It has been identified that the crease-line width, in fact develops in the same order as the thickness of thin membranes [73]. While several attempts have been taken by previous researchers on deriving an accurate representation for the material properties along this crease-line [31, 62], the simulation technique where the crease-line is idealised as a rotational spring [20, 32, 51], to which the estimated crease stiffness can be incorporated is identified to be the most fitting approach.

On the other hand, owing to the extremely low order of magnitude of the thickness of thin membrane panels in comparison with the other two dimensions, the panels could be idealised as shell elements. The use of shell elements holds significance in terms of capturing the face bending phenomena on either side of the crease as well.

Mierunalan [20] proposed the use of a series of 2-noded connector elements with zero thickness, placed at a reasonable spacing for the purpose of maintaining connectivity between adjacent membrane panels (represented by Kirchhoff shell elements) and for incorporating the rotational elasticity at the crease.

Figure 5.1 illustrates the local axes and vector definitions for a crease region and a connector element respectively [20]. By the definition in Figure 5.1 (a),

the relative rotations about local direction 1 are expected to be predominant. Rotations about the other two directions are restricted due to the plastic deformation and resulting weakening of crease material. This analogy aligns well with the deployment behaviour observed in Chapters 3 and 4. Figure 5.1 (b) indicates how the connector element replaces the crease region, with the defined local axes representing that of the crease region. By imposing kinematic constraints for rotations about 2 and 3 local axes and allowing free rotation of node b about the shared axis 1, the rotation θ of node b relative to node a could be defined.

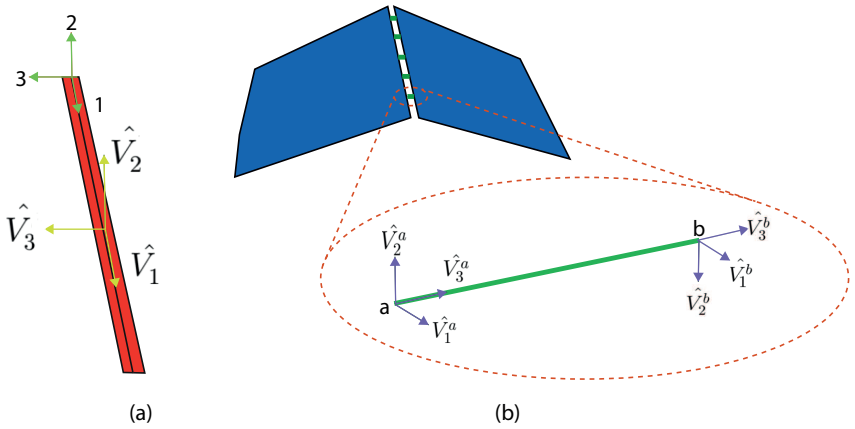

Figure 5.1: Local axes and vector definitions for (a) crease region (b) a connector element [20]

Assuming that the initial angular position of the connector is zero at the folded state, the defined rotation θ equates itself to the connector constitutive rotation. Accordingly, the kinematic moment M_c in the connector can be related to the internal resistive moment at the crease as in Equation 5.1.

$$M_c = M_{resistive}\hat{V}_1^a \tag{5.1}$$

where, the internal resistive moment developed at the crease on application of an external load is defined as per the Equation 5.2.

$$M_{resistive} = kw(\theta - \phi) \tag{5.2}$$

5.2 Finite element model of multiple creased thin membranes

An attempt is made in this section to simulate the deployment of a creased membrane with two and three creases in a commercially available finite element

software. The aforementioned connector definition is utilised for incorporating the estimated crease stiffness to the analysis.

Since this simulation is concerned with the opening of creased membrane panels starting from its folded configuration, the capabilities in representing accurate contact behaviour and the functionality of specific connector types is imperative. Abaqus/FEA is recommended owing to its robust algorithm facilitating these features [20, 32, 49] and its extensive usage in aerospace-related applications.

5.2.1 Finite element model of membrane with two creases

Following the experiment, 25 μm thick Kapton membrane panels of 20 mm $\times$ 20 mm dimensions were modelled, connected to each other in a zig-zag manner representing the parallel creases. The use of Static/General analysis step posed difficulties in solving the numerical model, since the relatively thin membrane is subjected to high curvatures during the simulation. Hence, Abaqus/Explicit solver was used instead considering its proven efficiency in solving quasi-static problems with contact, and handling discontinuities such as dynamic snapping (substantial changes in geometry in a limited time interval) prevalent in complex simulations.

Utilising shell elements for the purpose of representing membrane panels was based on their capability in capturing in-plane stresses as well as out-of-plane bending of the panels. However, in selecting the exact shell element to be used for the simulation from the readily available types, their relative accuracy in capturing such behaviour must be assessed, along with the computational efficiency and cost-effectiveness in utilising them. The merits of 3-noded and 4-noded general purpose, finite-membrane-strain shell elements were compared between their fully integrated (S3, S4) and reduced integrated (S3R, S4R) formulations accordingly, and S3 elements were selected for the numerical model. S4 elements were eliminated due to its computationally expensive nature for bending simulations with contact in comparison with the S4R elements (4 integration points per element versus single integration point), while S4R elements were eliminated due to poor accuracy as a result of their susceptibility to hourglassing.

Nevertheless, a refined mesh is required to capture bending deformations and minimise mesh distortion at the creases, since S3 is a linear shell element with constant strain approximation [74]. This requirement is further highlighted since the Abaqus/Explicit solver supports only linear elements [32]. As indicated in Figure 5.2, a typical finite element model consisted of 2972 shell elements and 1789 nodes with a minimum element length of 0.5 mm.

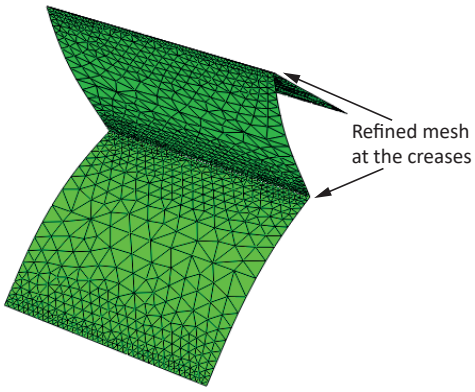

Figure 5.2: Mesh refinement at the crease

The material properties of Kapton used in the virtual simulations are as presented in Table 5.1.

Table 5.1: Material properties of Kapton used in the finite element simulation of multiple creased membrane

Property	**Magnitude**
Density (kg/m^3)	1420
Elastic modulus (MPa)	2500
Poisson's ratio	0.34

The boundary conditions of the specimen were modelled so that the simulation sequence follows the process of the physical experiment carried out. One edge of the specimen was restrained with a pinned boundary condition, allowing free rotation. A displacement equal to the full displacement achieved in the physical experiments (56 mm) was applied to the mid point of the free edge of the specimen. However, the deployment of the creased membrane was simulated starting from the fully-folded state of the specimens, and not from the initial stress-free state as in the experiments. Here it was assumed that the crease stiffness during self-opening (k_r) is the same as that observed on being

subjected to an external load (k_o).

Modelling the crease initially requires maintaining the connectivity between the shell portions using **TIE constraints* without rotational degrees of freedom. Since *Revolute* type connector elements offers the user with the ability to specify a single desired rotational degree of freedom between two points [20], its two-node 3D elements (CONN3D2) were selected to be used consequently for defining rotational elasticity at the crease. A linear **CONNECTOR, ELASTICITY* behaviour was assigned to the connector elements assuming a constant stiffness in both its states of self-opening and opening under external loading as presented in Equations 5.1 and 5.2, owing to the absence of experimental data on k_r. The average value of k (0.0000214 N/deg) obtained for a single crease (see Table 4.1) was used as the rotational spring stiffness accordingly, uniformly distributed among the connectors along the crease-line.

The arrangement of connector elements at the crease was as follows; two shell portions (membrane panels) are displaced by a distance equal to the thickness of the membrane [32], and connector elements are placed perpendicular to the crease-line by connecting the shells at specified nodes located with 2 mm spacing (see Figure 5.3). This particular value for spacing was decided based on a sensitivity study carried out by Mierunalan [20] on the optimum number of connectors to be used along the crease-line. In assigning the connector element, it was ensured that the local axis 1 of the connector is aligned parallel to the membrane edge at the crease, affirming that the opening behaviour is as explained in Section 5.1.

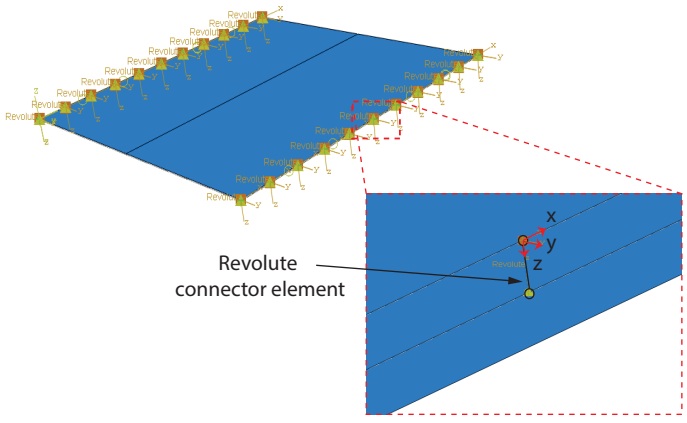

Figure 5.3: Node-based connectors placed perpendicular to the crease-line

5.2.2 Abaqus/Explicit Solver

The use of Explicit solver over the Standard/Implicit solvers has both its merits and demerits. Implementing Euler central difference time integration rule with the use of diagonal or "lumped" element mass matrices, the explicit operator solves for dynamic equilibrium at the beginning of each increment [20,32]. Inertia becomes a significant factor in determining the stability of the solver which is conditionally stable, based on the stability limit specified in Equation 5.3 for the minimum time increment Δt.

$$\Delta t \leqslant \frac{2}{\omega_{max}} \left(\sqrt{1 - \xi^2} - \xi \right) \tag{5.3}$$

where ξ and ω_{max} denote the fraction of critical damping in the fundamental frequency mode and the highest eigenvalue in the system respectively.

The focus here is specifying a stable time increment which is sufficiently small for capturing the propagation of the out of balance forces applied to the mode, to adjacent elements as stress waves. This stability limit is defined based on the "Courant" condition i.e. the time taken for a wave to travel between adjacent nodes in the finite element mesh [75]. Accordingly, the minimum stable time increment becomes a function of the shortest length of finite element in the model l_{min} and the dilational wave speed c_d, with the dilational wave speed expressed by the following equation.

$$c_d \approx \sqrt{\frac{\mathrm{E}}{\rho}} \tag{5.4}$$

where E and ρ denote modulus of elasticity and material density, respectively.

As per the above definition, the natural frequency (ω_{max}) of the model, material properties (E and ρ) and the minimum size (l_{min}) of the finite element are key determinants of the maximum size of the minimum stable time increment. However, this leads to computationally expensive simulations if the systems are modelled in their natural time periods with loading rates

maintained as in actual physical experiments. Increased loading rate, application of viscous pressure and mass scaling are some of the means of artificially increasing the speed of the process for arriving at an economical numerical solution.

Even though initially utilised for high speed dynamic simulations, the Explicit solver was used in this specific study considering its capability in solving quasi-static problems with contact, given that the inertial effects are minimised and thereby maintaining the time increments at their stable limit. Assessing the soundness of the Explicit analysis and verifying its accuracy can be carried out by examining the energy history of the simulation. The typical energy balance equation utilised in Abaqus/Explicit is as indicated in Equation 5.5.

$$E_{total} = E_i + E_{vd} + E_{ke} - E_{wk} \tag{5.5}$$

where E_i is the summation of elastic, inelastic strain energy and artificial energy (collectively referred to as the internal energy), E_{vd} is the viscous dissipation, E_{ke} is the kinetic energy and E_{wk} is the work done by the external forces.

The level of convergence of the numerical solutions can be identified by the presence/absence of discrepancies in the aforementioned energy balance. For the analysis to be devoid of any numerical instabilities such as hourglassing or shear locking etc.,the artificial energy should lesser than $1-2\%$ of internal energy, with the kinetic energy not exceeding $5-10\%$ of internal energy [34].

5.3 Results and Discussion

5.3.1 Sensitivity of the simulation for membrane with two creases

Load rate specification

When utilising an increased load rate for the simulation, Abaqus [34] recommends a time scale of 10 times the natural period of the system as an initial estimate, since higher loading rates have the tendency of amplifying the dynamic responses on failure to achieve a compromise. However, for the finite element model of the

parallel-creased membrane with two creases described under Section 5.2.1, a time scale of 3 s was chosen by a trial and error process of ensuring that the kinetic energy is maintained within the limits of 1−5% of internal energy throughout the simulation (see Figure 5.4).

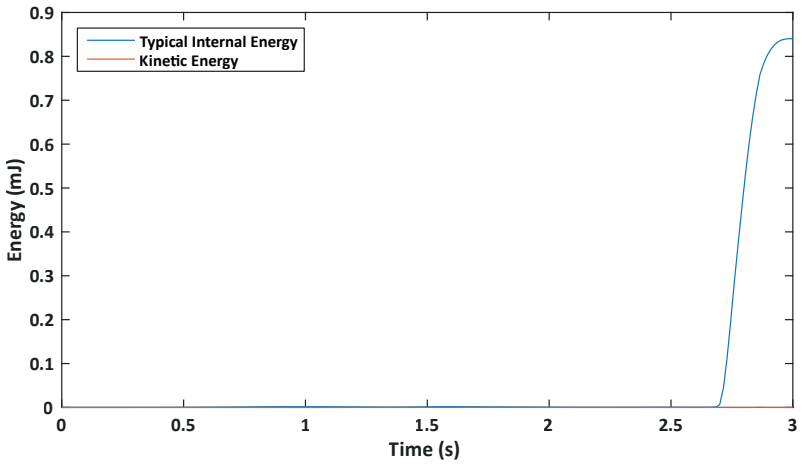

Figure 5.4: Comparison of kinetic energy profile with the internal energy profile of the finite element simulation for membrane with two creases

It should also be ensured that the generation of any considerable inertial effects within the model is prevented during the application of the load/displacement. Smooth application of load/displacement is imperative for maintaining the quasi-static condition in the simulation. Accordingly, an amplitude was defined for the loading step of the analysis using the Abaqus/Explicit command **Amplitude, Definition = Smooth Step*, which was capable of eliminating the accelerations imposed on the membrane structure at the initial and final stages of the step. However, slight peaks were observed in the kinetic energy plot during middle stage of the simulation which indicates the requirement for viscous damping, for the numerical model to be free from instabilities throughout.

Application of viscous pressure

The deployment simulation of the creased membrane indicated dynamic behaviour, which violated its quasi-static equilibrium during the loading step of the analysis. Viscous pressure loading was applied as the means of damping the observed dynamic instabilities in a minimal number of time increments. The normal velocity-dependent viscous pressure applied on the surfaces is

characterised in terms of a damping coefficient c_v. This coefficient should be specified such that the membrane structure is not over-damped, which would lower the accuracy of the analysis results obtained in the process. Abaqus [34] recommends an initial estimate for c_v to be a value below 2% of ρc_d, defined as in the Equation 5.6.

$$\rho c_d = \rho \sqrt{\frac{\mathrm{E}(1-\nu)}{\rho(1+\nu)(1-2\nu)}} \tag{5.6}$$

where ν denotes the the Poisson's ratio of the material of the membrane.

The value of ρc_d becomes equal to 2×10^{-3} for Kapton material (see Table 5.1) as per the above definition. Following an initial estimate of 4×10^{-5} for c_v (at the 2% limit of ρc_d) and by a trial and error process for minimising excessive deformations of the structure, 2×10^{-7} was chosen as the final value for the damping coefficient, facilitating quasi-static deployment.

The energy balance of the simulation is illustrated in Figure 5.5. The total energy for this simulation remains close to zero throughout the simulation, and the artificial energy lies in the range of 1% of internal energy. Negligible viscous dissipation energy indicates that the deployment is unaffected by the applied viscous pressure.

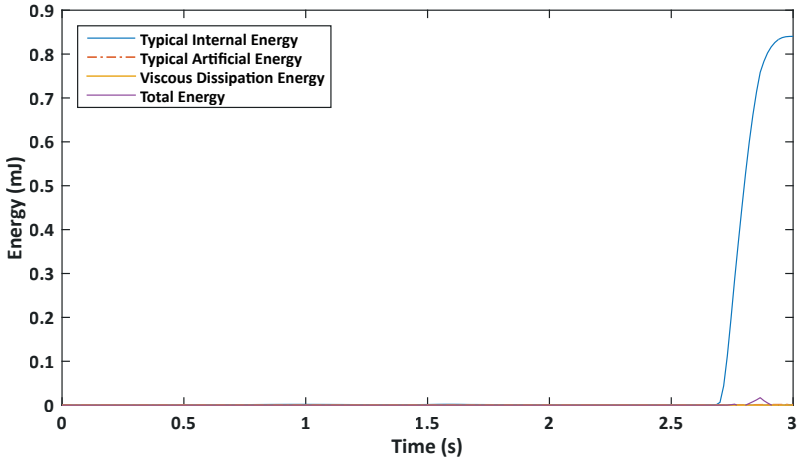

Figure 5.5: Energy variation of the finite element simulation for membrane with two creases

5.3.2 Comparison with experimental results

Figure 5.6 shows the snapshots taken during the simulation for the membrane specimen with two creases, compared with the shape of the specimen observed during physical experiments. It is evident that the membrane panel with pinned boundary condition does not undergo panel bending as in the experiment, which could be attributed to the inaccuracies in the experiment in replicating a perfect pinned boundary via the use of low stiffness adhesive. The crease at the loaded (top) end of the specimen indicate a similar opening behaviour at the start of the simulation. However, the simulation indicates negligible effect of crease stiffness during full deployment of the specimen, which differs from the behaviour observed in the physical experiments. This requires further investigation.

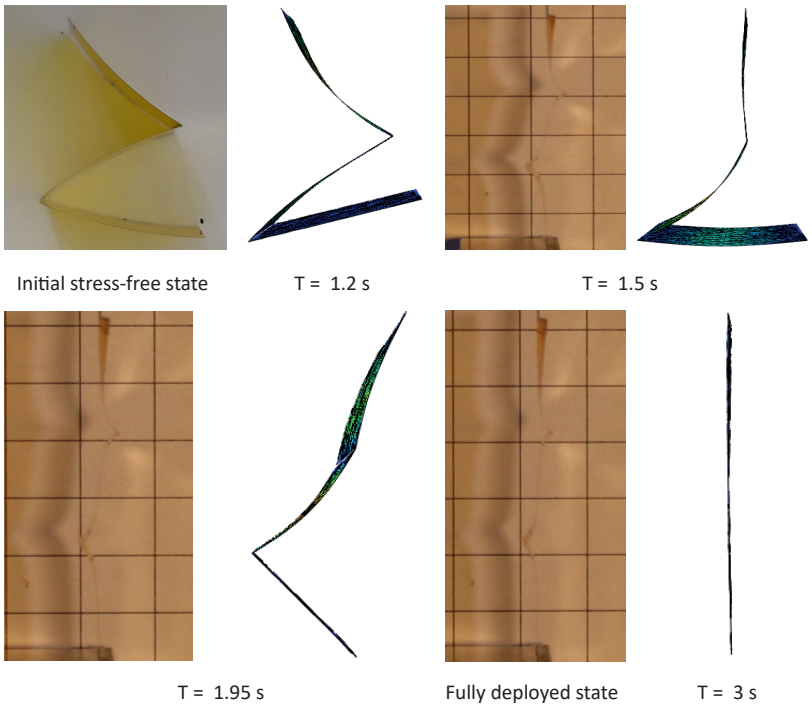

Figure 5.6: Snapshots taken during deployment simulation at different ratios of deployment compared with the shape of membrane observed during the experiment

Chapter 6

Quasi-static Deployment Simulation of a Creased Unit

In this chapter, an attempt is made to simulate the deployment behaviour of a simple creased unit consisting of an intersection of creases, by incorporating the crease-line mechanics presented in Chapter 4. The sensitivity of the simulation results is investigated based on the parameters applicable to the Abaqus/Explicit solver, and the simulated response is compared with the results of the physical experiments carried out via the improved experimental setup.

6.1 Crease pattern

In selecting a crease pattern, the main criteria to be satisfied were the presence of a single vertex with intersecting creases, and single degree of freedom for deployment. The traditional "Waterbomb" base with 6 creases was chosen for this purpose as a result, consisting of 4 mountain creases and 2 valley creases as illustrated in Figure 6.1.

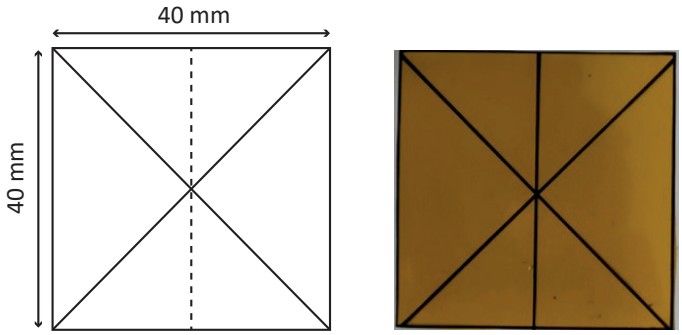

Figure 6.1: Crease pattern

The size of the specimen (40 mm × 40 mm) was chosen so that the lengths of the creases are in the same order as that of the parallel-creased membrane specimens used in the experimental study for characterisation of crease stiffness.

6.2 Details of the experimental study

The simple creased unit was prepared by the same method as what was followed for the parallel-creased membranes. On obtaining the pre-creases as shown in Figure 6.2 (a), the overall specimen in its folded configuration was subjected to a creasing pressure by a load of 7.05 kg for a duration of 30 minutes. The specimen was allowed to attain its initial stress-free state for 1 hour, following which it was placed in the experimental setup imposing the boundary conditions (see Figure 6.2 (b) and (c)).

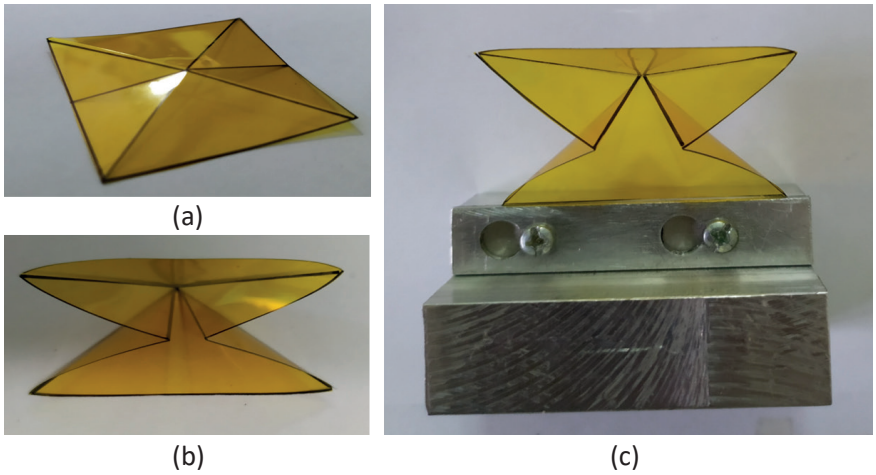

Figure 6.2: Simple creased unit (experimental study)
(a) Pre-creases (b) On achieving initial stress-free state (c) Imposing pinned boundary condition at one edge

Care was taken during the experiment to minimise the effect of air drag by ensuring quasi-static nature of deployment using lower steps of displacement, at a rate of 1 mm/step. However, beyond the ratio of deployment (D/D_f) of 0.93, the point of application of displacement was identified to undergo axial extension, limiting the maximum opening of the specimen to 37 mm at an angle of 140°-145°, as shown in Figure 6.3.

This behaviour could be attributed to the direction of application of deployment force to the specimen. The applied direction of loading (vertical) leads to the opening of the mountain creases of the specimen, but the overall deployment is limited by the lack of opening of the valley creases. It is observed that the deployment of the specimen is dominated by crease actuation of mountain creases up until this limit (with no panel bending), following which

the deployment of the specimen becomes dominated by panel bending about the point of displacement application (see Figure 6.3).

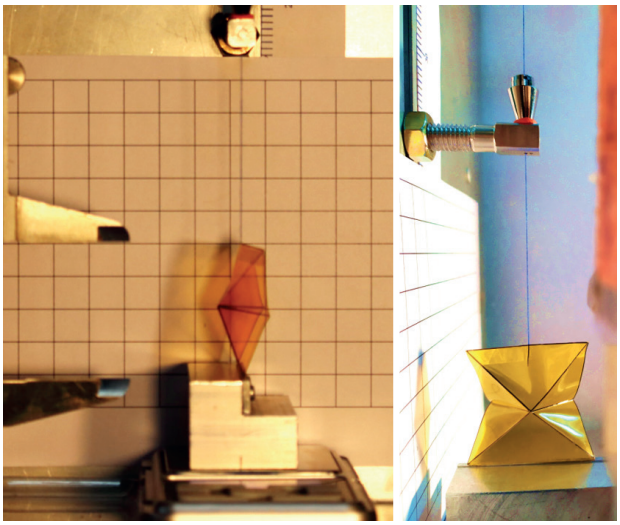

Figure 6.3: Deployment of simple creased unit (experimental study)

6.3 Finite element model of the creased unit

The numerical model for the creased unit was set up in Abaqus/Explicit finite element package. The geometry of the membrane panels separated by creases were created and meshed in Abaqus/Explicit itself (see Figure 6.4 (a)). Linear three-node shell elements with reduced integration−S3R were used to model the membrane panels, considering its suitability for simulations of thin membrane structures, and crease-lines were represented by two-node 3D connector elements, CONN3D2 as elaborated under Section 5.2. The finite element model of the creased unit consisted of 3732 shell elements and 2570 nodes with the minimum size of finite element being 1 mm.

The self-opening action was assumed to be a result of the same crease stiffness as the subsequent deployment on application of an external displacement. Hence, the simulation sequence differed from the experiment, starting from the fully creased state (neutral angle assumed as zero) instead of the neutral angle state. The reaction force and displacement at node A was recorded throughout the simulation for the purpose of comparison with the physical experiments.

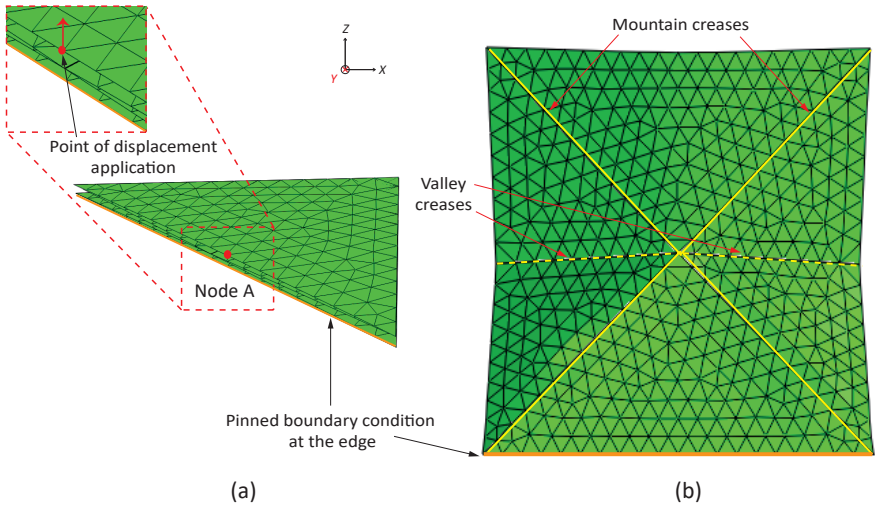

Figure 6.4: Finite element geometry of simple creased unit
(a) Fully folded state (b) Deployed state

Material properties of Kapton were defined as presented in Table 5.1, and the contact behaviour between the membrane panels was defined by using the *General Contact* feature for the entire membrane, by specifying *All* with self*. The significance of this option in Abaqus/Explicit over surface-to-surface contact feature is that it automatically identifies potential contact surfaces, based on the arrangement of the specific model [20]. In terms of the contact properties, "*Hard*" contact property which assumes no friction and no thermal interactions between the surfaces was used.

Since both the mountain and valley creases were observed to be contributing to the deployment of the creased unit, the rotational spring stiffness estimated in Chapter 4 was assigned to both the types of creases, uniformly distributed along the respective lengths.

6.4 Results and Discussion

6.4.1 Sensitivity of the simulation for the creased unit

Following the same methodology as in the case of membrane with two creases, a time scale of 4 s was chosen for the finite element model of the creased unit described in Section 6.3. Figure 6.5 ilustrates the kinetic energy profile of the simulation which was maintained within the limits of 1−5% of internal energy throughout the simulation. Similarly, a smooth step amplitude was defined such

that the dynamic effects imposed by the application of displacement are phased out.

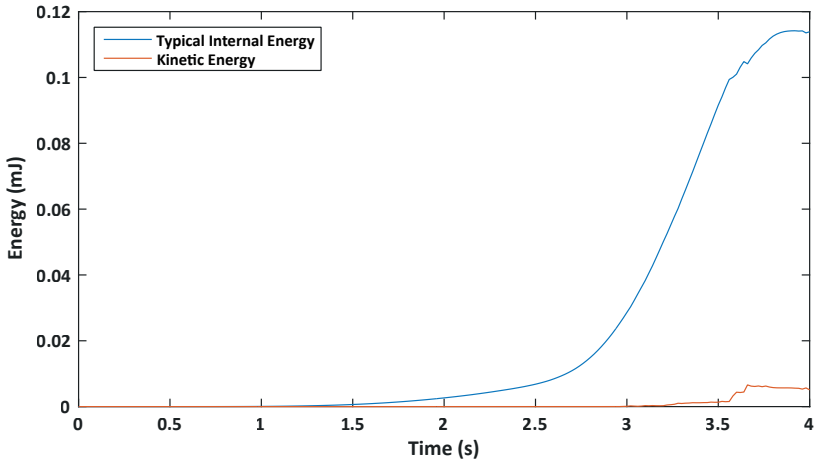

Figure 6.5: Comparison of kinetic energy profile with the internal energy profile of the finite element simulation for creased unit

On investigating the energy balance of the simulation further, the variation illustrated in Figure 6.6 was observed. It can be seen that the total energy for this simulation is close to zero throughout the simulation, indicating the absence of numerical instabilities affecing the results thus obtained. As recommended, the artificial energy lies in the range of $1-2\%$ of internal energy for the overall simulation, with negligible viscous dissipation energy due to the default contact damping force.

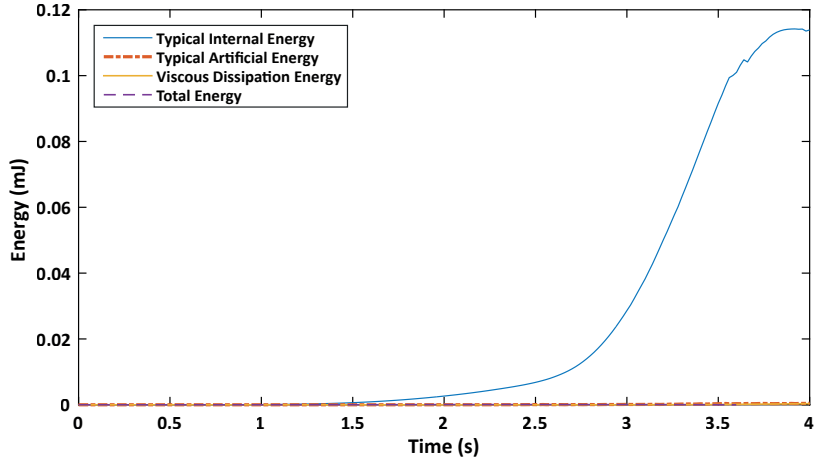

Figure 6.6: Energy variation of the finite element simulation for creased unit

6.4.2 Comparison with physical experiments

The comparison between the results obtained from the finite element simulation with the behaviour observed in the experiment was carried out by use of the displacement achieved by the specimen at each load step, over the full time scale.

Simulations were carried out considering both the cases of gravitational pressure and without gravitational pressure applied with the same smooth amplitude as the application of displacement, under the load step of the analysis. Figure 6.7 depicts the deployment force recorded at node A plotted against the ratio of deployment, D/D_f. Here, D was defined as the vertical distance between the pinned and loaded edges.

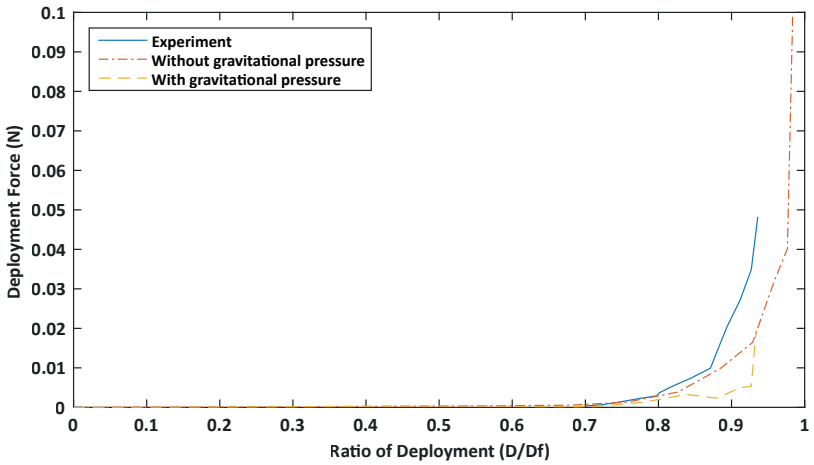

Figure 6.7: Energy variation of the finite element simulation for creased unit

It can be seen that up to 80% deployment, both the simulations with and without the effect of gravitational pressure align well with the experimental results. Beyond this point, the model with the effect of gravitational pressure fails to represent the results obtained by the experiment, while the model without the gravitational effect indicate lower deployment forces for the same ratio of deployment as the experiment. In all three plots, an increase in deployment force is observed for slight changes in ratio of deployment at the end of the simulation (this is more pronounced in the model without the effect of gravity), which indicates that the specimen has undergone axial tension at the point of load application. However, the model incorporating the effect of

gravity predicts the maximum ratio of deployment correctly, at 0.93 as observed in the experiments.

Figure 6.8 indicates the snapshots taken during deployment simulation at different ratios of deployment for the model including the gravitational pressure, compared with the shape of the structure observed during the experiment. The experiment was concluded at the point where axial extension of the membrane commenced, as evident from the difference in the shape observed at the end of the simulation process.

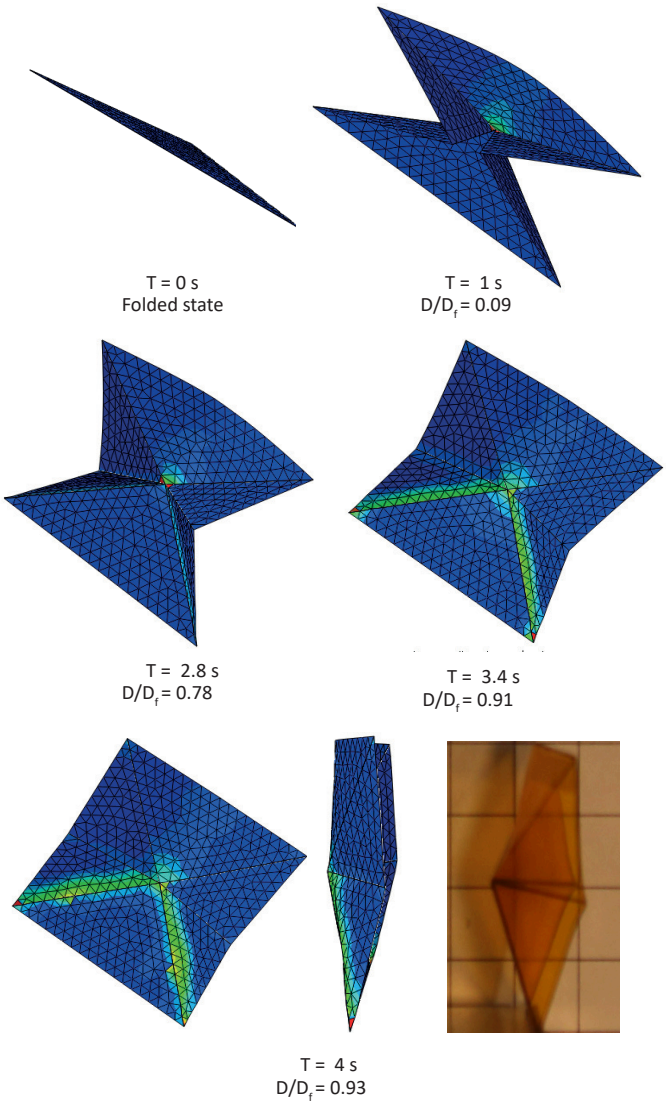

Figure 6.8: Snapshots taken during deployment simulation at different ratios of deployment compared with the final shape of structure observed during experiments

Chapter 7

Conclusions and Future Work

7.1 Conclusions

Creased membrane structures display unique behaviours due to the localised plastic deformations developed in thin membranes during creasing. Previous studies have identified that the hinge response at a crease could be best represented by a rotational spring, whose nature of stiffness should be determined via physical experiments. Following the initial stress-free state of the creased membrane achieved on removal of creasing pressure, additional loads exerted on the membrane for opening or closing would lead to a resistive moment at the crease, as a result of crease actuation and panel bending on either side. This resistive moment, along with the opening angle at each step of loading has been utilised in this study to arrive at the crease stiffness k, which is found to be linear for parallel-creased membranes. In assessing this response, the significance of the effect of self-weight of the membrane was analysed, which was neglected by earlier researchers. Equations have been formulated for the moment−rotation response at one, two and three parallel creases incorporating the effect of self-weight accordingly. The time dependence of the moment−rotation response was analysed as well, by measuring the time taken for attaining static equilibrium on being loaded.

On identifying the limitations in the experimental setup developed by previous researchers which contributed to inaccuracies in the measurements taken to assess the moment−rotation response of creased membranes, an improved experimental setup was designed and developed. The produced setup offers capabilities in facilitating controlled displacement for creased membranes of a wide range of dimensions, along with precise force measurement devoid of disturbances due to vibrations on loading. It also encompasses the means of ensuring proper alignment of the membrane, which is considered essential owing

to the accuracy of opening angle and distance measurements being dependent on it.

Crease stiffness was determined for single-creased 25 μm thick Kapton 100HN membranes utilising the improved setup, which was incorporated to finite element simulations for the purpose of predicting the deployment behaviour of membrane structures with multiple creases. Here, the crease-line is represented by connector elements assigned with a specific rotational elasticity (determined by the physical experiments), and the response of a membrane specimen with two creases on application of an external displacement is simulated using commercial finite element package Abaqus/Explicit. While the simulation was able to capture some features of the response observed in the actual structure, the crease stiffness was observed to have negligible effect on the deployment which contradicts the experimental observations. Hence, it requires further refinement in order for accurate results on deployment characteristics to be obtained.

For the purpose of investigating the applicability of the determined crease stiffness in predicting the deployment behaviour of a membrane structure consisting of intersecting creases, a quasi-static simulation was carried out for a simple creased unit based on traditional "Waterbomb" base. The simulation which was developed in Abaqus/Explicit environment was able to capture the deployment response observed in the physical experiments, in terms of maximum deployment ratio and shape once the effect of gravity was incorporated to the simulation.

7.2 Recommendations for Future Work

The following are some suggested future research directives.

1. Quantifying the stiffness of asymmetric creases and interacting creases at a vertex of a membrane structure.

2. Carrying out microscopic experimental investigations utilising Digital Image Correlation techniques (DIC) (determining strain contours of the membrane) for accurately capturing the effect of crease stiffness on its deployment behaviour.

References

[1] S. D. Guest, "Deployable Structures : Concepts and Analysis," Ph.D. dissertation, University of Cambridge, 1994.

[2] V. Brunck, F. Lechenault, A. Reid, and M. Adda-Bedia, "Elastic theory of origami-based metamaterials," *Phys. Rev. E*, vol. 93, no. 3, p. 33005, Mar 2016.

[3] R. J. Lang, S. Magleby, and L. Howell, "Single-degree-of-freedom rigidly foldable cut origami flashers," *Journal of Mechanisms and Robotics*, vol. 8, 11 2015.

[4] E. Filipov, K. Liu, T. Tachi, M. Schenk, and G. Paulino, "Bar and hinge models for scalable analysis of origami," *International Journal of Solids and Structures*, vol. 124, pp. 26 – 45, 2017.

[5] M. Schenk and S. D. Guest, "Geometry of miura-folded metamaterials," *Proceedings of the National Academy of Sciences*, vol. 110, no. 9, pp. 3276–3281, 2013.

[6] D. Lichodziejewski, B. Derbès, K. Slade, and T. Mann, "Vacuum deployment and testing of a 4-quadrant scalable inflatable rigidizable solar sail system," in *46th AIAA/ASME/ASCE/AHS/ASC Structures, Structural Dynamics, and Materials Conference*, Austin, Texas, 2005.

[7] U. Geppert, B. Biering, F. Lura, J. Block, M. Straubel, and R. Reinhard, "The 3-step DLR-ESA Gossamer road to solar sailing," *Advances in Space Research*, vol. 48, no. 11, pp. 1695–1701, 2011.

[8] P. Seefeldt, P. Spietz, T. Spröwitz, J. Grundmann, M. Hillebrandt, C. Fiona Hobbie, M. Ruffer, M. Straubel, N. Toth, and M. Zander,

"Gossamer-1: Mission concept and technology for a controlled deployment of gossamer spacecraft," *Advances in Space Research*, vol. 59, 12 2016.

[9] P. Seefeldt, "A stowing and deployment strategy for large membrane space systems on the example of gossamer-1," *Advances in Space Research*, vol. 60, 06 2017.

[10] X. Zhang and C. Zhou, "Dynamic analysis of spinning solar sails at deployment process," *Chinese Journal of Aeronautics*, vol. 30, no. 5, pp. 1719 – 1728, 2017. [Online]. Available: http://www.sciencedirect.com/science/article/pii/S1000936117301838

[11] C. Katan, "Nasa's next solar sail: lessons learned from nanosail-d2," in *26th Annual AIAA/USU Conference on Small Satellites: Enhancing Global Awareness through Small Satellites*, 2012.

[12] NASA, "NanoSail-D." [Online]. Available: https://www.nasa.gov/mission{_}pages/smallsats/nanosaild.html

[13] L. Johnson, M. Whorton, A. Heaton, R. Pinson, G. Laue, and C. Adams, "NanoSail-D: A solar sail demonstration mission," *Acta Astronautica*, vol. 68, no. 5-6, pp. 571–575, 2011.

[14] "FeatherSail – Design, Development and Future D.C. Alhorn and J. M. Scheierl Marshall Space Flight Center (MSFC) Huntsville, Alabama," 2018.

[15] NASA, "NanoSail-D," NASA, Tech. Rep., 2010. [Online]. Available: www.nasa.gov

[16] The Planetary Society, "Radial Velocity — The Planetary Society," 2019. [Online]. Available: http://www.planetary.org/explore/projects/lightsail-solar-sailing/lightsail-faqs.htmlhttp://www.planetary.org/explore/space-topics/exoplanets/radial-velocity.html

[17] B. B. Betts, B. Nye, J. Vaughn, E. Greeson, R. Chute, D. A. Spencer, R. W. Ridenoure, R. Munakata, S. D. Wong, A. Diaz, D. A. Stetson, J. D. Foley, J. M. Bellardo, and B. A. Plante, "LightSail 1 Mission Results and Public Outreach Strategies," in *Fourth International Symposium on Solar Sailing*, Kyoto, Japan, 2017.

[18] B. B. Betts, D. A. Spencer, B. Nye, R. Munakata, J. M. Bellardo, S. D. Wong, A. Diaz, R. W. Ridenoure, B. A. Plante, J. D. Foley, and J. Vaughn, "LightSail 2 : Controlled Solar Sailing Using a CubeSat," in *Fourth International Symposium on Solar Sailing*, Kyoto, Japan, 2017.

[19] D. Chambers, "Active Response Gravity Offload System," p. 1, 2013. [Online]. Available: https://www.nasa.gov/centers/johnson/partnerships/eddc/is/active-response-gravity-offload-systemhttps://www.nasa.gov/centers/johnson/engineering/integrated{_}environments/active{_}response{_}gravity/index.html

[20] S. Mierunalan, "Prediction of Mechanical Properties of Creases in Thin Folded Membranes," Master's thesis, University of Moratuwa, 2018.

[21] J. M. Gattas, W. Wu, and Z. You, "Miura-base rigid origami: Parameterizations of first-level derivative and piecewise geometries," *Journal of Mechanical Design*, vol. 135, p. 111011, 10 2013.

[22] X. Zhou, S. Zang, and Z. You, "Origami mechanical metamaterials based on the miura-derivative fold patterns," *Proceedings of the Royal Society of London A: Mathematical, Physical and Engineering Sciences*, vol. 472, no. 2191, 2016.

[23] A. Papa and S. Pellegrino, "Systematically Creased Thin-Film Membrane Structures," *J. Spacecr. Rockets*, vol. 45, no. 1, pp. 10–18, 2008.

[24] R. Funase, M. Sugita, O. Mori, Y. Tsuda, and J. Kawaguchi, "Modeling of Spinning Solar Sail By Multi Particle Model and Its Application To Attitude Control System," in *Proceedings of the ASME 2009 International Design Engineering Technical Conferences & Computers and Information in Engineering Conference*, San Diego, California, 2009.

[25] F. Wang, H. Gong, X. Chen, and C. Q. Chen, "Folding to curved surfaces: A generalized design method and mechanics of origami-based cylindrical structures," *Scientific Reports*, vol. 6, p. 33312, 09 2016.

[26] B. Y. Dharmadasa, H. M. Y. C. Mallikarachchi, and F. Lopez Jimenez, "Characterizing the Mechanics of Fold-lines in Thin Kapton Membranes," in *2018 AIAA Spacecraft Structures Conference*. Kissimmee, Florida: American Institute of Aeronautics and Astronautics, 2018.

[27] Y. Satou and H. Furuya, "Effects of elasto-plastic behavior of crease on deployed shape of space membrane," 01 2018.

[28] F. Lechenault and M. Adda-Bedia, "Generic Bistability in Creased Conical Surfaces," *Phys. Rev. Lett.*, vol. 115, no. 23, pp. 1–5, 2015.

[29] M. Schenk, "Folded Shell Structures," Ph.D. dissertation, University of Cambridge, 2011.

[30] H. Sakamoto, M. C. Natori, S. Kadonishi, Y. Satou, Y. Shirasawa, N. Okuizumi, O. Mori, H. Furuya, and M. Okuma, "Folding patterns of planar gossamer space structures consisting of membranes and booms," *Acta Astronaut.*, vol. 94, no. 1, pp. 34–41, 2014.

[31] J. Cai, Z. Ren, Y. Ding, X. Deng, Y. Xu, and J. Feng, "Deployment simulation of foldable origami membrane structures," *Aerosp. Sci. Technol.*, vol. 67, no. April, pp. 343–353, 2017.

[32] B. Y. Dharmadasa, "Simulation of Fold-Line Stiffness in Deployable Membranes," Master's thesis, University of Moratuwa, 2017.

[33] Dupont, "DEC Kapton summary of properties," 2015. [Online]. Available: http://www.dupont.com/products-and-services/membranes-films/polyimide-films/brands/kapton-polyimide-film/products/kapton-fn.html

[34] Abaqus, "Analysis User's Guide," Dassault Systemes Simulia Corp., Providence, Rhode Island, 2014.

[35] K. Miura, "Method of packaging and deployment of large membranes in space," The Institute of Space and Astronautical Science, Tech. Rep., 1985.

[36] S. J. Callens and A. A. Zadpoor, "From flat sheets to curved geometries: Origami and kirigami approaches," *Materials Today*, vol. 21, no. 3, pp. 241 – 264, 2018. [Online]. Available: http://www.sciencedirect.com/science/article/pii/S1369702117306399

[37] Y. Chen, H. Feng, J. Ma, R. Peng, and Z. You, "Symmetric waterbomb origami," *Proceedings of the Royal Society A: Mathematical, Physical and Engineering Sciences*, vol. 472, no. 2190, p. Article: 20150846, 2016.

[38] K. Kuribayashi, K. Tsuchiya, Z. You, D. Tomus, M. Umemoto, T. Ito, and M. Sasaki, "Self-deployable origami stent grafts as a biomedical application

of Ni-rich TiNi shape memory alloy foil," *Materials Science and Engineering: A*, vol. 419, no. 1-2, pp. 131–137, Mar 2006.

[39] R. D. Resch, "The topological design of sculptural and architectural systems," in *Proceedings of the June 4-8, 1973, national computer conference and exposition on - AFIPS '73*. New York, USA: ACM Press, 1973, p. 643.

[40] R. J. Lang, "Airbag Folding - Robert J. Lang Origami," 2015. [Online]. Available: https://langorigami.com/article/airbag-folding/

[41] Www.caltech.edu, "Knowing When to Fold 'Em," 2012. [Online]. Available: https://www.caltech.edu/about/news/knowing-when-fold-em-37540

[42] D. Main, "From Robots To Retinas: 9 Amazing Origami Applications," 2014. [Online]. Available: https://www.popsci.com/article/science/robots-retinas-9-amazing-origami-applications/http://www.popsci.com/article/science/robots-retinas-9-amazing-origami-applications

[43] E. Filipov, G. H. Paulino, and T. Tachi, "Origami tubes with reconfigurable polygonal cross-sections," *Proceedings of the Royal Society A: Mathematical, Physical and Engineering Science*, vol. 472, p. 20150607, 01 2016.

[44] E. T. Filipov, T. Tachi, and G. H. Paulino, "Origami tubes assembled into stiff, yet reconfigurable structures and metamaterials," vol. 112, no. 40, pp. 12 321–12 326, 2015.

[45] M. Walker and K. Seffen, "The flexural mechanics of creased thin strips," *International Journal of Solids and Structures*, vol. 167, pp. 192 – 201, 2019. [Online]. Available: http://www.sciencedirect.com/science/article/pii/S0020768319301313

[46] V. Brunck, F. Lechenault, A. Reid, and M. Adda-Bedia, "Elastic theory of origami-based metamaterials," *Phys. Rev. E*, vol. 93, no. 3, p. 33005, mar 2016.

[47] K. Liu and G. H. Paulino, "Nonlinear mechanics of non-rigid origami: an efficient computational approach," *Proc. R. Soc. A Math. Phys. Eng. Sci.*, vol. 473, no. 2206, p. 20170348, 2017.

[48] C. Pradier, J. Cavoret, D. Dureisseix, C. Jean-Mistral, and F. Ville, "An Experimental Study and Model Determination of the Mechanical Stiffness

of Paper Folds," *Journal of Mechanical Design*, vol. 138, no. 4, p. 041401, 2016.

[49] S. Mierunalan and H. M. Y. C. Mallikarachchi, "Prediction of creased geometry of thin folded membranes using finite element analysis," in *3rd International Moratuwa Engineering Research Conference, MERCon 2017*, Colombo, Sri Lanka, 2017, pp. 283–287.

[50] D. M. S. P. Dassanayake, S. Mierunalan, H. C. Weerasinghe, and H. M. Y. C. Mallikarachchi, "Fold-line mechanics of thin-folded membranes," in *Annual Sessions of Institution of Engineers, Sri Lanka*, The Institution of Engineers, Colombo, Sri Lanka, October 2018, pp. 203–210.

[51] F. Lechenault, B. Thiria, and M. Adda-Bedia, "Mechanical response of a creased sheet," *Phys. Rev. Lett.*, vol. 112, no. 24, pp. 1–5, 2014.

[52] S. marie Belcastro and T. C. Hull, "Modelling the folding of paper into three dimensions using affine transformations," *Linear Algebra and its Applications*, vol. 348, no. 1, pp. 273 – 282, 2002.

[53] T. Tachi, "Simulation of rigid origami," *Origami 4: Fourth International Meeting of Origami Science, Mathematics, and Education*, vol. 4, 08 2009.

[54] W. Wu and Z. You, "Modelling rigid origami with quaternions and dual quaternions," *Proceedings of the Royal Society of London A: Mathematical, Physical and Engineering Sciences*, vol. 466, no. 2119, pp. 2155–2174, 2010.

[55] R. MacNeal and W. Robbins, "Tensile properties of a tape with a transverse crease," Astro Research Corporation, Tech. Rep., 1966.

[56] D. Murphy, T. Trautt, M. McEachen, D. Messner, G. Laue, and P. Gierow, "Progress and plans for system demonstration of a scalable square solar sail," in *14th AAS/AIAA Space Flight Mechanics Conference*, AAS, San Diego, CA, 2004.

[57] M. A. Dias, L. H. Dudte, L. Mahadevan, and C. D. Santangelo, "Geometric mechanics of curved crease origami," *Phys. Rev. Lett.*, vol. 109, no. 11, pp. 1–5, 2012.

[58] J. P. Duncan and J. L. Duncan, "Folded Developables," *Proc. R. Soc. A Math. Phys. Eng. Sci.*, vol. 383, no. 1784, pp. 191–205, 1982.

[59] K. A. Seffen, "Spherical images and inextensible curved folding," *Phys. Rev. E*, vol. 97, no. 2, pp. 1–7, 2018.

[60] M. A. Dias and B. Audoly, "A non-linear rod model for folded elastic strips," *Journal of the Mechanics and Physics of Solids*, vol. 62, pp. 57 – 80, 2014, sixtieth anniversary issue in honor of Professor Rodney Hill. [Online]. Available: http://www.sciencedirect.com/science/article/pii/S0022509613001658

[61] A. Gough, N. M. A. Hossain, C. H. Jenkins, J. Blandino, and A. Hendricks, "Experimental and numerical study of creased membranes," in *46th AIAA/ASME/ASCE/AHS/ASC Structures, Structural Dynamics and Materials Conference*, Austin, TX, United States, 2005.

[62] N. Hossain, K. Woo, and C. Jenkins, "Nonlinear Material Response of Systematically Creased Membranes," in *47th AIAA/ASME/ASCE/AHS/ASC Structures, Structural Dynamics, and Materials Conference*, Newport, Rhode Island, 2006.

[63] B. Thiria and M. Adda-Bedia, "Relaxation mechanisms in the unfolding of thin sheets," *Phys. Rev. Lett.*, vol. 107 (2), p. 025506, Jul 2011.

[64] H. Yasuda, T. Yein, T. Tachi, K. Miura, and M. Taya, "Folding behaviour of tachi-miura polyhedron bellows," *Proceedings. Mathematical, physical, and engineering sciences / the Royal Society*, vol. 469, p. 20130351, 11 2013.

[65] H. Furuya, Y. Inoue, and T. Masuoka, "Deployment characteristics of rotationally skew fold membrane for spinning solar sail," in *46th AIAA/ASME/ASCE/AHS Structures, Structural Dynamics, and Materials Conference*, Austin, Texas, 04 2005.

[66] D. Sleight, Y. Michii, D. Lichodziejewski, B. Derbes, T. Mann, K. Slade, and J. Wang, "Finite Element Analysis and Test Correlation of a 10-Meter Inflation-Deployed Solar Sail," in *46th AIAA/ASME/ASCE/AHS/ASC Structures, Structural Dynamics and Materials Conference*, Austin, Texas, 2005.

[67] K. Woo, K. Nandukar, and C. H. Jenkins, "Effective modulus of creased thin membranes," *Journal of Spacecraft and Rockets*, vol. 45 (1), pp. 19–26, 2008.

[68] C. Wang, H. Tan, and X. D. He, "Wrinkle-crease interaction behavior simulation of a rectangular membrane under shearing," *Acta Mechanica Sinica*, vol. 27, pp. 550–558, 08 2011.

[69] M. Liyanage and H. M. Y. C. Mallikarachchi, "Origami based folding patterns for compact deployable structures," in *4th International Conference for Structural Engineering and Construction Management*, Kandy, Sri Lanka, December 2013.

[70] J. Zhao, Q. Tian, and H.-Y. Hu, "Deployment dynamics of a simplified spinning ikaros solar sail via absolute coordinate based method," *Acta Mechanica Sinica*, vol. 29, 02 2013.

[71] S. D. Guest and S. Pellegrino, "Inextensional wrapping of flat membranes," *Proceedings of International Seminar Structure Morphology*, 01 1992.

[72] A. C. Abbott, P. R. Buskohl, J. J. Joo, G. W. Reich, and R. A. Vaia, "Characterization of creases in polymers for adaptive origami structures," in *ASME 2014 Conference on Smart Materials, Adaptive Structures and Intelligent Systems, SMASIS 2014*, vol. 1. University of Dayton, Ohio, 2014. [Online]. Available: https://etd.ohiolink.edu/!etd.send{_}file?accession=dayton1406890919{&}disposition=inline

[73] A. C. Andrew, B. C. Philip, J. J. James, R. W. Gregory, and V. A. Richard, "Characterization of creases in polymers for adaptive origami structures," in *ASME 2014 Conference on Smart Materials, Adaptive Structures and Intelligent Systems SMASIS2014*, Newport, Rhode Island, 2014.

[74] Massachusetts Institute of Technology, "Selecting shell elements," 2017. [Online]. Available: https://abaqus-docs.mit.edu/2017/English/SIMACAEGSARefMap/simagsa-c-shlselecting.htm

[75] T. Belytschko, W. K. W. K. Liu, B. B. Moran, and K. I. Elkhodary, *Nonlinear finite elements for continua and structures*. John Wiley & Sons, 2014.

Appendix A

Moment−Angle Data

1. Single Crease Stiffness (Initial Experimental Setup)

Specimen 1

$\boldsymbol{\theta_1}$ (deg)	$\boldsymbol{x_1}$ *(cm)*	$\boldsymbol{M_1}$ $\times 10^{-3}$ *(Nm/m)*
88	0.83	0.52
92	0.74	0.58
93	0.67	0.64
94	0.60	0.66
97	0.54	0.68
100	0.50	0.71
101	0.47	0.74
102	0.45	0.78
104	0.43	0.79
106	0.39	0.80
109	0.38	0.81
110	0.37	0.82
112	0.36	0.83
113	0.35	0.84
114	0.34	0.85
114	0.33	0.87

Specimen 2

$\boldsymbol{\theta_1}$ (deg)	$\boldsymbol{x_1}$ *(cm)*	$\boldsymbol{M_1}$ $\times 10^{-3}$ *(Nm/m)*
68	0.79	0.45
71	0.73	0.51
72	0.65	0.57
74	0.58	0.62
78	0.52	0.65
80	0.49	0.69
81	0.45	0.72
81	0.44	0.75
83	0.42	0.77
85	0.37	0.78
88	0.36	0.80
91	0.35	0.81
92	0.33	0.82
93	0.32	0.83
95	0.31	0.84
96	0.30	0.85

Specimen 3

$\boldsymbol{\theta_1}$ (deg)	$\boldsymbol{x_1}$ *(cm)*	$\boldsymbol{M_1}$ $\times 10^{-3}$ *(Nm/m)*
75	0.81	0.50
78	0.76	0.56
79	0.68	0.63
81	0.61	0.66
84	0.56	0.70
89	0.52	0.73
90	0.48	0.76
91	0.46	0.80
94	0.44	0.82
96	0.39	0.84
98	0.37	0.85
101	0.36	0.87
103	0.34	0.89
104	0.33	0.90
105	0.32	0.91
106	0.31	0.92

2. Single Crease Stiffness (Improved Experimental Setup)

Specimen 1

$\boldsymbol{\theta_1}$ (deg)	$\boldsymbol{x_1}$ *(cm)*	$\boldsymbol{M_1}$ $\times 10^{-3}$ *(Nm/m)*
91	1.06	0.01
92	0.94	0.02
106	0.78	0.05
107	0.67	0.17
118	0.53	0.37
125	0.42	0.65
134	0.29	0.78
147	0.16	0.97
149	0.10	1.33

Specimen 2

$\boldsymbol{\theta_1}$ (deg)	$\boldsymbol{x_1}$ *(cm)*	$\boldsymbol{M_1}$ $\times 10^{-3}$ *(Nm/m)*
74	2.09	0.01
78	2.04	0.02
79	1.99	0.03
80	1.94	0.05
82	1.88	0.07
83	1.81	0.11
84	1.77	0.13
87	1.65	0.15
90	1.55	0.18
92	1.53	0.21
93	1.45	0.23
95	1.29	0.33
96	1.19	0.37
98	1.06	0.43
99	0.93	0.60
103	0.78	0.70
104	0.70	0.80
134	0.29	0.89
147	0.16	1.19
149	0.10	1.53

Specimen 3

$\boldsymbol{\theta_1}$ (deg)	$\boldsymbol{x_1}$ *(cm)*	$\boldsymbol{M_1}$ $\times 10^{-3}$ *(Nm/m)*
119	1.06	0.01
120	0.94	0.02
122	1.06	0.05
125	0.94	0.18
128	0.78	0.25
136	0.67	0.54
161	0.53	1.02
164	0.42	1.10

3. Stiffness of Membrane with Two Creases (Initial Experimental Setup)

Specimen 1 (Loading)

$\boldsymbol{\theta_1}$ (deg)	$\boldsymbol{\theta_2}$ (deg)	$\boldsymbol{x_1}$ *(cm)*	$\boldsymbol{x_2}$ *(cm)*	$\boldsymbol{M_1}$ $\times 10^{-3}$ *(Nm/m)*	$\boldsymbol{M_2}$ $\times 10^{-3}$ *(Nm/m)*
62	67	1.08	0.87	0.67	0.66
67	75	1.03	0.81	0.80	0.75
77	77	0.96	0.75	0.90	0.81
80	79	0.91	0.69	0.99	0.85
82	82	0.86	0.66	1.08	0.92
84	85	0.83	0.61	1.18	0.95
88	90	0.78	0.60	1.22	1.02
89	91	0.76	0.56	1.31	1.04
93	92	0.74	0.51	1.39	1.02
93	94	0.71	0.50	1.45	1.09
93	94	0.68	0.48	1.50	1.13
94	94	0.66	0.48	1.55	1.20
95	95	0.65	0.47	1.63	1.24
96	96	0.62	0.41	1.67	1.17
96	97	0.61	0.41	1.72	1.21
97	97	0.58	0.39	1.75	1.23
98	98	0.58	0.38	1.83	1.26
99	99	0.57	0.37	1.88	1.28
99	100	0.56	0.35	1.92	1.28
101	101	0.53	0.35	1.93	1.29
103	103	0.50	0.33	1.93	1.30
104	104	0.49	0.33	1.95	1.32
106	104	0.49	0.31	2.02	1.33
106	104	0.49	0.30	2.06	1.28
107	105	0.48	0.29	2.04	1.25
108	106	0.47	0.28	2.06	1.23
109	107	0.47	0.27	2.08	1.25

Specimen 1 (Unloading)

$\boldsymbol{\theta_1}$ (deg)	$\boldsymbol{\theta_2}$ (deg)	$\boldsymbol{x_1}$ *(cm)*	$\boldsymbol{x_2}$ *(cm)*	$\boldsymbol{M_1}$ $\times 10^{-3}$ *(Nm/m)*	$\boldsymbol{M_2}$ $\times 10^{-3}$ *(Nm/m)*
71	71	0.95	0.63	0.59	0.48
72	72	0.91	0.57	0.71	0.53
74	74	0.86	0.53	0.81	0.57
77	77	0.79	0.52	0.87	0.64
77	78	0.75	0.50	0.94	0.70
79	78	0.72	0.47	1.02	0.72
83	81	0.68	0.44	1.08	0.75
84	82	0.66	0.42	1.14	0.79
86	86	0.64	0.39	1.21	0.78
87	88	0.64	0.38	1.31	0.83
89	90	0.62	0.37	1.37	0.86
91	91	0.62	0.37	1.45	0.92
92	92	0.59	0.34	1.50	0.91
93	94	0.56	0.32	1.51	0.91
94	95	0.55	0.32	1.55	0.96
95	97	0.54	0.31	1.63	0.98
96	98	0.54	0.31	1.69	1.03
97	99	0.53	0.31	1.76	1.05
99	99	0.53	0.31	1.84	1.07
101	100	0.53	0.31	1.94	1.18
103	101	0.52	0.31	1.96	1.20
103	103	0.51	0.30	2.02	1.24
105	104	0.50	0.30	2.05	1.26
106	105	0.50	0.30	2.08	1.28
107	106	0.48	0.29	2.04	1.26
109	107	0.47	0.28	2.04	1.24
109	108	0.47	0.28	2.08	1.26

Specimen 2 (Loading)

$\boldsymbol{\theta_1}$ (deg)	$\boldsymbol{\theta_2}$ (deg)	$\boldsymbol{x_1}$ *(cm)*	$\boldsymbol{x_2}$ *(cm)*	$\boldsymbol{M_1}$ $\times 10^{-3}$ *(Nm/m)*	$\boldsymbol{M_2}$ $\times 10^{-3}$*(Nm/m)*
60	48	0.98	1.15	0.61	0.87
61	50	0.98	1.14	0.77	1.06
63	54	0.94	1.06	0.89	1.14
68	59	0.90	0.97	0.99	1.20
70	64	0.89	0.91	1.10	1.27
74	69	0.79	0.84	1.11	1.31
76	71	0.76	0.77	1.20	1.32
79	72	0.74	0.75	1.28	1.40
81	75	0.72	0.73	1.35	1.49
84	79	0.68	0.69	1.38	1.52
85	81	0.65	0.67	1.42	1.56
88	83	0.62	0.65	1.46	1.63
91	85	0.61	0.65	1.54	1.72
95	85	0.58	0.62	1.56	1.73
96	87	0.58	0.58	1.65	1.74
97	88	0.57	0.56	1.69	1.81
99	89	0.54	0.55	1.73	1.78
100	91	0.53	0.53	1.74	1.73
102	93	0.52	0.51	1.77	1.77
104	94	0.51	0.50	1.78	1.80
106	96	0.50	0.49	1.78	1.80
107	96	0.50	0.48	1.81	1.81

Specimen 2 (Unloading)

$\boldsymbol{\theta_1}$ (deg)	$\boldsymbol{\theta_2}$ (deg)	$\boldsymbol{x_1}$ *(cm)*	$\boldsymbol{x_2}$ *(cm)*	$\boldsymbol{M_1}$ $\times 10^{-3}$ *(Nm/m)*	$\boldsymbol{M_2}$ $\times 10^{-3}$*(Nm/m)*
70	50	0.93	1.09	0.58	0.83
72	51	0.87	1.04	0.68	0.96
73	55	0.85	0.97	0.80	1.04
75	57	0.83	0.89	0.91	1.10
78	60	0.81	0.86	1.02	1.19
79	61	0.76	0.83	1.07	1.29
80	63	0.73	0.78	1.15	1.33
83	66	0.72	0.73	1.25	1.36
84	68	0.71	0.71	1.33	1.44
85	70	0.69	0.70	1.41	1.52
87	71	0.66	0.66	1.45	1.54
89	74	0.63	0.64	1.50	1.59
90	75	0.61	0.62	1.56	1.65
91	78	0.60	0.61	1.59	1.75
93	80	0.59	0.60	1.68	1.80
94	83	0.58	0.58	1.73	1.82
95	85	0.55	0.55	1.74	1.82
100	88	0.54	0.54	1.77	1.85
102	90	0.53	0.51	1.78	1.80
104	92	0.52	0.50	1.79	1.80
105	94	0.51	0.49	1.77	1.81
106	96	0.50	0.49	1.80	1.82

4. Stiffness of Membrane with Two Creases (Initial Experimental Setup - Different Orientations)

Orientation 1 (Loading)

$\boldsymbol{\theta_1}$ (deg)	$\boldsymbol{\theta_2}$ (deg)	$\boldsymbol{x_1}$ *(cm)*	$\boldsymbol{x_2}$ *(cm)*	$\boldsymbol{M_1}$ $\times 10^{-3}$ *(Nm/m)*	$\boldsymbol{M_2}$ $\times 10^{-3}$*(Nm/m)*
111	119	0.53	0.70	0.33	0.54
113	121	0.50	0.64	0.39	0.59
114	122	0.48	0.60	0.45	0.65
116	126	0.43	0.53	0.54	0.74
118	128	0.40	0.49	0.63	0.83
121	131	0.37	0.45	0.69	0.91
123	134	0.32	0.42	0.71	0.99
126	136	0.29	0.40	0.74	1.07
127	137	0.28	0.38	0.81	1.10
131	139	0.27	0.37	0.85	1.22
133	140	0.26	0.36	0.87	1.28
134	141	0.25	0.35	0.89	1.31
136	142	0.24	0.34	0.92	1.34
137	144	0.22	0.33	0.89	1.33
137	146	0.21	0.32	0.87	1.35

Orientation 1 (Unloading)

$\boldsymbol{\theta_1}$ (deg)	$\boldsymbol{\theta_2}$ (deg)	$\boldsymbol{x_1}$ *(cm)*	$\boldsymbol{x_2}$ *(cm)*	$\boldsymbol{M_1}$ $\times 10^{-3}$ *(Nm/m)*	$\boldsymbol{M_2}$ $\times 10^{-3}$*(Nm/m)*
110	119	0.52	0.70	0.32	0.53
113	121	0.49	0.64	0.39	0.59
114	123	0.45	0.61	0.42	0.66
116	125	0.42	0.52	0.53	0.73
118	127	0.38	0.47	0.60	0.80
120	129	0.36	0.44	0.69	0.90
123	132	0.32	0.43	0.71	1.00
125	134	0.30	0.40	0.76	1.07
127	135	0.28	0.38	0.80	1.13
128	136	0.27	0.38	0.86	1.25
130	138	0.27	0.37	0.93	1.33
132	140	0.24	0.36	0.91	1.40
134	143	0.23	0.35	0.91	1.42
136	144	0.22	0.34	0.89	1.42
137	146	0.22	0.33	0.88	1.37

Orientation 2 (Loading)

$\boldsymbol{\theta_1}$ (deg)	$\boldsymbol{\theta_2}$ (deg)	$\boldsymbol{x_1}$ *(cm)*	$\boldsymbol{x_2}$ *(cm)*	$\boldsymbol{M_1}$ $\times 10^{-3}$ *(Nm/m)*	$\boldsymbol{M_2}$ $\times 10^{-3}$*(Nm/m)*
110	120	0.57	0.63	0.36	0.48
114	123	0.54	0.58	0.42	0.53
115	124	0.51	0.55	0.48	0.59
119	129	0.45	0.48	0.57	0.67
122	132	0.43	0.43	0.67	0.72
124	134	0.39	0.42	0.74	0.85
126	137	0.37	0.38	0.82	0.90
128	138	0.35	0.36	0.87	0.96
130	140	0.34	0.35	0.95	1.03
131	142	0.31	0.32	0.99	1.06
132	143	0.29	0.30	1.00	1.09
133	144	0.28	0.29	1.06	1.15
133	145	0.27	0.27	1.07	1.10
134	146	0.27	0.27	1.08	1.12
135	146	0.27	0.27	1.10	1.12

Orientation 2 (Unloading)

$\boldsymbol{\theta_1}$ (deg)	$\boldsymbol{\theta_2}$ (deg)	$\boldsymbol{x_1}$ *(cm)*	$\boldsymbol{x_2}$ *(cm)*	$\boldsymbol{M_1}$ $\times 10^{-3}$ *(Nm/m)*	$\boldsymbol{M_2}$ $\times 10^{-3}$*(Nm/m)*
110	122	0.57	0.58	0.35	0.45
111	123	0.54	0.52	0.42	0.48
112	124	0.50	0.49	0.47	0.53
115	128	0.46	0.44	0.57	0.62
117	130	0.42	0.42	0.66	0.72
118	131	0.38	0.39	0.71	0.80
120	132	0.36	0.39	0.80	0.92
122	135	0.35	0.35	0.89	0.93
125	137	0.31	0.35	0.90	1.03
127	138	0.31	0.32	0.97	1.07
129	140	0.30	0.32	1.05	1.15
130	141	0.29	0.31	1.09	1.22
133	144	0.28	0.28	1.09	1.14
135	144	0.27	0.27	1.10	1.14
135	145	0.27	0.27	1.10	1.13

Orientation 3 (Loading)

$\boldsymbol{\theta_1}$ (deg)	$\boldsymbol{\theta_2}$ (deg)	$\boldsymbol{x_1}$ *(cm)*	$\boldsymbol{x_2}$ *(cm)*	$\boldsymbol{M_1}$ $\times 10^{-3}$ *(Nm/m)*	$\boldsymbol{M_2}$ $\times 10^{-3}$*(Nm/m)*
128	134	0.63	0.26	0.40	0.20
129	136	0.59	0.25	0.46	0.23
130	137	0.54	0.24	0.51	0.27
133	138	0.49	0.22	0.62	0.30
134	140	0.45	0.21	0.71	0.35
135	141	0.42	0.19	0.79	0.38
137	143	0.39	0.18	0.86	0.41
139	144	0.37	0.17	0.92	0.44
140	145	0.35	0.15	0.99	0.43
141	146	0.33	0.14	1.05	0.47
142	148	0.32	0.13	1.11	0.44
143	149	0.31	0.12	1.19	0.47
144	148	0.31	0.12	1.22	0.48
144	149	0.30	0.11	1.22	0.47
145	150	0.29	0.10	1.21	0.46

Orientation 3 (Unloading)

$\boldsymbol{\theta_1}$ (deg)	$\boldsymbol{\theta_2}$ (deg)	$\boldsymbol{x_1}$ *(cm)*	$\boldsymbol{x_2}$ *(cm)*	$\boldsymbol{M_1}$ $\times 10^{-3}$ *(Nm/m)*	$\boldsymbol{M_2}$ $\times 10^{-3}$*(Nm/m)*
123	132	0.68	0.27	0.43	0.20
124	134	0.65	0.22	0.51	0.21
125	135	0.58	0.25	0.54	0.27
128	136	0.52	0.21	0.65	0.30
130	137	0.46	0.20	0.72	0.35
132	139	0.42	0.19	0.80	0.39
133	141	0.39	0.18	0.87	0.43
135	142	0.37	0.17	0.92	0.46
137	143	0.35	0.15	0.99	0.45
138	144	0.34	0.14	1.06	0.47
139	145	0.33	0.14	1.10	0.49
140	146	0.32	0.13	1.17	0.49
142	148	0.31	0.12	1.20	0.49
143	149	0.30	0.12	1.21	0.49
144	150	0.30	0.11	1.22	0.48

Orientation 4 (Loading)

$\boldsymbol{\theta_1}$ (deg)	$\boldsymbol{\theta_2}$ (deg)	$\boldsymbol{x_1}$ *(cm)*	$\boldsymbol{x_2}$ *(cm)*	$\boldsymbol{M_1}$ $\times 10^{-3}$ *(Nm/m)*	$\boldsymbol{M_2}$ $\times 10^{-3}$*(Nm/m)*
131	132	0.52	0.45	0.33	0.34
132	133	0.47	0.45	0.37	0.41
133	134	0.43	0.44	0.40	0.48
136	136	0.36	0.43	0.45	0.60
138	138	0.31	0.41	0.49	0.70
140	139	0.27	0.39	0.51	0.79
142	141	0.26	0.38	0.57	0.88
143	142	0.23	0.35	0.58	0.92
144	144	0.22	0.34	0.62	1.01
145	145	0.20	0.33	0.62	1.10
146	146	0.18	0.33	0.63	1.19
147	146	0.18	0.32	0.68	1.28
148	147	0.18	0.31	0.70	1.28
149	148	0.17	0.31	0.69	1.29
150	149	0.16	0.30	0.69	1.25

Orientation 4 (Unloading)

$\boldsymbol{\theta_1}$ (deg)	$\boldsymbol{\theta_2}$ (deg)	$\boldsymbol{x_1}$ *(cm)*	$\boldsymbol{x_2}$ *(cm)*	$\boldsymbol{M_1}$ $\times 10^{-3}$ *(Nm/m)*	$\boldsymbol{M_2}$ $\times 10^{-3}$*(Nm/m)*
128	130	0.52	0.46	0.32	0.35
130	132	0.46	0.46	0.36	0.43
133	133	0.42	0.45	0.40	0.49
137	134	0.35	0.43	0.45	0.60
138	137	0.31	0.40	0.49	0.68
140	138	0.28	0.39	0.52	0.79
141	139	0.26	0.37	0.57	0.87
141	140	0.24	0.36	0.60	0.95
142	142	0.22	0.35	0.63	1.04
143	143	0.21	0.35	0.67	1.14
144	144	0.20	0.34	0.70	1.21
146	145	0.19	0.33	0.73	1.30
147	146	0.19	0.31	0.74	1.27
148	148	0.18	0.31	0.71	1.27
150	149	0.17	0.30	0.69	1.26

5. Stiffness of Membrane with Three Creases (Initial Experimental Setup)

Crease 1

Loading			**Unloading**		
$\boldsymbol{\theta_1}$ (deg)	$\boldsymbol{x_1}$ *(cm)*	$\boldsymbol{M_1}$ $\times 10^{-3}$ *(Nm/m)*	$\boldsymbol{\theta_1}$ (deg)	$\boldsymbol{x_1}$ *(cm)*	$\boldsymbol{M_1}$ $\times 10^{-3}$ *(Nm/m)*
107	0.73	0.47	108	0.77	0.48
108	0.71	0.56	110	0.73	0.57
109	0.67	0.63	114	0.71	0.66
111	0.62	0.78	117	0.65	0.82
113	0.57	0.90	120	0.59	0.92
117	0.52	0.98	122	0.54	1.01
121	0.49	1.08	125	0.50	1.10
124	0.47	1.18	127	0.47	1.17
127	0.43	1.22	129	0.44	1.25
129	0.40	1.24	131	0.43	1.35
131	0.39	1.34	132	0.42	1.44
134	0.38	1.44	134	0.39	1.45
135	0.37	1.49	136	0.37	1.49
137	0.35	1.54	137	0.35	1.51
138	0.34	1.61	139	0.34	1.54
139	0.33	1.68	140	0.34	1.60
141	0.32	1.74	141	0.33	1.71
142	0.32	1.77	141	0.32	1.77
143	0.31	1.74	142	0.31	1.75
143	0.30	1.71	143	0.30	1.71

Crease 2

Loading			**Unloading**		
$\boldsymbol{\theta_2}$ (deg)	$\boldsymbol{x_2}$ *(cm)*	$\boldsymbol{M_2}$ $\times 10^{-3}$ *(Nm/m)*	$\boldsymbol{\theta_2}$ (deg)	$\boldsymbol{x_2}$ *(cm)*	$\boldsymbol{M_2}$ $\times 10^{-3}$ *(Nm/m)*
96	0.69	0.52	96	0.71	0.58
99	0.64	0.59	101	0.63	0.63
100	0.63	0.68	103	0.62	0.70
102	0.56	0.78	108	0.57	0.77
105	0.53	0.90	110	0.51	0.94
107	0.49	0.98	113	0.48	0.98
109	0.46	1.09	115	0.45	1.04
111	0.42	1.13	118	0.41	1.11
112	0.41	1.23	119	0.40	1.14
114	0.41	1.33	121	0.40	1.17
115	0.40	1.44	122	0.39	1.23
117	0.39	1.54	124	0.38	1.31
118	0.35	1.48	125	0.34	1.44
119	0.34	1.53	127	0.33	1.53
121	0.33	1.61	129	0.32	1.62
123	0.30	1.54	129	0.31	1.57
124	0.29	1.59	131	0.28	1.57
125	0.28	1.60	132	0.27	1.59
127	0.28	1.60	133	0.27	1.59
127	0.27	1.57	134	0.26	1.58

Crease 3

Loading			**Unloading**		
$\boldsymbol{\theta_3}$ *(*deg*)*	$\boldsymbol{x_3}$ *(cm)*	$\boldsymbol{M_3}$ $\times 10^{-3}$ *(Nm/m)*	$\boldsymbol{\theta_3}$ *(*deg*)*	$\boldsymbol{x_3}$ *(cm)*	$\boldsymbol{M_3}$ $\times 10^{-3}$ *(Nm/m)*
110	0.86	0.72	113	0.85	0.71
112	0.84	0.83	114	0.81	0.80
113	0.81	0.93	115	0.79	0.91
115	0.76	1.12	118	0.72	1.06
118	0.72	1.29	120	0.66	1.18
121	0.67	1.41	122	0.63	1.31
124	0.65	1.56	124	0.59	1.44
126	0.62	1.68	126	0.58	1.57
128	0.60	1.84	131	0.55	1.68
130	0.55	1.79	132	0.53	1.76
133	0.53	1.93	133	0.51	1.90
134	0.52	2.07	135	0.50	1.99
136	0.49	2.08	136	0.48	2.08
137	0.48	2.21	137	0.47	2.16
139	0.47	2.32	139	0.46	2.26
141	0.46	2.43	140	0.45	2.33
142	0.44	2.40	141	0.44	2.43
143	0.43	2.45	141	0.43	2.41
143	0.42	2.40	142	0.42	2.43
143	0.41	2.41	143	0.41	2.41

Appendix B

Keywords of Abaqus Input Files

1. Predicting Deployment Behaviour of Membrane with Two Parallel Creases

```
**----------------------------------------
** CONSTRAINT DEFINITION
**----------------------------------------
* Constraint: tie
*Tie, name=tie, adjust=yes, no rotation,
type=NODE TO SURFACE
**----------------------------------------
** CONNECTOR PROPERTY DEFINITION
**----------------------------------------
Connector Behavior, name=Connect
*Connector Elasticity, component=4
0.022649,
* * *---------------------------------------- ** ELEMENT CONTROL
**----------------------------------------
*Section Controls, name=EC-1
1., 1., 1., 0.01, 1.
*Amplitude, name=Smooth, definition=SMOOTH STEP
0., 0., 3.1, 1.
**----------------------------------------
** MATERIAL PROPERTY DEFINITION
**----------------------------------------
*Material, name=Kapton-lin
*Density
```

```
1.42e-09,
*Elastic
2500., 0.34
**----------------------------------------
** INTERACTION PROPERTY
**----------------------------------------
*Surface Interaction, name=contactproperty
*Surface Behavior, pressure-overclosure=HARD
**----------------------------------------
** BOUNDARY CONDITIONS
**----------------------------------------
** Name: PinnedC Type: Symmetry/Axisymmetry/Encastre
*Boundary
Set-6, 1, 1
** Name: Disp Type: Displacement/Rotation
*Boundary
Set-7, 1, 1
**----------------------------------------
** INTERACTIONS
**----------------------------------------
** Interaction: Contact
*Contact, op=NEW
*Contact Inclusions, ALL* with self
*Contact Property Assignment,contactproperty
**----------------------------------------
** STEP: Load
**----------------------------------------
*Step, name=Load, nlgeom=YES
*Dynamic, Explicit
, 4.2
*Bulk Viscosity
0., 0.
**----------------------------------------
```

```
**----------------------------------------------------------------
** CONSTRAINT DEFINITION
**----------------------------------------------------------------
** Constraint: tie
*Tie, name=tie, adjust=yes, no rotation,
type=SURFACE TO SURFACE
**----------------------------------------------------------------
** CONNECTOR PROPERTY DEFINITION
**----------------------------------------------------------------
Connector Behavior, name=Connect1
*Connector Elasticity, component=4
0.035181,
**----------------------------------------------------------------
Connector Behavior, name=Connect2
*Connector Elasticity, component=4
0.024877,
**----------------------------------------------------------------
** ELEMENT CONTROL
**----------------------------------------------------------------
*Section Controls, name=EC-1
1., 1., 1., 0.01, 1.
*Amplitude, name=Smooth, definition=SMOOTH STEP
0., 0., 4.1, 1.
**----------------------------------------------------------------
** MATERIAL PROPERTY DEFINITION
**----------------------------------------------------------------
*Material, name=Kapton
*Density
1.42e-09,
*Elastic
2500., 0.34
**----------------------------------------------------------------
** INTERACTION PROPERTY
**----------------------------------------------------------------
*Surface Interaction, name=contactproperty
```

```
*Surface Behavior, pressure-overclosure=HARD
**----------------------------------------------------------------
** BOUNDARY CONDITIONS
**----------------------------------------------------------------
** Name: PinnedC Type: Symmetry/Axisymmetry/Encastre
*Boundary
Set-10, 1, 1
** Name: Disp Type: Displacement/Rotation
*Boundary
Set-11, 1, 1
**----------------------------------------------------------------
** INTERACTIONS
**----------------------------------------------------------------
** Interaction: Contact
*Contact, op=NEW
*Contact Inclusions, ALL* with self
*Contact Property Assignment,contactproperty
**----------------------------------------------------------------
** STEP: Load
**----------------------------------------------------------------
*Step, name=Load, nlgeom=YES
*Dynamic, Explicit
, 4.2
*Bulk Viscosity
0., 0.
**----------------------------------------------------------------
** LOADS
**----------------------------------------------------------------
** Name: viscous Type: Pressure
*Dsload, ref node=Set-14
Surf-19, VP, 2e-07
```